Modelling and Optimization of a Hydrogen Refuelling Station with CH2P Technology

Delivering decentralized hydrogen and electricity for mobility

Unrestricted
SR.19.001
2019 April

Unrestricted **SR.19.001**

Modelling and Optimization of a Hydrogen Refuelling Station based on CH2P Technology
Delivering decentralized hydrogen and electricity for mobility

by

Daniel Heere

Shell Global Solutions International BV, Amsterdam

Further electronic copies can be obtained from the Global Information Centre.

Abstract

The vehicle industry is increasingly exploring emission-free mobility. Transforming the mobility sector to zero-emission vehicles that consume renewable and low carbon fuels is necessary to reduce the impacts on climate change. Hydrogen powered electric vehicles, or Fuel Cell Electric Vehicles (FCEVs), could make a significant contribution to reduce GHG-emissions and energy use in the transport sector. The current refuelling network for hydrogen vehicles is in its very early stages. The Cogeneration of Hydrogen, Heat and Power project (CH2P) aims to impact the sector with a more efficient solution for the growing hydrogen infrastructure. It does so by offering very efficient decentralized H_2 refuelling stations. The goal of this project is to design a refuelling station that has the ability to refuel hydrogen vehicles and to charge electric vehicles, simultaneously. The on-site CH2P production system is based on SMR and SOFC technology. A thermodynamic model has been designed to size and optimize all the station components. This includes the compression, intercooling, storage, throttling, precooling and dispensing of hydrogen, and the storage and charging of power.

Main messages to take away from this analysis are the following: CH2P as a decentralized production method is profitable. For higher station utilisation the NPV has the potential to increase further by 55 %. Cascade filling of vehicles reduces the total storage demand and is recommended in most scenarios, it greatly reduces the CAPEX and energy consumption of the station. The optimal configuration consisted only of 950 bar High Pressure Storages. By adding a battery to the station, the system can power five fast-chargers to charge BEVs. However, power production by CH2P is more expensive than grid power and the current electric system is not sufficient for coping with sudden power fluctuations.

Table of contents

List of Figures

List of Tables

Nomenclature

Abbreviations

AC	Alternating Current
AFV	Alternative Fuel Vehicle
Al	Aluminium
APPR	Average Pressure Ramp Rate
BEV	Battery Electric Vehicle
CAPEX	Capital Expenditure
CF	Carbon Fibre
CF	Cash Flow
CH2P	Cogeneration of Hydrogen, Heat and Power
COP	Coefficient of Performance
CR	Compression Ratio
CSD	Compression, Storage and Dispensing
CSI	Customer Satisfaction Index
DC	Direct Current
EOS	Equation Of State
EV	Electric Vehicle
FCEV	Fuel Cell Electric Vehicle
FCF	Future Cash Flow
GA	Genetic Algorithm
GHG	Greenhouse gas
H2ME	H_2 Mobility Europe
HPS	High Pressure Storage
HRS	Hydrogen Refuelling Station
HS	Hot Standby
ICE	Internal Combustion Engine
infl	Inflation
IRR	Internal Rate of Return

KPH	Kilometres Per Hour
LHV	Lower Heating Value
LPS	Low Pressure Storage
MPS	Medium Pressure Storage
NIST	National Institue of Standards and Technology
NPV	Net Present Value
NWP	Nominal Working Pressure
ODE	Ordinary Differential Equation
OPEX	Operational Expenditure
PBP	Payback Period
PE	Polyethylene
ppb	Parts per billion
PV	Present Value
PVT	Pressure Volume Temperature
RFB	Redox Flux Battery
SMR	Steam Methane Reforming
SoC	State-of-Charge
SOFC	Solid Oxide Fuel Cell
SS	Stainless Steel
VIR	Value Investment Ratio
WACC	Weighted Average Cost of Capital

Constants

σ	Stefan Boltzmann $[Js^{-1}m^{-2}K^{-4}]$
R	Universal gas constant $[JK^{-1}mol^{-1}]$

Equation Variables

α	Thermal diffusivity $[m^2/s]$
β	Thermal expansion coefficient $[K^{-1}]$
δ_{wall}	Wall thickness $[m]$
$\dot{m}$	Mass flow $[kg/s]$
$\dot{Q}$	Heat $[W]$

$\dot{W}$	Work $[W]$
η_s	Isentropic efficiency [%]
μ_{JT}	Joule-Thomson coefficient $[K/Pa]$
ν	Kinematic viscosity $[m^2/s]$
ρ	Density $[kg/m^3]$
σ_y	Yield stress $[MPa]$
A_s	Area storage $[m^2]$
c	Specific heat capacity $[J/(kg*K)]$
D_h	Hydraulic diameter pipe $[m]$
d_i	Inner diameter pipe $[m]$
D_{int}	Internal diameter $[m]$
g	Gravitational acceleration $[m/s^2]$
h	Convective heat transfer coefficient $[J/(m^2*K)]$
h	Specific enthalpy $[J/kg]$
k	Thermal conductivity $[J/(m*K)]$
L	Length pipe $[m]$
m	Mass $[kg]$
P_d	Discharge pressure $[Pa]$
P_s	Suction pressure $[Pa]$
Q_c	Constant cooling duty $[W]$
Q_v	Variable cooling duty $[W]$
T	Temperature $[K]$
T_{amb}	Ambient temperature $[K]$
T_g	Temperature gas $[K]$
$T_{w,i}$	Temperature wall inside $[K]$
$T_{w,o}$	Temperature wall outside $[K]$
u	Specific internal energy $[J/kg]$
V	Volume flow $[m^3/s]$
v	Flow speed $[m/s]$
V_s	Volume storage $[m^3]$
Z	Compressibility factor [-]

1 Introduction

The vehicle industry is increasingly exploring emission-free mobility. Transforming the mobility sector to zero-emission vehicles that consume renewable and low carbon fuels is necessary to reduce the impacts on climate change. The Energy Agreement from the Social and Economic Council of the Netherlands (SER) contains ambitions to sell only zero-emission new passenger cars from 2035 onwards [1]. On a European scale the objectives in the area of transport and CO_2 include: reducing the greenhouse gas emissions (GHG) by 20 % by 2030 (relative to 2008), the development of sustainable fuels and propulsion systems, phasing out the use of traditional internal combustion engines by 50 % in urban areas in 2030 (and completely by 2050), and achieving CO_2 free logistics in urban areas by 2030.

Hydrogen powered electric vehicles, or Fuel Cell Electric Vehicles (FCEVs), could make a significant contribution to reduce GHG-emissions and energy use in the transport sector. They offer the same mileage as current petrol and diesel fueled vehicles (somewhere between 500-800 km) and the refuelling duration being 3 minutes is similar to conventional vehicles. The main benefit of FCEVs is the use of compressed hydrogen gas that produces electric power via a highly efficient fuel cell, and the only product that comes out of the tail-pipe is water vapour. This would have an enormous positive side-effect on heavy air pollution in urban residential areas [2]. Moreover, hydrogen is one of the most abundant elements on the planet, can be produced from a variety of sources and greatly reduces the amount of carbon emissions when produced from renewables. Besides lower emissions, FCEVs offer quieter (no combustion, less moving parts) and a better responsive driving experience. In order to achieve a similar driving range, the hydrogen density is increased considerably by raising the pressure to 700 bar (i.e. by factor 480).

The current refuelling network for hydrogen vehicles is in its very early stages. To achieve successful market growth globally, vehicle manufacturers, politicians and operators of refuelling infrastructure must make it a top priority to increase the appeal of Fuel Cell Electric Vehicles. The general public demands ease of infrastructure use, simple payment methods and great accessibility. This includes refuelling a hydrogen vehicle tank within an acceptable time period. In Germany, Shell is joining forces with several other industry players, the German government and European Union to lay-out a network of 400 Hydrogen Refuelling Stations by 2023 [3]. Their goal is to deliver early infrastructure deployment. The total hydrogen cost consists of the production, transportation and delivery costs. Almost half of the cost to FCEV owners depends on the station infrastructure [4]. In the early years the station costs will likely remain high as demand needs to increase to become profitable [5].

Currently, the hydrogen is produced on- and off-site, for example, via electrolysis from (renewable) electric power, from natural gas via steam methane reforming (SMR), delivered through pipelines or transported in pressurized tanks on trucks. The majority is produced by fossil fuels such as gas (48%), oil (30%) and coal (18%), and only 4% through electrolysis [6]. Even when FCEVs use hydrogen from natural gas without carbon capture, they emit 20 to 30 percent less CO_2 than vehicles powered by internal combustion engines (ICE) [7].

Shell also participates in the CH2P project, to fully support the transition to a clean transport sector. The Cogeneration of Hydrogen, Heat and Power project (CH2P) aims to impact the sector with a more efficient solution for the growing hydrogen infrastructure. It does so by offering very efficient decentralized H_2 refuelling stations with electric storage services. The CH2P system produces not only hydrogen, but also electric power through its highly efficient Solid Oxide Fuel Cell (SOFC). Early infrastructure deployment is challenging, but the CH2P project tries to ensure that an efficient, safe and affordable Hydrogen Refuelling Station becomes a reality. The main challenges, besides the low number of hydrogen stations, are lowering the capital and operational costs of the station and standardizing the approach.

The goal of this project is to design a refuelling station that has the ability to refuel hydrogen vehicles and to charge electric vehicles, simultaneously. The CH2P unit acts as the on-site producer of hydrogen and electricity and will be seen as the input to this system. The station must facilitate flexible, safe and low cost refuelling and charging of FCEVs and BEVs. Additional electric loads might be present at the station and should be investigated as potential power consumers. In order to bridge the production and demand mismatch, storage facilities will be present at the station. Compressors build the pressure needed, both for effective storage and refuelling, and are supplemented with intercooling stages to prevent the equipment from overheating. Then, before dispensing, the hydrogen is pre-cooled to -40°C. Both cooling procedures are necessary because the tank material induces a temperature limit and the hydrogen temperature increases due to two phenomena. Firstly, during compression the temperature of the gas is increased in the compressor and also in the tank that is being filled. Secondly, opposing to ideal gases, hydrogen heats up during expansion as a result of the Joule-Thomson effect [8]. After successfully modelling the system, the size of the station components will be optimized.

Some studies around entire Hydrogen Refuelling Stations have been conducted, although the list is not extensive. Focus is primarily on thermodynamic models based on on-site electrolysis, tube-trailer delivery or even without production method, looking for energy efficient station configurations. This report is the first to examine the design of a station linked to CH2P technology. Moreover, the focus will be on finding the most economical design and not purely on energy efficiency.

Description of the chapters: Chapter 2 further elaborates on the research questions and corresponding methodology and scope. The following chapter, Chapter 3, conceptually identifies the relevant station components and gives an overview of the system and key design data. Then in Chapter 4 all the models are explained. First, the demand profiles for the vehicles are identified, followed by the working principle of the CH2P system and its modes of operation. Then the hydrogen part and the electric part of the station are explained. The next chapter, Chapter 5, introduces the financial framework used for the optimization of the station components. The results are then discussed in Chapter 6. Finally, the conclusions and recommendations can be found in Chapter 7.

2 Problem statement

Hydrogen refuelling capacity needs to be rolled out on a large scale basis, as a part to ensure consumer willingness to buy fuel cell electric vehicles. A Hydrogen Refuelling Station (HRS) must offer safe, quick, cheap and intuitive ways to deliver hydrogen gas for mobility. Several stations have already been built in the past, dispensing hydrogen gas obtained via various production routes and methods (e.g. electrolysis, pipelines, trucks etc.) However, the system proposed under the CH2P project locally co-generates hydrogen, heat and power from natural gas using steam methane reforming and Solid Oxide Fuel Cell technology. This combines the ability to deliver both hydrogen to Fuel Cell Electric Vehicles (FCEVs) and electric power to Battery Electric Vehicles (BEVs). As the station will be capable of producing different products, a strategy for sizing and operating the pathways needs to be found. It is critical to understand how the system functions dynamically and what strategy should be followed to effectively supply future hydrogen and electric demand profiles, while bringing down the cost. This resulted in the following research question.

2.1 Research questions

2.1.1 Main question

The aim of this research is to answer the following main question:

- *What is the optimal design for a Hydrogen Refuelling Station delivering hydrogen and power produced by a CH2P unit to Fuel Cell and Battery Electric Vehicles?*

2.1.2 Sub-questions

Supporting sub-questions are:

- *What are the projected refuelling and charging demand scenarios for the mobility sector of tomorrow?*
- *What are the station's system components, process conditions and operating strategy?*
- *What is the optimal station configuration and corresponding size?*

2.2 Methodology

After identifying the research question, literature and other (internal) sources of information will be explored to get acquainted with the overall research topic. At first, future market demand profiles for hydrogen and electric vehicles need to be classified in different scenarios. The demand is important for sizing the overall system. Next, the process requirements, process block schemes, process flow schemes, mass and heat balances will be determined. The following stages include further mathematical modelling of all system parts, sizing the equipment and defining the operating modes for the system. Focus remains on using realistic system components, ideally gathered from industry players.

It must be ensured that the requirements of standards and protocols, such as the SAE J2601 fuelling protocol, are met at all times. The thermodynamic model incorporates the mass, temperature, pressure, and power evolution over time at the station from source to vehicle (the latter not included). Emphasis is put in gathering precise economic factors as they greatly impact the nature of the design. Programming and simulation will be done in Matrix Laboratory (MatLab) software. An optimization layer will run on top of the simulation model to optimize the system components. The optimization method uses MatLab's Genetic Algorithm to test different scenarios. During the optimization a penalty function based on the number of satisfied customers pushes the optimizer towards the desired outcome.

2.3 Scope

The scope of the project includes finding the hydrogen and electric power demand profiles for vehicles and the station. It further covers the thermodynamical modelling of the system except for the CH2P system and the vehicle tank. The system contains hydrogen and electric storage facilities, mechanical hydrogen compressors, heat-exchangers for gas intercooling and pre-cooling, dispensing and charging procedures. The CH2P production method is already designed and is not part of this research. The CH2P unit will act as a blackbox, only the operating modes and in-and output behavior is used. Also excluded from this analysis are pipes/valves, other forms of compression and all electrical components except for the battery and fast-charger. The effects of grid balancing services are not considered as they depend on local incentives.

3 Concept design

Distributed production by the CH2P system could be an effective way to introduce hydrogen in the nearby future for low demand markets. The use cases under consideration as stated by the consortium are as follows:

- Hydrogen production for the station plus power production to run the CH2P system itself
- Hydrogen production for the station plus power to cover on-site electricity consumption like the CH2P system, the hydrogen station and the conventional refuelling station (including lighting, car wash and shop)
- Hydrogen production for the station plus power production for charging battery electric vehicles
- Hydrogen production for the station plus power production for export (to the grid, including for power balancing, or to neighbouring electricity consumers)

3.1 System Overview

Main tasks of the station are to produce hydrogen and power, provide storage to meet the production and demand mismatch, and provide refuelling and charging possibilities to vehicles. Figure 3.1 shows a specific hydrogen configuration with Low Pressure and High Pressure storage as an option.

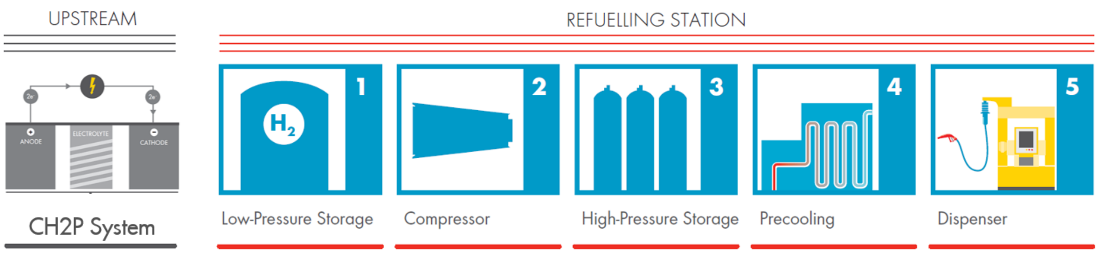

Figure 3.1: Station components hydrogen

Table 3.1: Key design data and assumptions

Item	Value
Simulation period	24h
CH2P capacity	400 kg/day
CH2P H_2	7 bar
High Pressure Storage	950 bar
FCEV pressure	700 bar
FCEV vessel	7 kg
Refrigeration	-40°C
BEV charger	150 kW

Table 3.2: Station tasks and possible equipment

Task	Description	Equipment
Hydrogen production	Production of hydrogen from natural gas	CH2P (SMR & FC)
Power production	Produce electricity from hydrogen	CH2P (FC)
Hydrogen storage	Cover production and demand mismatch	Pressurized/ cryogenic
Electricity storage	Cover production and demand mismatch	Electrochemical, battolyser
Hydrogen compression	Bring to storage or vehicle pressure	Mechanical, electrochemical
Hydrogen intercooling	Lower temperature between compression stages	Heat exchanger
Hydrogen precooling	Precool -40 °C before dispensing (SAE J2601)	Heat exchanger
Hydrogen dispensing	Connection station and vehicle	Dispenser
Electric charging	Charge Battery Electric Vehicles	Electric charger
Sell/buy electricity	Import/export electric energy	Grid connection

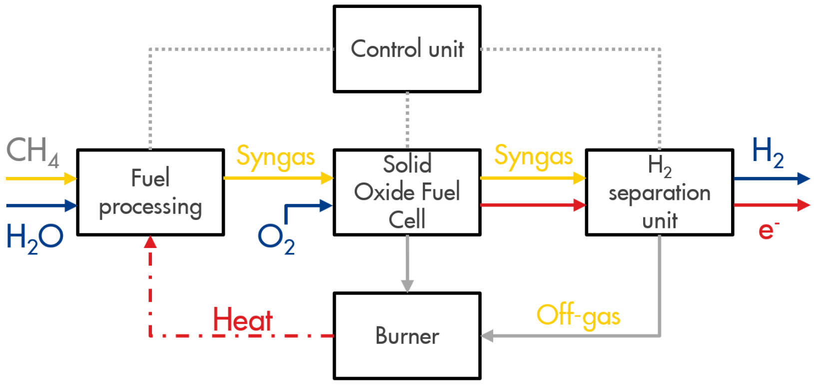

Figure 3.2: Blockdiagram CH2P unit

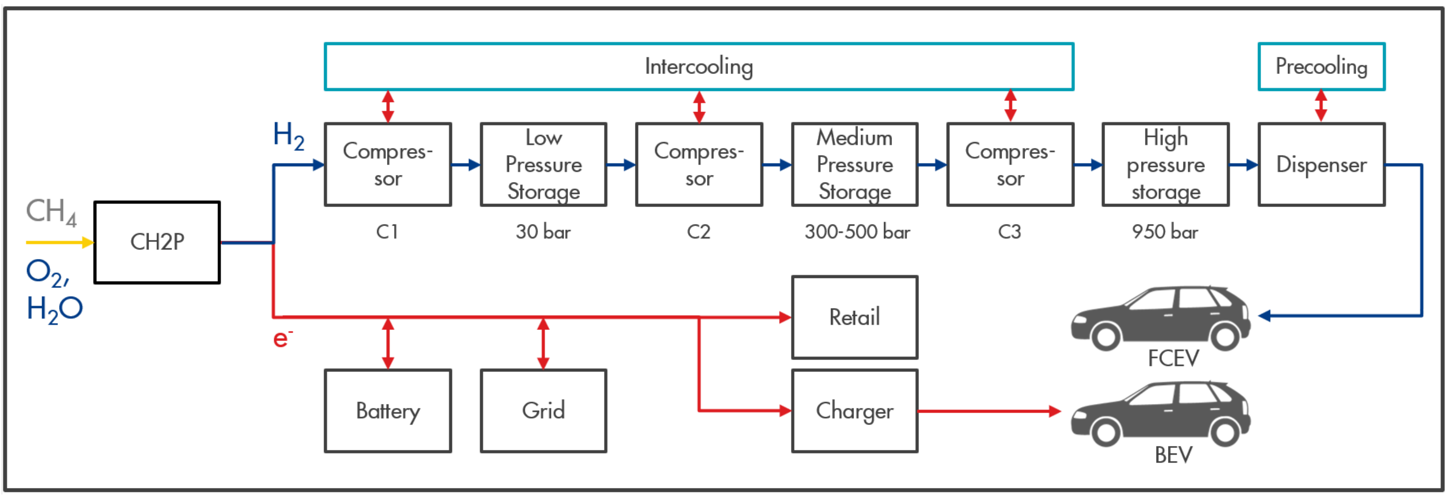

Figure 3.3: HRS blockdiagram

4 Models

In this chapter first the hydrogen and electric demand are discussed in Section 4.1. The electric demand not only includes power for BEVs, but also for the retail station and the CH2P system itself. In Section 4.2 the working principle of the CH2P unit is explained and the modes it operates in. Then all the hydrogen system components are explained in Section 4.3, followed by the electrical system in Section 4.4.

4.1 Demand

Transportation creates almost 25% of Europe's greenhouse gas emissions and is the main cause of air pollution in cities [9]. It is a top-priority to increase the efficiency in the transport sector, and to make sure clean alternatives for fossil fuels are widely available and also to encourage further transition to low emission vehicles. More value will be added in alternative powertrain technologies encouraged by stricter emission regulations. Large scale adoption of alternatives, such as electrification, becomes more likely to meet CO_2 targets. Decarbonization can be helped by hydrogen-powered vehicles complementing battery electric vehicles, whereas BEVs offer high fuel efficiency for light-weighted vehicles ideally for short range and hydrogen vehicles with higher energy densities are suitable for heavy transport or larger distances.The transition will further include growth of carsharing, connected and autonomous vehicles.

Current developments of Hydrogen Refuelling Stations and FCEVs are in the early stages of market introduction. Early market challenges exist as the car manufacturers are reluctant to build new vehicle types without the supporting infrastructure existing. However, investments in infrastructure by the station holders is likewise lingering [10]. Luckily the H_2 Mobility Europe (H2ME) project gives FCEV drivers access to a network of Hydrogen Refuelling Stations. In particular, H2 Germany plans to have built 100 stations by the end of 2019 [5]. In California (U.S), the government supports the market to reach 1000 hydrogen stations and 1.000.000 fuel cell vehicles in 2030 [11].

Consumers are looking for high availability refuelling stations with quick and convenient charging or refuelling for low prices. BEVs require longer charging times than FCEVs, but high power chargers up to 150 kW could greatly reduce waiting times in the future.

Demand projections for hydrogen and electricity shape the dimension of a HRS. Refuelling station demand variates on different time scales, where storage helps against the production and demand mismatch. The first level is the short term capacity needed for hourly variations and the second one accommodates for long term or seasonal variations. Figure 4.2 shows representative short term variations in demand. Long term profiles arise from higher driven distances in summer versus winter periods [12]. In this report only the short term mismatch during the day is considered.

4.1.1 Hydrogen demand

The size of the station depends greatly on the number of arriving vehicles. Moreover, it is important to understand when these vehicles typically refuel and what demand per customer generally exists. An indication is made by randomly generating car arrivals that

Figure 4.1: Hourly gasoline demand [12]

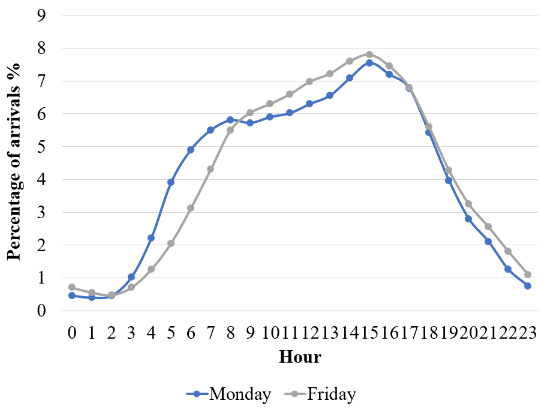

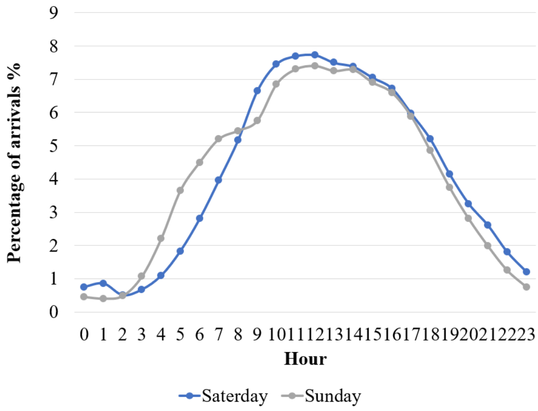

fit the probability curve of gasoline cars and assuming a certain hydrogen demand per fill. Then the effect of adding more dispensers to the station is explored and the results are compared based on waiting time, customer satisfaction and dispenser availability.

In the beginning of 2018 there were 8.4 million cars in the Netherlands, and nearly 400 thousand new cars entered the market [13]. The Hydrogen Council envisions 3.0% of new vehicles sold globally in 2030 to be hydrogen-powered. In leading areas, California, Germany, Japan, and South Korea, 1 in 12 cars sold in 2030 could be hydrogen driven [14]. From the average mileage driven by passenger cars we can calculate the hydrogen usage (kg/day) to give an idea about the required number of refuelling stations and effective station utilization. Station size and utilization rates are expected to grow throughout the coming years. The model focuses on one 400 kg/day system with utilization rates ranging from 30% to 100%, as the system is modular expandable.

Table 4.1: Demand scenarios single 400 kg/day CH2P system

Utilization	30%	40%	50%	60%	70%	80%	90%	100%
H_2 sold (kg/d)	120	160	200	240	280	320	360	400
Cars/day	24	32	40	48	56	64	72	80

Commuter patterns influence hourly distribution of refuelling events, mainly work related travel. U.S. data of refuelling station demand, based on over 400 gasoline stations, shows different weekly profiles and normally distributed peaks during morning and afternoon rush hour [12]. Peak refuelling takes place on Friday evening, when consumers most likely try to be ready for the weekend, and on Sunday afternoons to prepare for work, reducing demand on Mondays and Tuesdays. Weekend days show considerable different profiles, picking up later in the morning. Daily profiles start growing around 5 a.m. with a maximum around 5 p.m.. This is shown by Figures 4.1, 4.2. Additional assumptions are made to further simplify the situation. Differences between summer and winter periods are leveled out, as is done with weekly variations. Furthermore, each car arrival shows the same fuelling behavior.

In the US an average fill is 70 % of the tank volume, so a typical fill for a 7 kg, 174-L, type IV hydrogen tank is around 5 kg. Vehicles are assumed to begin filling with pressure 15 MPa at 298 K, reflecting an initial state of charge of 2.0 kg. As a rule of

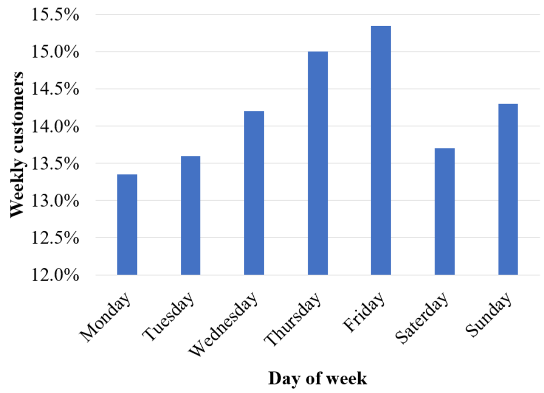

Figure 4.2: The weekly gasoline demand [12]

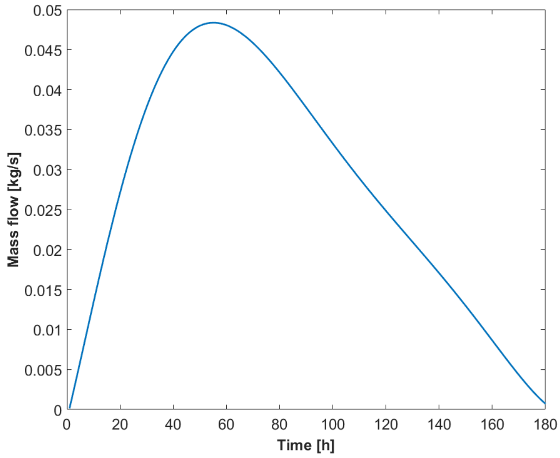

Figure 4.3: Mass flow profile for hydrogen dispensing

thumb the distance traveled per kg hydrogen is roughly 100 km [12]. Fuelling protocols for light duty and medium duty gaseous hydrogen surface vehicles are listed in the SAE J2601 standard [15]. The maximum dispensing rate of hydrogen is 60 g/s. Refuelling takes about 3 minutes for a maximum maximum working pressure of 87.5 MPa at 358 K or 70 MPa at 298 K. Figure 4.3 shows the ideal mass flow for a refuelling activity, fitted to the SAE J2601 refuelling curve. More on the refuelling procedure in Section 4.3.4.

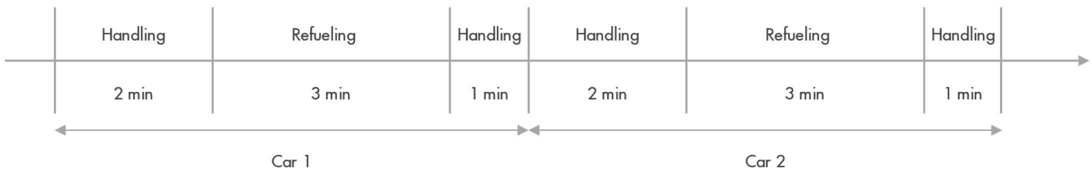

Figure 4.4: Refuelling procedure back-to-back fill hydrogen car

Based on the foregoing data a specific day is selected acting as a basis on which the station equipment is optimized. From 365 randomly generated arrival profiles we must pick a day that has more back-to-back fillings (i.e. higher load), but does not over-dimensionalize the station for too extreme values. All generated days are evaluated by a moving sum of the number of arrivals in a 'moving' time window of a certain width (in this case 1, 3 and 5 hours). A normal distribution is fitted to the maximum moving sum per generated day. At $\mu + 1.5\sigma$ the station is expected to be successful in 93.3 % of randomly selected days. For days with the same maximum the one with the highest moving sum with 3 hour width is picked (see Figure 4.5). Figure 4.6 shows the selected profile and number of arrivals per hour, whereas Figure 4.7 shows it on a minute basis with corresponding moving sum at the bottom.

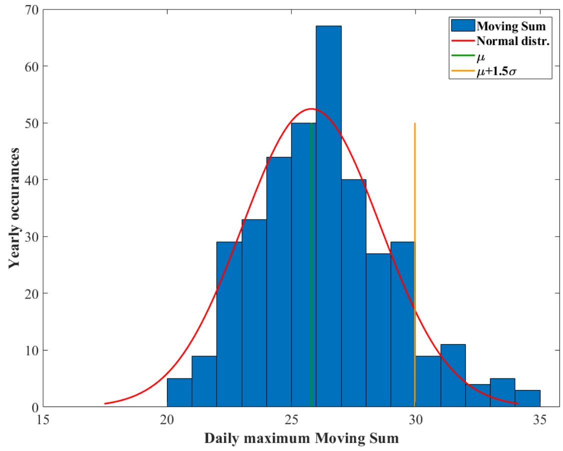

Figure 4.5: Selection of FCEV profile - Moving Sum 5h

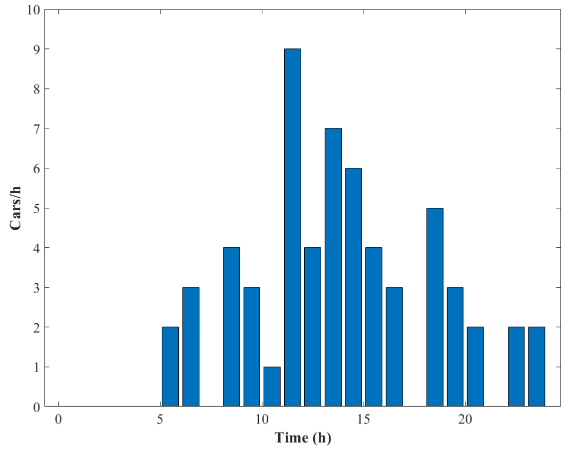

Figure 4.6: Hourly FCEV arrivals for selected day

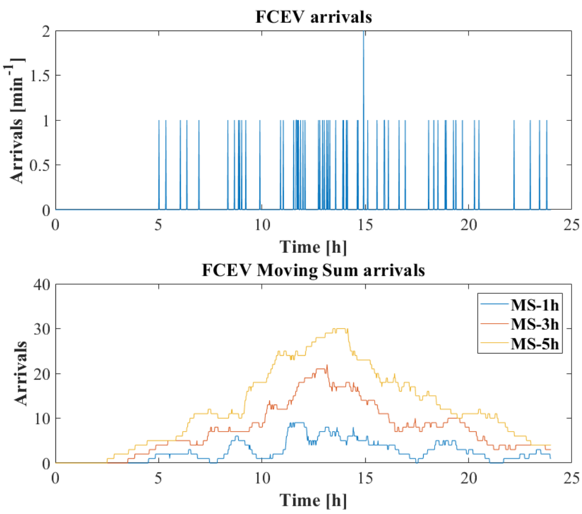

Figure 4.7: Generated arrival times for FCEVs on specific day and moving sum with different time windows

Then the ideal number of dispensers must be determined and its effect on the Customer Satisfaction Index (CSI). It can be seen in Figure 4.8 that for increasing station utilization more dispensers are needed to reach a high CSI. Two dispensers is ideal for this profile, the occupation rate per dispenser is shown in Figure 4.9.

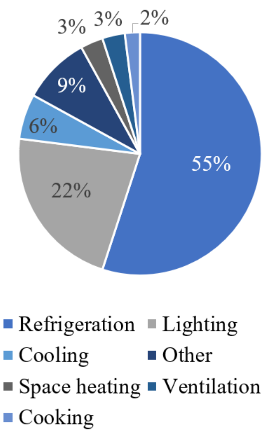

Figure 4.10: Electricity consumption convenience stores [16]

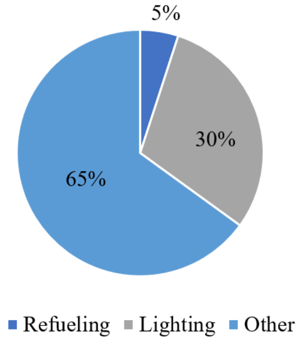

Figure 4.11: Typical power consumption conventional retail station

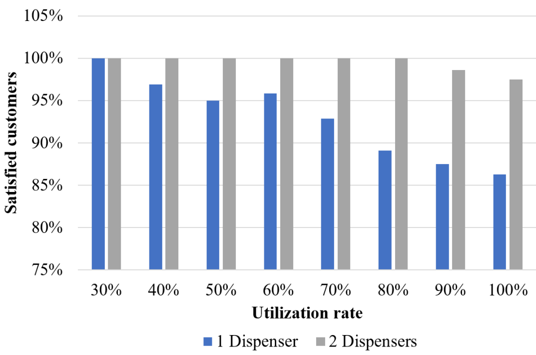

Figure 4.8: CSI at different utilization rates and dispenser numbers

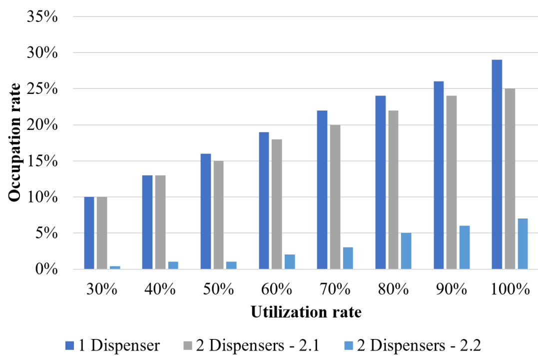

Figure 4.9: Average occupation rate of dispensers

4.1.2 Electric demand

In this section the overall electric demand for the station is identified. The CH2P system not only acts as a provider of hydrogen, but simultaneously has the ability to deliver 500 kW of gross power. Therefore, the electric demand from different loads needs to be scrutinized. Apart from the vehicles the retail station demands power as well. The implications of adding a battery to the system or the effect of the grid connection capacity is discussed in Section 4.4.

At conventional retail stations in Europe the power consumption lays between 250 to 1500 kWh per day (FICTIVE). Measurements at a small station show 15 kW average power levels throughout the day, where larger stations consume on average 30 kW. During night hours (22:00 - 05:30h) the power consumption is roughly half of normal levels, although considerable amount is used for lighting ($\approx$ 30%). At a conventional station only 10 % (FICTIVE) of the power consumption is used for the fuelling process. Other loads involved are refrigeration, heating (electrical in UK/NL markets) and cooling and gas pumps.

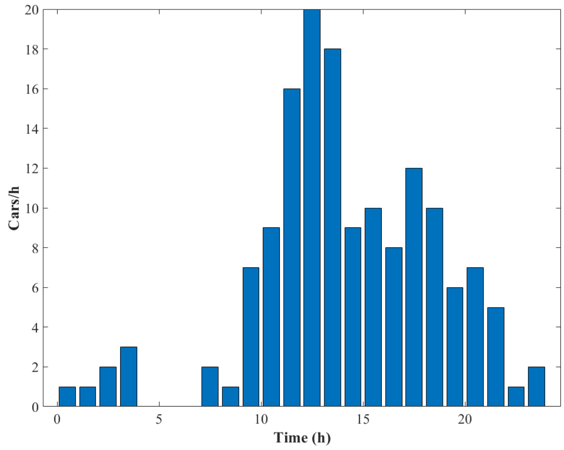

Figure 4.12: Hourly BEV arrivals for selected day

The CH2P system is capable of producing 500 kW gross power (depending on the operating mode of the system), of which a certain part is available for charging vehicles. After deducting power consumption for the retail station, the compression and cooling of the hydrogen, 50 % is estimated to be available for charging. In Section 4.2 the different operating modes are listed and their corresponding power output levels. Due to these high power capabilities a wide range of utilization rates will be examined, see Table 4.2, as in the starting phase utilization rates are expected to be low.

Most early BEV owners charge their vehicles at home, but there is still a high demand for public charging infrastructure. BEVs should be equally attractive for people traveling longer distances or without having their own garage. Energy consumption for a vehicle is 18 kWh/100 km [17]. BEV charging takes considerably longer than refuelling with gasoline or hydrogen. In the coming years chargers are expected to grow in power capacity to ensure faster charging. The station can provide electricity to a large number of vehicles. The average charging duration per vehicle is 15 minutes. The average charging power is 50 % of the maximum power capacity of 150 kW for a fast charger. Fast charging is possible up to SoCs of 70-80 %. To avoid battery degradation effects the battery is charged while slowly reducing the charging voltage upon reaching high SoCs. In the model the power drawn by the cars is taken constant.

Table 4.2: Demand scenarios battery electric vehicles at 50% power availability for charging (i.e. 5 MWh)

Utilization	10%	20%	30%	40%	50%	60%	70%	80%	90%	100%
Power (MWh/d)	0.5	1.0	1.5	2.0	2.5	3.0	3.5	4.0	4.5	5.0
Cars/day	27	53	80	107	134	160	187	213	240	267

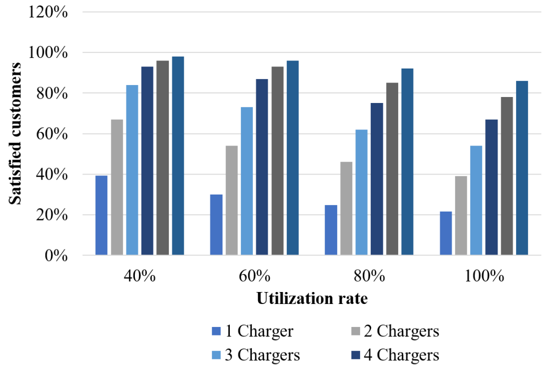

Figure 4.13: CSI at different utilization rates and dispenser numbers

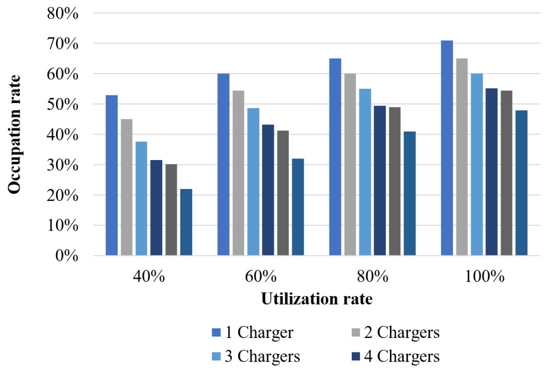

Figure 4.14: Average occupation rate of chargers

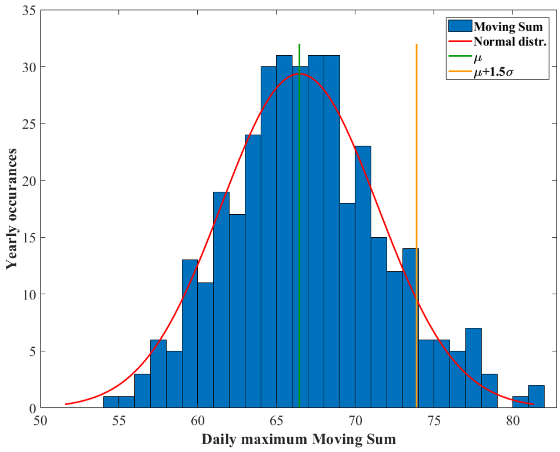

Figure 4.15: Selection of BEV profile - Moving Sum 5h

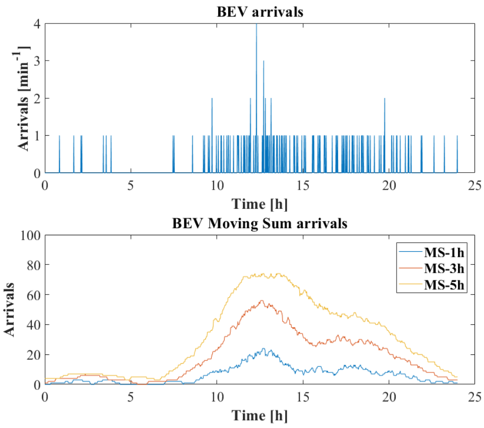

Figure 4.16: BEV arrival times and MS different time windows

4.1.3 Queuing model

In order to run realistic scenarios for the station model, where numbers of arrivals are expected to grow with increasing EV penetration, the station queuing is modeled. Economic operation of the HRS aims at high occupancy rates at both chargers and dispensers, however there is a trade-off with customer waiting times. Based on the earlier defined daily number of FCEVs and BEVs, the arrival times in minutes are randomly generated and weighted by the corresponding probability density function as discussed in the previous sections. Outcomes of interest are the length of the queuing line, what the average waiting time is per vehicle and how many satisfied customers related to a predefined level leave the station accordingly. Every individual refuelling moment is assumed to follow the same protocol and shows identical customer behavior, the same applies to charging.

The maximum acceptable time customers want to wait in line is set at five minutes, as longer waiting times result in unhappy customers. The size of the waiting room is unlimited however. The Customer Satisfaction Index can be increased by adding more dispensers or chargers. The queuing can only be simulated with one type of dispenser or charger at a time. In other words, it is, for example, not possible to simulate the station queuing by using a 50 kW and 150 kW charger simultaneously. The cueing procedure is shown in Figure C.3.

Figure 4.17 shows when hydrogen cars have to wait and for how long. The upper plot gives the corresponding car number and red lines indicate unsatisfied customers that drive away due to long waiting times. For 60 FCEVs the average waiting time is 0.2 min and 98.3 % of customers are satisfied for two dispensers in place. The waiting time for electric cars is longer despite the larger number of chargers, this due to longer handling times per vehicle and higher vehicle numbers. The average waiting time per vehicle is 0.5 minutes and the percentage of satisfied customers is 96 % for six fast-chargers and 150 BEVs. It can be noticed that most of the waiting is concentrated around mid-day.

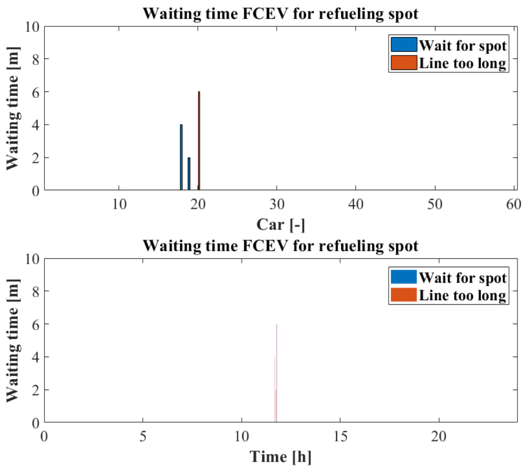

Figure 4.17: Waiting time per FCEV

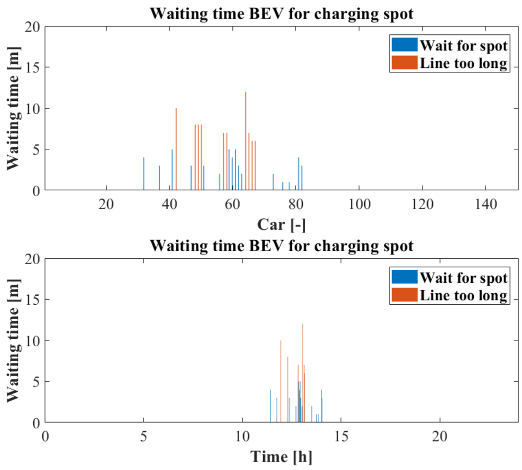

Figure 4.18: Waiting time per BEV

4.2 CH2P

This section gives more background on the working principles of the underlying CH2P unit. The cogeneration of hydrogen, heat and power is based on steam methane reforming and fuel cell technology. Production of hydrogen and electricity by the CH2P unit is more efficiently than standard SMR or standard power generation, and reduces CO_2 emissions. The system is able to operate in six different modes, including Hot Standby (HS) in which no production occurs.

4.2.1 SMR and SOFC

Natural gas is partially reformed with steam at high temperature, the resulting syngas (CH_4, CO, H_2, H_2O) is fed to the fuel cell, then fully reformed to hydrogen and partially converted to power, CO_2 and steam. The hydrogen is purified to a level of 99.999% with less than 200 ppb CO particles. Temperature of the exhaust gas is around 800 °C, then cooled down for further purification in a Pressure-Swing Absorption unit (PSA). The off-gas is fed to a burner to provide heat for the SMR. The CH2P unit is far more efficient and less emissive than traditional SMR by utilizing the high temperature of the fuel cell for the reforming process and integrating the heat loss of the system. The second advantage is the flexibility of changing the production ratio of hydrogen and power depending on the demand. Finally, water is recycled, which greatly reduces the overall water demand.

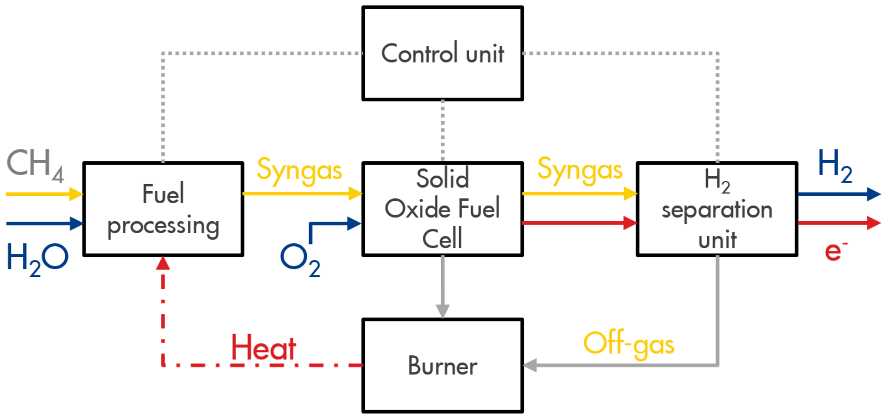

Figure 4.19: Block diagram CH2P unit

Steam methane reforming is based on gas (e.g. biogas, natural gas) as a feed-stock. In a reformer hydrogen (H_2) and carbon monoxide (CO) are produced when methane (CH_4) reacts with steam in a highly endothermic process (Equation 4.1). The reactions takes place at very high temperatures (700-1000 °C) nearby a metal catalyst. The hydrogen production is enhanced via the water-gas shift reaction, where carbon monoxide reacts with water to form carbon dioxide and hydrogen (Equation 4.2). The equilibrium of the latter reaction shifts to the right with lower temperatures. There are few articles around SMR for on-site hydrogen production, Yang et al. [18] shows good conversion at rather low productions rates.

$$CH_4 + H_2O \iff CO + 3H_2 \tag{4.1}$$

$$CO + H_2O \iff CO_2 + H_2 \tag{4.2}$$

A Solid Oxide Fuel Cell is an electrochemical device that converts chemical energy to electrical energy at high temperature. The cells exist in different designs, for example stacked in tubes or layers. The operating temperature of the cell ranges from 600 - 1000 °C. Most cells use hydrogen as fuel, which in this system is produced from natural gas by steam methane reforming. When the SOFC is supplied directly with CH_4, it internally reforms the gas and produces hydrogen and electricity [19]. The reactions are again the reforming and water-gas shift Equations 4.1 and 4.2. The electrolyte is made from a ceramic solid oxide that conducts the oxygen ions. The high temperature increases the conductivity of these ions. Much research is focused on finding materials that have higher conductivities at lower temperatures. An advantage for these type of cells is that for a solid electrolyte the lifetime is much longer than for others [20]. The basic reactions in the cell are given in Equations 4.3, 4.4, 4.5. Additional reforming takes place when methane reacts with water at the anode and produces more hydrogen. The resulting carbon monoxide can then form carbon dioxide with oxygen ions or react with water to create more hydrogen. Figure 4.20 explains how the basic fuel cell reactions without reforming occur.

$$Total : 2H_2 + 2O_2 = 2H_2O \tag{4.3}$$

$$Cathode : O_2 + 4e^- = 2O^{2-} \tag{4.4}$$

$$Anode : 2H_2 = 4H^+ 4e^- \tag{4.5}$$

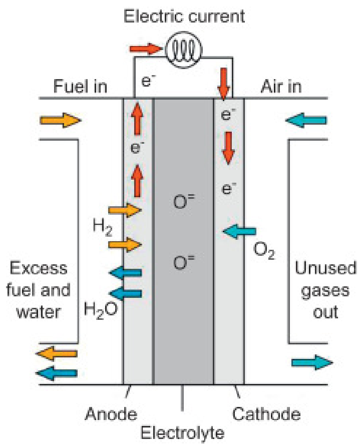

Figure 4.20: Solid Oxide Fuel Cell [21]

Raw Mode	Input NG kg/h	O$_2$ kg/h	Pwr kW	Output H$_2$ kg/h	CO$_2$ kg/h	Pwr kW
1	-	2016	19	2.5	-	148
2	-	3536	94	17.5	-	142
3	-	4824	83	17.2	-	415
4	-	2380	52	8.1	-	209
5	-	3600	36	2.4	-	270
HS	0	0	0	0	0	0

Table 4.3: Input-output values CH2P system

4.2.2 Operating modes

The CH2P system has the ability to operate in various modes. Table 4.4 shows the corresponding in- and output. In Figure 4.21 the modes are displayed with gross power production on the y-axis and hydrogen production per day on the x-axis. It is assumed that in Hot Standby mode the production is zero. The transient for the system to switch between different modes is 40 minutes (FICTIVE). The mode of operation is determined by the state-of-charge of the storages that are connected to the CH2P unit directly (see Figure 4.22). For example, if the first hydrogen storage is a Low Pressure Storage (LPS) and its state-of-charge is 25 % and the battery is 75 % full, then mode 2 is selected. Above 90 % it turns to Hot Standby. The goal is to keep the station ready and storages full, therefore mode 3 has a larger operating area. For longer transient times, the thresholds at which modes switch must be redefined (Figure 4.22). During a 60 minute transient the storage will be filled for a longer time and therefore the mode must be changed earlier.

Table 4.4: Operating modes CH2P

Mode	CH$_4$ [kg/d]	Power gross [kW]	Power CH2P [kW]	Power net [kW]	Hydrogen [kg/d]
1	-	167	19	148	61
2	-	236	94	142	420
3	-	498	83	415	412
4	-	261	52	209	195
5	-	307	36	271	58
HS	0	0	0	0	0

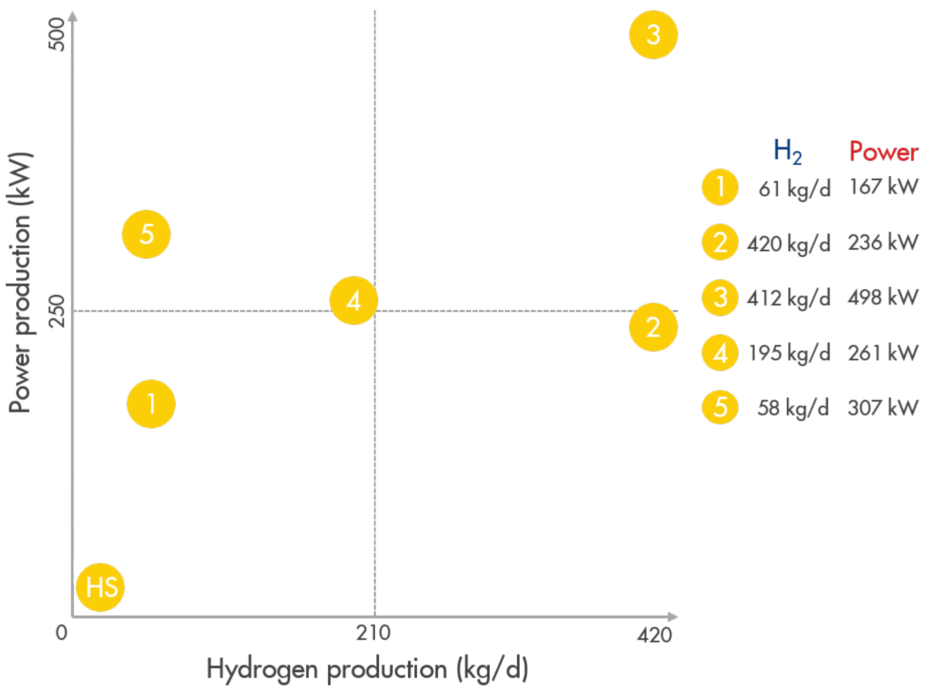

Figure 4.21: Operation modes in main state, system produces electricity and hydrogen with fixed power request and H2 production

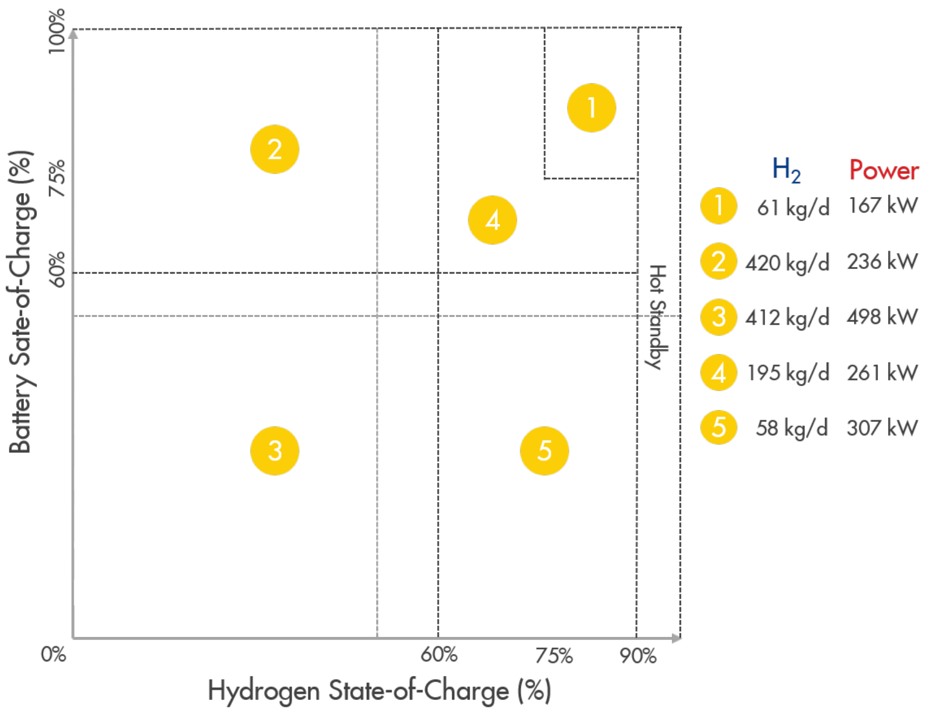

Figure 4.22: Operation modes selection based on the battery and storage State-of-Charge

4.3 Hydrogen line

In this section all the components regarding the hydrogen compression, storage, throttling, cooling and dispensing are discussed in more detail. The design is heavily influenced by the SAE J2601 protocol developed by the Society of Automotive Engineers (Appendix B). This standard provides technical information and look-up tables that give, for example, the final pressure of the vehicle tank after refuelling for vessel types. The Average Pressure Ramp Rate (APRR) is given for different station parameters to make sure that the temperature limit in the tank is not exceeded during filling.

The number of studies that have developed models describing the entire Hydrogen Refuelling Stations is not extensive. Most studies focus on the filling of vehicle vessels and to a lesser extent on the optimization of the station's components. However, Rothuizen et al. [22] developed a thermodynamic model to optimize the full station design. Multiple pressure banks were tested showing that the total energy demand can be reduced by adding more storages to the station. The reduction in compression energy was found to be 17 % and 12 % in cooling demand. The second study conducted by Rothuizen and Rokni [23] found that the most energy efficient configuration for the hydrogen cascade system would consist of three storages. Another study developed the same type of model, but focused also on the station's heat integration by re-using waste heat collected in an ammonia absorption refrigeration unit [24]. The proposed station included an on-site electrolyser for hydrogen production from water and power. Four cases for making an absorption refrigeration process were investigated, concluding that such a system is not achievable at the conditions tested (only effective for low ambient temperatures). The model did not consider heat transfer in the storages, which are included in this report.

The model's complexity is simplified by several assumptions:

- Hydrogen flows adiabatically through the pipes between all the system components
- Ideal mixing occurs when the storages are filled and gas properties are homogeneous
- All storage tanks below 300 bar are tank type I, above 300 bar are tank type IV
- A storage vessel can either be filled or emptied at the same time (not both simultaneously) [25]
- The compressor has a constant mass flow. For the cascade setup, it first refills the smallest storage to keep it ready at high pressure for any refuellings.
- Both intercooler and precooling systems are assumed to be present and capable of providing the necessary cooling. Furthermore, the precooler is assumed to be at -40°C constantly and is capable of cooling the hydrogen within a few seconds.
- The vehicle tank is only filled from the storages and not directly by a compressor.

Before zooming into the hydrogen components the non-ideal gas property is shown (Figure 4.23).

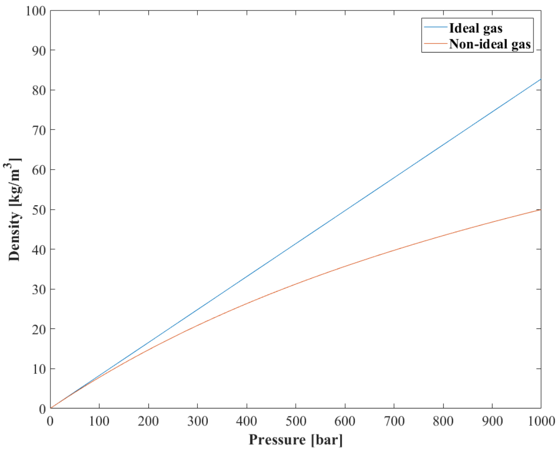

Figure 4.23: Hydrogen density for (non-)ideal gas

4.3.1 Compressor

The compressor raises the hydrogen pressure to the desired storage pressure level. As can be seen in Figure 3.3, the maximum number of (multi-stage) compressors is three, when all storage levels are used. More stages enables the possibility of interstage cooling, which is needed to limit the discharge temperature from the compressor. The compressor only refills the stationary storage tanks at the station and is not used for direct filling of the vehicle tank. This method increases the amount of compression work, as part of the delivered work is lost again when the gas is throttled from stationary to vehicle storage pressure. However, stationary storages are always included in the design to make sure relevant mass flows are reached without the need for over-sized compressors.

Reciprocating compressors are widely used today (e.g. in refineries) to compress hydrogen by moving pistons that reduce the volume of the hydrogen. Besides mechanical devices for hydrogen compression, electrochemical options may soon be feasible that offer higher efficiencies, less maintenance and silent operation [6; 26]. In this report only the first type is considered as they are used most commonly. For high pressure compression they are non-lubricated to assure that the hydrogen gets not impurified by any evaporating lubricant-oil. Another new type of compressor uses an ionic liquid instead of a metal piston. This liquid is nearly incompressible and does not evaporate. Compressors can now use nearly all the dead volume that was previous left in the cylinder to further increase efficiency and greatly decrease the number of moving parts to reduce down-time.

Parks et al. [27] and compressor manufacturers recommend to break the compression section into two parts for several reasons. Firstly, due to the unavailability of a compressor pressurizing hydrogen from 7 to 950 bar, and secondly, because the total energy consumption upon refuelling can be reduced by using storages of intermediate pressure. Even though the CH2P unit is comfortable running in various modes, the low-pressure compression of hydrogen leaving the unit is rather continuous, whereas the compression towards the much higher pressure storages runs in separated duties to bring the vessels back to required dispensing levels. Nowadays larger compressors exist however, and the optimum configuration of storages and compressors will follow from the optimization.

More about the storage configurations in Section 4.3.2.

Reversible isothermal compression assumes that the gas holds a constant temperature upon compression. Heat produced by compression is removed at the same rate.

$$\dot{W}_{isothermal} = RTln(P_s/P_d) \tag{4.6}$$

In an isentropic idealization the cycle is considered internally reversible and adiabatic, meaning there is no entropy generation ($\Delta s = 0$) within the system and there is no heat transfer ($\dot{Q} = 0$) from the gas during compression. All the work adds to the internal energy so that both the temperature and pressure increase. The isentropic efficiency compares actual performance to performance under idealized circumstances. Ignoring heat transfer with its surroundings and negligible kinetic and potential energy contributions, the required shaft work by the compressor is:

$$-\dot{W} = \dot{m}(h_1 - h_2) \tag{4.7}$$

where $\dot{m}$ is the mass flow and h_1 and h_2 are the in- and outflow enthalpy. The isentropic compressor efficiency, typically between 75% and 85% is the ratio of isentropic and real performed work:

$$\eta_s = \frac{(-\dot{W}/\dot{m})_s}{(-\dot{W}/\dot{m})} \tag{4.8}$$

Since the desired outlet pressure is given and the entropy stays constant ($s_2 = s_1$), these two state variables give the ideal enthalpy of the outgoing compressor flow. Then, the real outlet enthalpy flow (h_2) is calculated from:

$$h_2 - h_1 = \frac{h_{2s} - h_1}{\eta_s} \tag{4.9}$$

In which the isentropic efficiency is found from the following equation that is valid between pressure ratio 1.1 and 5 [23]:

$$\eta_s = 0.1091(\ln\frac{P_d}{P_s})^3 - 0.5247(\ln\frac{P_d}{P_s})^2 + 0.8577\ln\frac{P_d}{P_s} + 0.3727 \tag{4.10}$$

Figure 4.24 visualizes the isentropic efficiency for a wide range of pressure ratios and shows that based on the compression ratio (CR) we would prefer a high compression ratio. Relevant compressor parameters are given in Table 4.5.

Quantity	Value	Unit
$P_{suction}$	7	bar
$P_{discharge}$	950	bar
T_{in}	20	°C
T_{lim}	220	°C
$T_{intercooling}$	45	°C
CR_{max}	3.5	-

Table 4.5: Compression parameters

The amount of work increases for higher suction pressure (when compression ratio is kept constant, see Figure 4.25a). Figure 4.25b shows the compression work needed

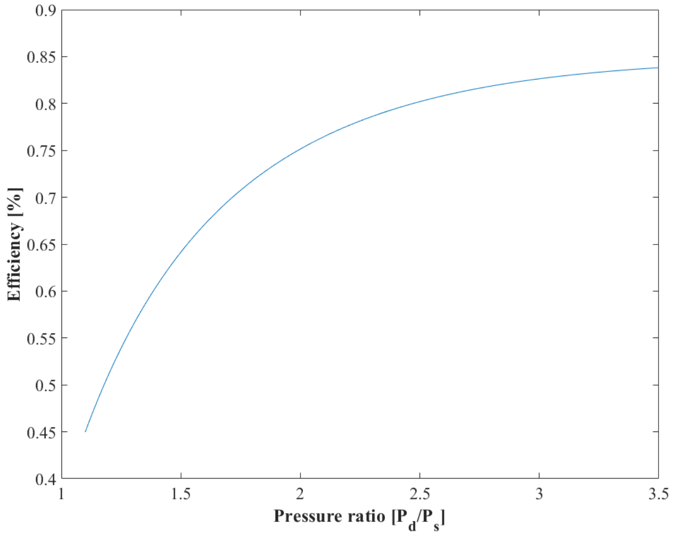

Figure 4.24: Isentropic compressor efficiency as function of compression ratio

for increasing the number of stages for a compression factor of 3.5. The result feels counterintuitive because with more stages and intercooling the compression should become more ideal towards the isothermal situation. In this case, however, the efficiency for lower pressure ratios is more influential. For compression to a High Pressure Storage (HPS, 950 bar) another interesting point arises. For low suction pressures more stages are required to reduce the amount of work per unit mass of hydrogen and to keep the discharge temperature within limits (Figure 4.27), but for higher values the number of stages must be reduced both from an energy and capital cost perspective (for $\eta_{is} = f(CR)$). See Figures 4.26a, 4.26b for the difference between fixed and variable isentropic efficiencies.

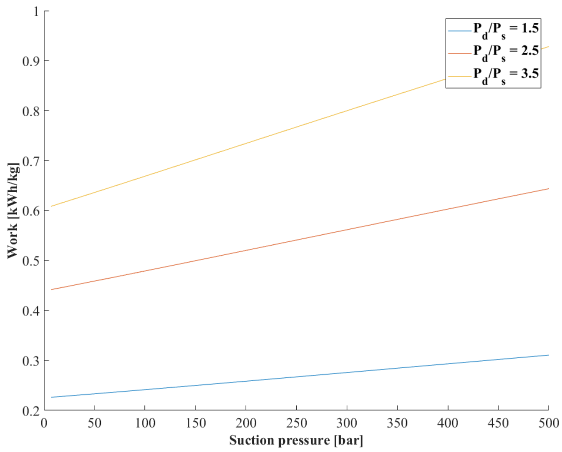

(a) Work for several compression ratios

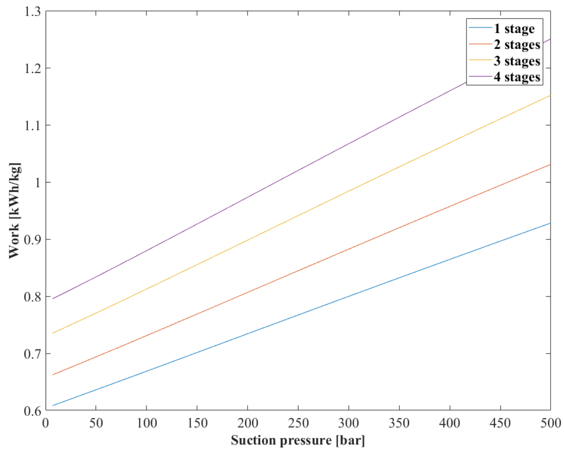

(b) Multistage compression work at fixed pressure ratio

Figure 4.25: (Multi-) stage compression work as function of different suction pressures for varying pressure ratios and compressor stages

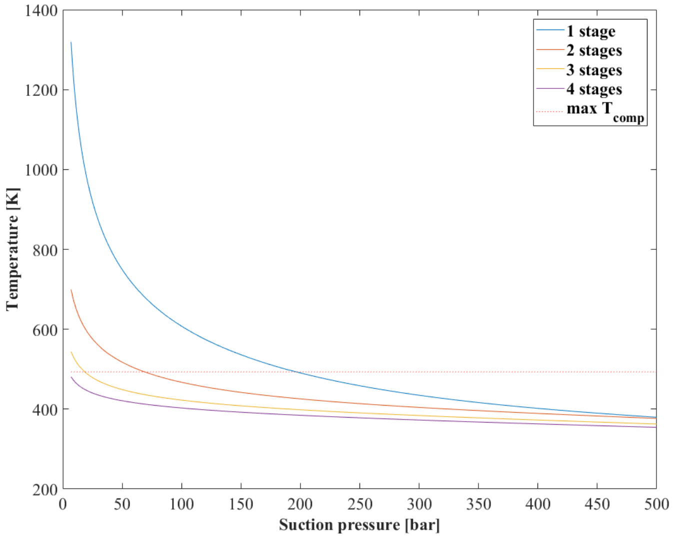

Figure 4.27: (Multi-) stage compression discharge temperature for high pressure storage with isentropic efficiency as function of pressure ratio

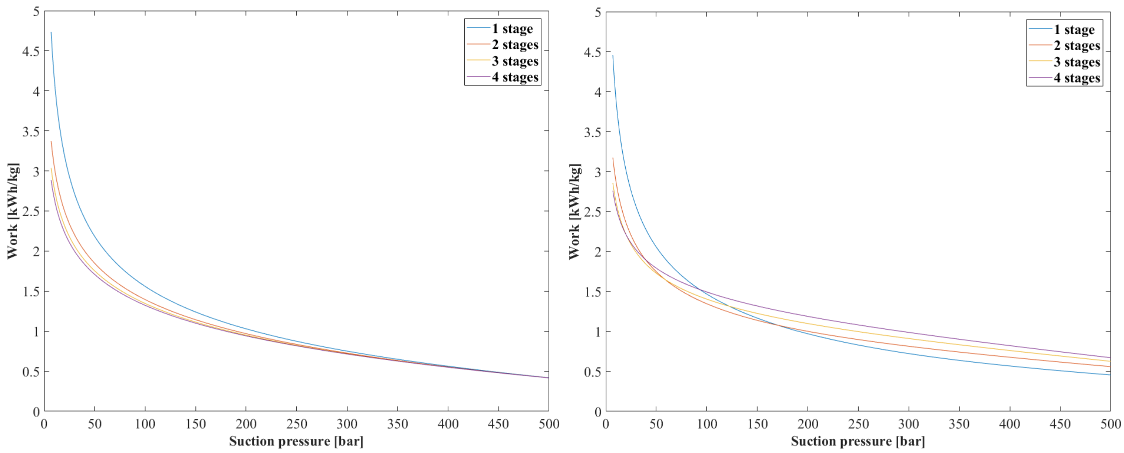

(a) Constant isentropic efficiency

(b) Isentropic efficiency as function of pressure ratio

Figure 4.26: (Multi-) stage compression work for filling high pressure storage as function of suction pressure for varying isentropic efficiencies

In Section 4.3.4 the energy consumption for compression and cooling is given. These numbers are validated with real data from a refuelling station. The power use for compression was 2.5 kWh/kg and 7.5 kW for precooling. The compressor is only turned on for short moments and the value for compression is in agreement with the simulated value.

4.3.2 Hydrogen storage

In this section the mass and energy balances are given for the hydrogen storage vessels. In Section 4.3.4 more info follows on the dispensing and different sizes of storages. Hydrogen storage poses opportunities for different time-scales. Within a smaller (non-seasonal) time frame, storage at high pressure is favored as the density at 950 bar is roughly 20 times denser than at 30 bar. For liquid storage a complex liquefaction facility is needed with 30-40 % higher energy requirements for cooling (percentage of caloric value or lower heating value)[28]. Therefore, gaseous storage is more common. Research by the Department of Energy [12] suggests that the optimal storage capacity is about 30 % of daily hydrogen dispensed.

A buffer storage system may consist of several tanks, each operated within a specific pressure range. Upon filling and emptying of the storage vessels, temperature changes step in. The effects of several parameters, such as initial gas pressure and temperature, ambient temperature and different ramp rates needs to be carefully checked. Filling of the vessel results in increased pressure and temperature values, but during rush hour multiple refuellings result in large pressure and temperature drops potentially impacting vessel life-time, but also the cooling demand. The advantage of storage configurations consisting of multiple tanks is the lower cooling and compression requirements when compared to having a single larger storage tank [25]. Cascade vessels are switched when a certain pressure difference is reached after which the mass flow would be too small to speak of fast filling.

Generally speaking there are five types of tanks (type I to V). The first type is a metal tank made of aluminum or steel, whereas the second type has additional filament windings made of carbon fiber. Type III and IV tanks consist of a composite material (carbon fiber, CF) combined with a metal or polymer (thermoplastic) liner, respectively. The plastic liner ensures gas tightness and the carbon fiber increases strength and saves weight. The last storage, type V, is linerless and entirely made of composite material. To support high-pressure 700 bar dispensing mostly type IV cylinders are currently used [27], see Figure 4.28.

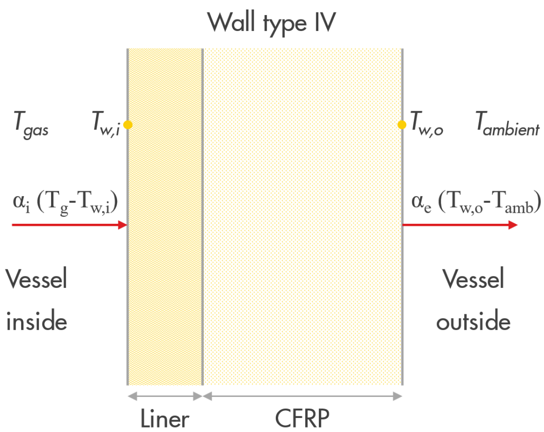

Figure 4.28: Schematic figure of vessel wall for type IV tank

The wall thickness of the vessel is calculated by the Mean Diameter formula (used in many standards in Europe), where P is the design pressure (MPa), D_{int} the internal diameter [m], σ_y the minimum yield stress [MPa] based on a maximum yield/tensile strength ratio of 0.9 and F the design stress factor (3/4) [29]:

$$\delta_{wall} = \frac{P_{design} * D_{int}}{20 * \sigma_y * F - P_{design}} \tag{4.11}$$

Table 4.6: SAE J2601 performance and safety limits for hydrogen vehicle tank fuelling

Parameter	Limit	Unit
Minimum gas temperature	-40	°C
Maximum gas temperature	85	°C
Minimum dispenser pressure	0.5	MPa
Maximum dispenser pressure (70 MPa NWP)	87.5	MPa
Maximum flow rate	60	g/s

Table 4.7: Vehicle tank 7kg - 70MPa (type IV) material properties SAE

Parameter	Polyethylene liner	Composite layer
Density $\frac{kg}{m^3}$)	945	1494
Specific Heat ($\frac{J}{kgK}$)	2100	1120
Thermal Conductivity ($\frac{W}{mK}$)	0.5	0.5

Table 4.8: Station storage vessel (type I to IV) material properties

Parameter	Type I	Type II		Type III		Type IV	
	Metal SS/Al	Metal Al	Comp CF	Comp CF	Liner SS/Al	Comp CF	Liner PE
Density ($\frac{kg}{m^3}$)	8000	2750	1494	1494	2750	1494	945
Specific Heat ($\frac{J}{kgK}$)	470	896	1120	1120	896	1120	2100
Thermal Conductivity ($\frac{W}{mK}$)	48	167	0.5	0.5	167	0.5	0.5

Depending on the pressure drop across the dispenser, the minimum working pressure of the high pressure bank should be around 850 bar, because the fuelling protocol indicates that the final pressure of the car is around this level. The vehicle tank has a temperature limit of 85 °C for two reasons. The tank material must remain unharmed from thermal degradation and the maximum working pressure in the tank during refuelling is not allowed to exceed 125 % of the nominal working pressure when filling the tank to 100 % SoC [30].

The State-of-Charge of storage tank is given in Eq. 4.13, where m_{min} is the multiplication of the storage volume and the minimum density based on the lower pressure limit in the tank at atmospheric temperature. The same holds for m_{max} based on the upper pressure limit of the storage. The corresponding density is calculated via a real gas equation, where the compressibility factor Z describes the deviation from ideality and Z a function is of (p, T), see appendix A:

$$Z = \frac{pV}{RT} \tag{4.12}$$

The SoC is then defined as:

$$SoC = \frac{m_s - m_{min}}{m_{max} - m_{min}} \tag{4.13}$$

The mass balance is given in its simplest form, where the input/output of the storages may be discontinuous time functions:

$$\frac{dm_s}{dt} = m_{in} - m_{out} \tag{4.14}$$

Determining the temperature differential in the storage tank starts from finding the new gas density,

$$\rho^{i+1} = \frac{m_s^i + \frac{dm_s}{dt}}{V_s} \tag{4.15}$$

and applying the energy equation, to express the heat transfer through the vessel wall, the in- and outflow of hydrogen in the form of internal energy, and the flow effects of both streams:

$$\frac{dE}{dt} = \dot{Q} - \dot{W} + \dot{m}_{in}(u + \frac{1}{2}v^2 + gz + \frac{P}{\rho})_{in} - \dot{m}_{out}(u + \frac{1}{2}v^2 + gz + \frac{P}{\rho})_{out} \tag{4.16}$$

It is assumed that changes in potential and kinetic energy as negligible and that there is no additional work term. The assumption that kinetic energy can be neglected results in an overestimation of the mean internal energy and thus the temperature of the gas [31]. Then further simplifying, with $h = u + Pv = u + \frac{P}{\rho}$, gives:

$$\frac{dm_s u_s}{dt} = \dot{Q} + \dot{m}_{in}h_{in} - \dot{m}_{out}h_{out} \tag{4.17}$$

As both m$_s$ and u$_s$ are functions of time the first term is split by the product rule:

$$m_s\frac{du_s}{dt} + u_s\frac{dm_s}{dt} = \dot{Q} + \dot{m}_{in}h_{in} - \dot{m}_{out}h_{out} \tag{4.18}$$

The term that was not considered yet, $\dot{Q}$, resembles the heat loss from the gas volume to the environment and greatly depends on the gas to storage wall heat convection, heat conduction through the vessel wall and finally convection to the surroundings.

The governing equation for heat conduction here is the Fourier's equation in x direction:

$$\frac{\partial T}{\partial t} = \alpha\frac{\partial^2 T}{\partial x^2} \tag{4.19}$$

Many steady state and transient heat convection and conduction problems can be solved analytically. In this case, however, we need a numerical solution method to solve the heat transfer through a hydrogen storage tank wall. A finite-difference method is used (Mills [32]), starting by discretizing the spatial and time axis to create several nodes together in a mesh. The difference equations are created by approximating the heat conduction equation (Eq.4.19), which is in differential form, with finite differences. The conduction in the tank walls is assumed to be mono-dimensional as the tanks are designed such that the wall thickness is small compared to the curvature of the tank. The unsteady conduction takes place without internal heat generation and constant thermal properties are considered for this problem.

The principle of energy conservation for the control volume, of size ΔxΔyΔz, is shown in fig. 4.29, where it is discretized in Δx. West (W) and East (E) denote the faces of the element. Time is discretized in steps of Δt, from the current time (i) to the next step (i+1). The change of internal energy in time by heat conduction for the control volume is then:

$$\Delta U = \dot{Q}\Delta t \tag{4.20}$$

$$\rho c(\Delta x \Delta y \Delta z)(T_m^{i+1} - T_m^i) = \dot{Q}_W \Delta t - \dot{Q}_E \Delta t \tag{4.21}$$

where the conduction and heat fluxes are taken at time step i in order to make the final equation for T_m^{i+1} explicit:

$$\dot{Q}_W \Delta t = -k\frac{T_m^i - T_{m-1}^i}{\Delta x}(\Delta y \Delta z)\Delta t \tag{4.22}$$

$$\dot{Q}_E \Delta t = -k\frac{T_{m+1}^i - T_m^i}{\Delta x}(\Delta y \Delta z)\Delta t \tag{4.23}$$

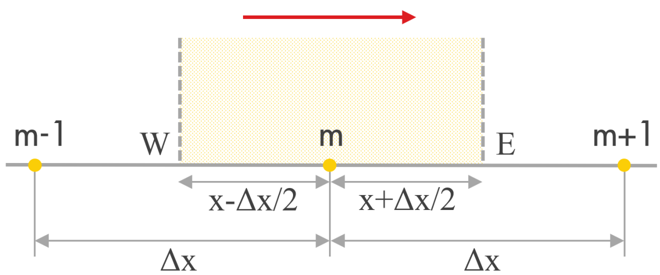

Figure 4.29: Finite control volume 1D unsteady conduction

After substituting Eq. (4.22, 4.23) and introducing the Fourier number in Eq. 4.21, this gives an equation for the temperature at node m at the next time step (i+1):

$$T_m^{i+1} = Fo(T_{m-1}^i + T_{m+1}^i) + (1 - 2Fo)T_m^i \tag{4.24}$$

where $Fo = \frac{\alpha \Delta t}{\Delta x^2}$ and $\alpha = \frac{k}{c\rho}$. The Fourier modulus, a dimensionless number for transient heat conduction, is the ratio of the conductive transport rate to the heat storage rate, whereas the thermal diffusivity or rate of heat transfer is described by α in terms of the ratio of thermal conductivity (k) by density (ρ) and specific heat capacity (c) of the material. Following the procedure by Mills [32] a nodal mesh can be constructed, after which it becomes clear that the temperatures at the boundary nodes 0 and M depend on the specified boundary conditions, see Figure 4.30. Furthermore, the Fourier number imposes an important convergence requirement for stability of the solution:

$$Fo \leq \frac{1}{2} \tag{4.25}$$

Then the time step follows depending on the chosen size of Δx:

$$\Delta t \leq \frac{\Delta x^2}{2\alpha} \tag{4.26}$$

At boundary nodes 0 and M a convective boundary condition is needed,

$$-k\left.\frac{\partial T}{\partial x}\right|_{x=0\,or M} = h_c(T_{amb} - T(x = 0\,or M, t)) \tag{4.27}$$

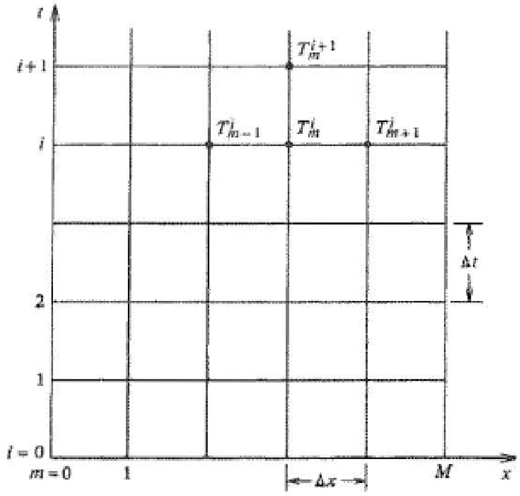

Figure 4.30: Nodal mesh 1D unsteady conduction (Mills [32])

corresponding to the finite control volume depicted in fig. 4.31, and an energy balance this gives:

$$\rho c \frac{\Delta x}{2}(\Delta y \Delta z)(T_0^{i+1} - T_0^i) = k(\Delta y \Delta z)\frac{T_1^i - T_0^i}{\Delta x}\Delta t + h_c(\Delta y \Delta z)(T_e^i - T_0^i)\Delta t \tag{4.28}$$

After rearranging:

$$T_0^{i+1} = 2Fo(T_1^i + BiT_e^i) + (1 - 2Fo - 2FoBi)T_0^i \tag{4.29}$$

where Bi is the Biot number, defined as $Bi = \frac{h_c \Delta x}{k}$, representing the ratio of heat transfer resistances in the material and at its surface. Small Biot values indicate fast internal heat conduction relative to the convection at its surface resulting in uniform temperatures in the material, whereas large numbers show non-uniform temperature fields inside the material. The stability criterion is different this time and more strict, dependent on the Biot number:

$$Fo \leq \frac{1}{2(1 + Bi)} \tag{4.30}$$

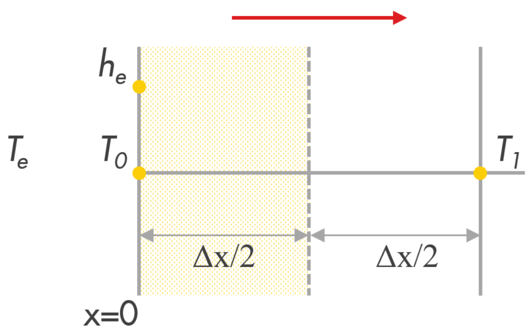

Figure 4.31: Finite control volume 1D convective boundary condition

The heat flow from the storage tank is simply (h is heat transfer coefficient):

$$Q = -hA_s(T_s - T_{amb}) \ with \ \frac{1}{h} = \frac{1}{h_{int}} + \frac{1}{h_{wall}} + \frac{1}{h_{ext}} \tag{4.31}$$

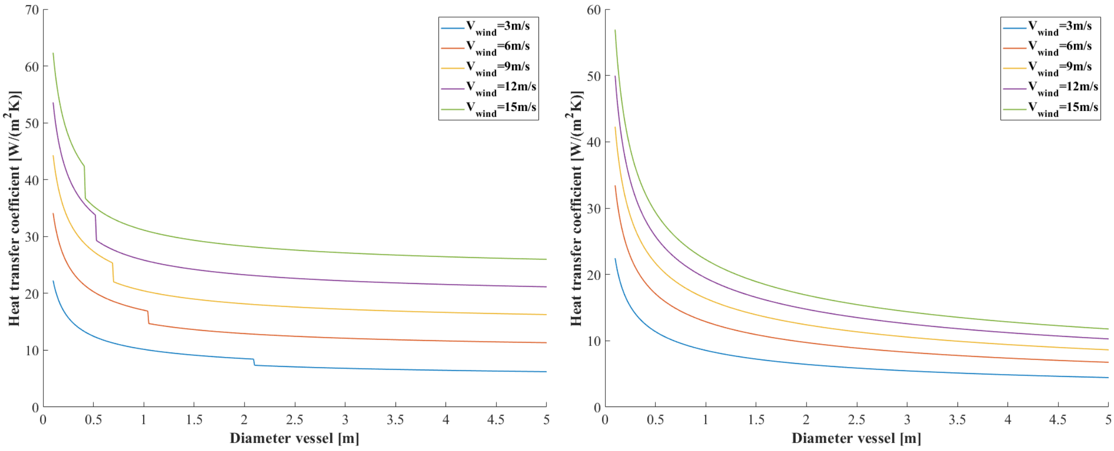

(a) Churchill-Bernstein relation **(b) Bourgeois et al.**

Figure 4.32: External convective heat transfer coefficient for various wind speeds and vessel diameters

Calculation of the stationary storage tank heat transfer consists of convective, conductive and radiative elements. The stationary storage tanks, stainless steel type I, conduct heat at a high pace (thermal conductivity $k_{cs} = 48\frac{W}{mK}$). For convection it is assumed to have an external forced flow with an isothermal surface and wind-speeds of 16 KPH or 4.4 m/s (according to Dutch average weather data 1981-2010 [33]). The average heat transfer coefficient, h_c, is calculated by finding the Nusselt number, which depends on the Prandtl number and the Reynolds number. The Reynolds number is ($\nu_{air} = 1.568 * 10^{-5}\frac{m^2}{s}$, U is flow velocity [m/s] and D is outside diameter [m]):

$$Re_D = \frac{UD}{\nu} \tag{4.32}$$

The Prandtl number is the ratio of momentum or viscous diffusivity to thermal diffusivity and depends only on the fluid ($\alpha = 22.07 * 10^{-6}\frac{m^2}{s}$):

$$Pr_{air} = \frac{\nu}{\alpha} \tag{4.33}$$

Then the average Nusselt number is given by the Churchill-Bernstein relation [32], which together with Equation 4.38 leads to Figure 4.32a:

$$\overline{Nu}_D = 0.3 + \frac{0.62Re_D^{1/2}Pr^{1/3}}{[1+(0.4/Pr)^{2/3}]^{1/4}}; \quad Re_D < 10^4 \tag{4.34}$$

$$\overline{Nu}_D = 0.3 + \frac{0.62Re_D^{1/2}Pr^{1/3}}{[1+(0.4/Pr)^{2/3}]^{1/4}}[1+(\frac{Re_D}{282.000})^{1/2}]; \quad 2*10^4 < Re_D < 4*10^5 \tag{4.35}$$

$$\overline{Nu}_D = 0.3 + \frac{0.62Re_D^{1/2}Pr^{1/3}}{[1+(0.4/Pr)^{2/3}]^{1/4}}[1+(\frac{Re_D}{282.000})^{5/8}]^{4/5}; \quad 4*10^5 < Re_D < 5*10^6 \tag{4.36}$$

An alternative correlation for the Nusselt number, without discontinuities, is given here [34], leading to Figure 4.32b:

$$\overline{Nu}_D = (0.4Re_D^{1/2} + 0.06Re_D^{2/3})Pr_{air}^{0.4} \tag{4.37}$$

From the Nusselt number the external convective heat transfer coefficient can be calculated:

$$\overline{h}_D = \frac{\overline{Nu}_D k_{air}}{D_{ext}} \tag{4.38}$$

Table 4.9: Air properties at T=300K

Parameter	Value
Density ($\frac{kg}{m^3}$)	1.177
Prandtl number (Pr)	0.71
Kinematic viscosity ($\frac{m^2}{s}$)	$1.568 * 10^{-5}$
Thermal Conductivity ($\frac{W}{mK}$)	$2.624 * 10^{-2}$

The internal heat convection coefficient is based on a selection of experimental studies around high pressure tank fillings. Even though various correlations for the Nusselt number are widely used, the results heavily depend on the local Reynolds numbers in the vicinity of the cylinder wall and on the geometry of the vessel. Hence, the internal heat convection coefficient in this model is taken from literature and assumed to be in the range of 100-200 W/(m^{2}K) [35]. Other reports give even wider values varying between 150 and 500 W/(m^{2}K) [22; 34]. It will be seen later that the internal heat convection coefficient contributes only little in the heat transfer resistance. The hydrogen is considered to be well stirred within the tank. Disclaimer here is that these values are based on rather small volumes (up to 200 L), whereas a large stationary storage vessel at low pressure easily is 10-100 times larger. In that case, the well-stirred assumption becomes weaker, as the forced convective inflow of hydrogen spreads less well in a large tank. Moreover, other effects such as buoyancy influences are likely to grow in importance and a mix of forced and natural convective forces could be considered. Woodfield et al. [36] proposes a Nusselt correlation consisting of both natural and forced convective terms, where constants a, b, c, d are related to tank geometry and orientation, and flow characteristics inside the vessel, which need to be gathered from experiments as they're not yet given by the report:

$$\overline{Nu}_{int} = aRa^b + cRe^d \tag{4.39}$$

The internal heat transfer coefficient is different during filling and emptying of the storages. For the latter case the natural convective heat transfer coefficient is calculated. The coefficient is roughly estimated by assuming that the inside cylinder wall is a flat vertical plate. The Grashof ($Gr_D = \beta \Delta T g D^3/\nu^2$) and Rayleigh ($Ra_D = Gr_D * Pr$) numbers are used together with correlations from Churchill and Usagi for the Prandtl number function, and Churchill and Chu for the average Nusselt number for laminar flow over height D [32]:

$$\Psi = (1 + (\frac{0.492}{Pr})^{9/16})^{-16/9} \tag{4.40}$$

$$\overline{Nu}_D = 0.68 + 0.670(Ra_D\Psi)^{0.25}; Ra_D \leq 10^9 \tag{4.41}$$

$$\overline{h}_D = \frac{k\overline{Nu}_D}{D} \tag{4.42}$$

After comparing several vessel diameters, pressure and temperature levels, the internal heat transfer coefficient is estimated at 25 $W/(m^2K)$.

The radiative contribution could be simply calculated by assuming that the tank is located outside and that its size is convex and small to its environment with ϵ the emissivity of the tank, σ the Stefan-Boltzmann constant and $T_{e,ext}$ the external wall temperature:

$$h_{rad} = \epsilon\sigma(T_{amb}^4 - T_{w,ext}^4) \tag{4.43}$$

But the contribution is small, less than 10 %, according to Bourgeois et al. [34] and therefore left out of further consideration.

All heat transfer coefficients are then compared and visualized in Figure 4.33. The heat transfer resistance, defined as one over the heat transfer coefficient, is for a tank type IV mostly affected by the wall conduction resistance. This in contrast to type I storage, which is mostly being affected by the external convective resistance, due to its higher conductive capacity. It is simple to notice that the internal convection coefficient is of less importance to the overall heat transfer from gas to its surroundings.

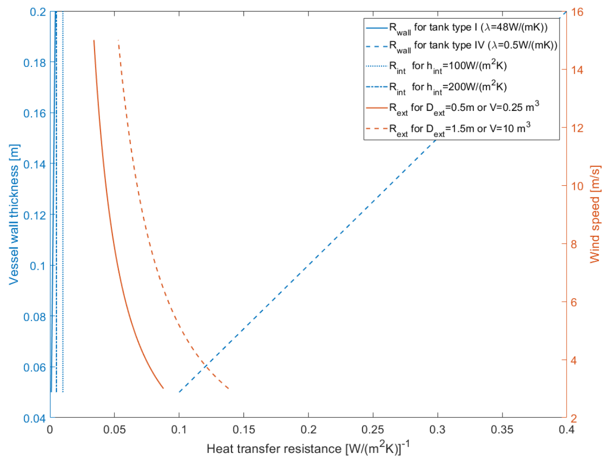

Figure 4.33: Comparison of internal/external convective and wall conductive heat transfer coefficients for a 0.25m^3 and 10m^3 storage tank

The behavior of vessel types I and IV are simulated for various heat transfer models and mass flows. The first heat model is the adiabatic case, where no heat flows through the vessel's walls. The second model only accounts for gas and ambient temperature, whereas the third model also accommodates for the thermal mass of the wall. The simulated mass flow can be seen in Figure 4.34 and the resulting temperature and pressure profiles in Figures 4.35a, 4.35b, 4.36a, 4.36b. The figures show that large differences exist between the models and the 3-temperature model (where thermal mass of wall is included) should be taken. As expected there are no differences between tank type I and IV for the adiabatic case. For the 2-temperature model the metal storage (type I) reaches less high temperatures during filling than type IV and is quicker in settling at the ambient temperature after filling, indicating a lower conductive wall resistance. The temperature of the wall elements is shown in Figures 4.37a and 4.37b.

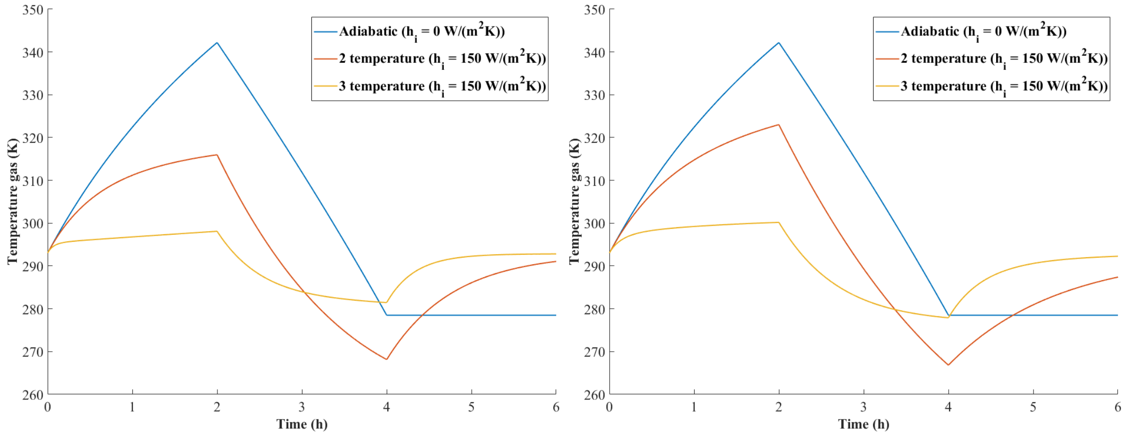

(a) Type I tank **(b) Type IV tank**

Figure 4.35: Comparison storage models: tank temperature (V=5m^3, P=300bar, $\dot{m}_i$=0.005kg/s)

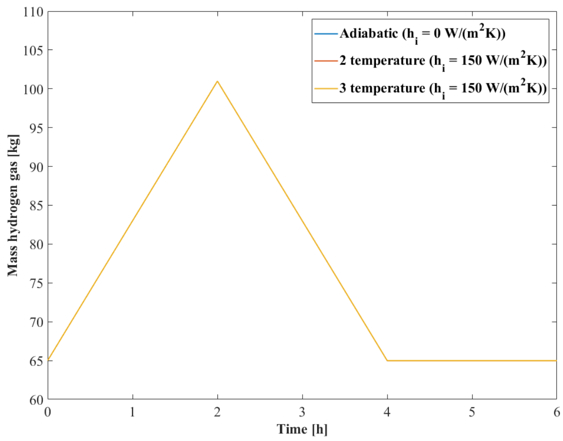

Figure 4.34: Comparison storage models: hydrogen mass profile (V=5m^3, P=300bar, $\dot{m}_i$=0.005kg/s)

4.3.3 Throttle

Hydrogen gas leaving the storage vessel should be throttled to dispensing pressure. Typically, when a vehicle arrives for refuelling, the dispenser connects to the low-pressure vessel in the buffer storage system, regulating the flow to keep it below the maximum allowable flow of 60 g/s and above the cascade switch point (which varies per operating strategy, but is typically 0.1 kg/min). Once the flow between the connected bank and vehicle tank drops below the cascade switch point (i.e. as the pressures are almost equal and the mass flow is low), the dispenser connects to the next cascade bank, where H_2 is stored at a higher pressure. This routine of sequentially connecting each cascade bank with higher-pressure H_2 to the vehicle tank is continued until the vehicle tank is filled with 5 kg of hydrogen or the flow from the highest-pressure bank is below a predetermined minimum value. Typically, the buffer storage vessels are maintained within a definite range to ensure that the vehicle tank receives 5 kg of H_2 after connecting to the

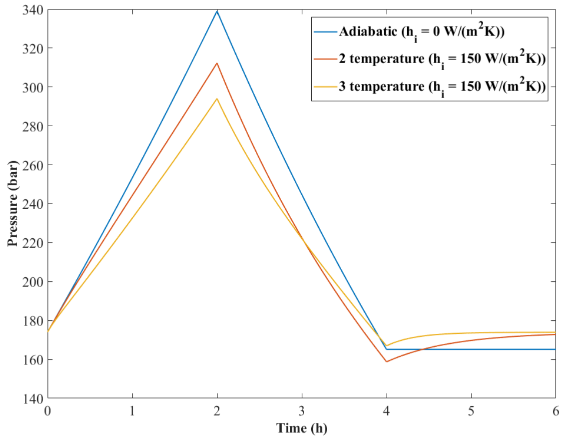

(a) Type I tank

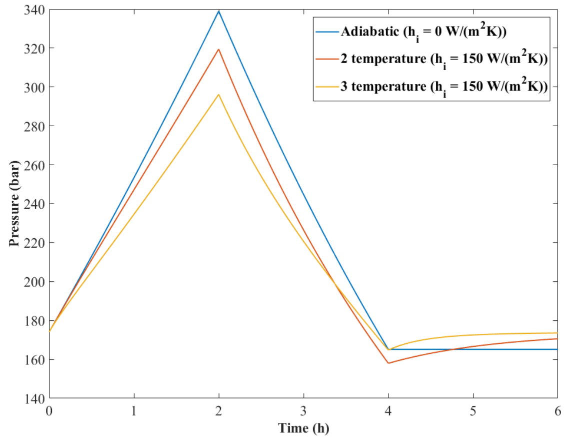

(b) Type IV tank

Figure 4.36: Comparison storage models: tank pressure (V=5m^3, P=300bar, $\dot{m}_i$=0.005kg/s)

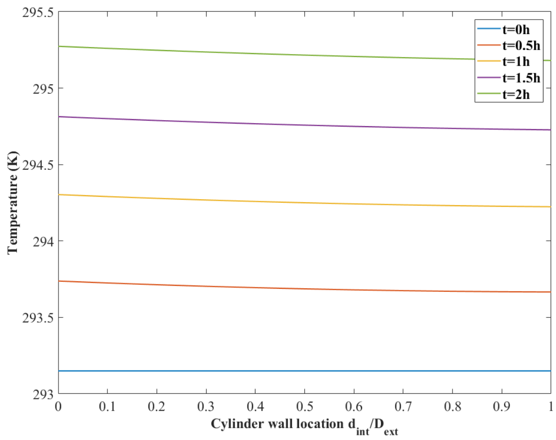

(a) Type I tank

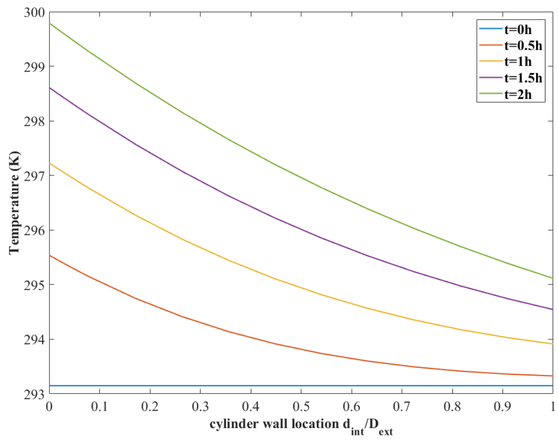

(b) Type IV tank

Figure 4.37: Comparison storage models: wall temperature (V=5m^3, P=300bar, $\dot{m}_i$=0.005kg/s)

high-pressure bank.

Before the hydrogen is dispensed, the gas must be expanded over an expansion valve or throttling device to meet the pressure of the car. Additional pre-cooling to -40°C is needed to limit the final temperature of the vehicle tank. The hydrogen is throttled under isenthalpic expansion from a high pressure to a level slightly above the car's pressure recognizing any pressure losses along the way. The thermodynamic process involved here is called the Joule-Thomson effect and explains the temperature change of a real gas upon expansion, which is quantified by the Joule-Thomson coefficient [8]:

$$\mu_{JT} = \left(\frac{\partial T}{\partial P}\right)_H \tag{4.44}$$

A positive coefficient indicates the effect of cooling, whereas a negative value corresponds to heating of the gas.

For a control volume enclosing a throttling device, the energy and mass balances are,

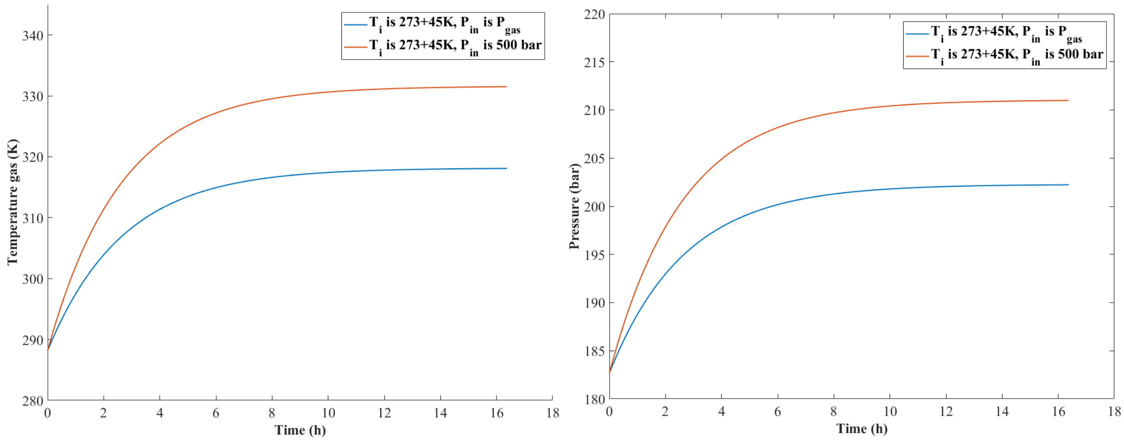

(a) Temperature effect **(b) Pressure effect**

Figure 4.38: Joule-Thomson effect with constant mass in- and outflow

at steady state:

$$\dot{m}_{in} = \dot{m}_{out} \tag{4.45}$$

$$\frac{dE}{dt} = \dot{Q} - \dot{W} + \dot{m}_{in}(h + \frac{V^2}{2} + gz) - \dot{m}_{out}(h + \frac{V^2}{2} + gz) = 0 \tag{4.46}$$

We assume that there is no heat transfer ($\dot{Q}$) and the potential and kinetic energy effects are also negligible, then

$$h(T, P)_{in} = h(T, P)_{out} \tag{4.47}$$

All the inlet conditions are known, as is the pressure outlet. The outlet temperature is then easily calculated from the known enthalpy value using the NIST tables [37].

The Joule-Thomson contribution becomes clear by showing its effect in filling a hydrogen tank. For a typical 300 bar adiabatic vessel with equal mass flowing in as out the temperature of the vessel settles at the inflow condition. The temperature of the inlet stream is the intercooling temperature of 318 K. Then the pressure of the incoming mass flow, originally slightly above the original tank pressure level, is changed to an arbitrary higher value (e.g. 500 bar). In the original setting the temperature of the tank settled at the intercooling level and the pressure at 202 bar. However, in the second scenario (with P$_i$ is 500 bar) the temperature and pressure in the tank settle at 331 K and 211 bar, respectively. Throttling the gas from 500 to 211 bar with T$_i$ is 318 K gives a temperature value of 331 K, which is identical to the value found by manipulating the storage inflow pressure. This clearly shows the Joule-Thomson heating effect of expanding hydrogen from 500 to 211 bar.

In order to follow the specified filling protocols defined by SAE, the mass flow entering the vehicle tank needs to be controlled by the same throttling valve as mentioned before to regulate the pressure. The relationship between the pressure and the velocity of the gas is described by Bernoulli's principle, which is derived from the energy conservation principle. For an incompressible, steady-state, inviscid, laminar flow the following holds for points on a streamline:

$$p_1 + \frac{1}{2}\rho V_1^2 = p_2 + \frac{1}{2}\rho V_2^2 \tag{4.48}$$

Together with continuity and the orifice flow coefficient, C, defined as $C = \frac{C_d}{\sqrt{1-\beta^4}}$ this becomes:

$$\dot{m} = CA_2\sqrt{2\rho(p_1 - p_2)} \tag{4.49}$$

where β is the ratio of the restriction diameter to the pipe diameter ($\beta = \frac{d}{D}$). The discharge coefficient (C_d) accounts for all the assumptions initially made around irreversibilities (inviscid, friction-less, turbulent etc.). For a reversible process C_d=1.
Eq. 4.49 can be used for compressible flow as well, if an additional factor is applied for the compressibility of the hydrogen gas. However, for small values of β the mass flow depends on a dynamic condition called choked flow, where the flow velocity in the valve outlet reaches Mach 1 and the mass flow no longer depends on the downstream pressure, but on the critical pressure [38], defined as:

$$p_c = p_1(\frac{2}{\gamma + 1})^{\frac{\gamma}{\gamma-1}} \tag{4.50}$$

When the desired downstream pressure (p_2) is lower than the critical pressure (P_c) choking occurs:

$$\dot{m} = CA\sqrt{\gamma\rho p_1(\frac{2}{\gamma + 1})^{\frac{\gamma+1}{\gamma-1}}} \tag{4.51}$$

In the second case, for $p_2 \geq p_c$, the unchoked mass flow becomes:

$$\dot{m} = CA\sqrt{2\rho p_1(\frac{\gamma}{\gamma - 1})((\frac{p_2}{p_1})^{\frac{2}{\gamma}} - (\frac{p_2}{p_1})^{\frac{\gamma+1}{\gamma}}} \tag{4.52}$$

The size of the required restriction diameter is then under choking,

$$d = \sqrt{\frac{1}{0.25\pi}\frac{\dot{m}}{C\sqrt{\gamma\rho p_1(\frac{2}{\gamma+1})^{\frac{\gamma+1}{\gamma-1}}}}} \tag{4.53}$$

and under non-choked fluid conditions:

$$d = \sqrt{\frac{1}{0.25\pi}\frac{\dot{m}}{C\sqrt{2\rho p_1(\frac{\gamma}{\gamma-1})((\frac{p_2}{p_1})^{\frac{2}{\gamma}} - (\frac{p_2}{p_1})^{\frac{\gamma+1}{\gamma}}}}} \tag{4.54}$$

The results for the orifice diameter at constant specific heats and $T_{amb} = 25°$ C are:

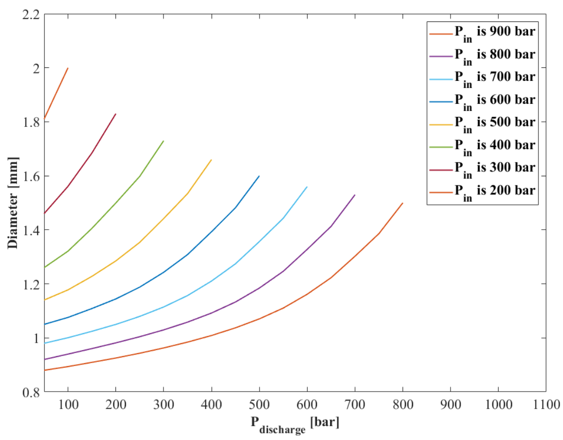

Figure 4.39: Orifice diameter for compressible flow

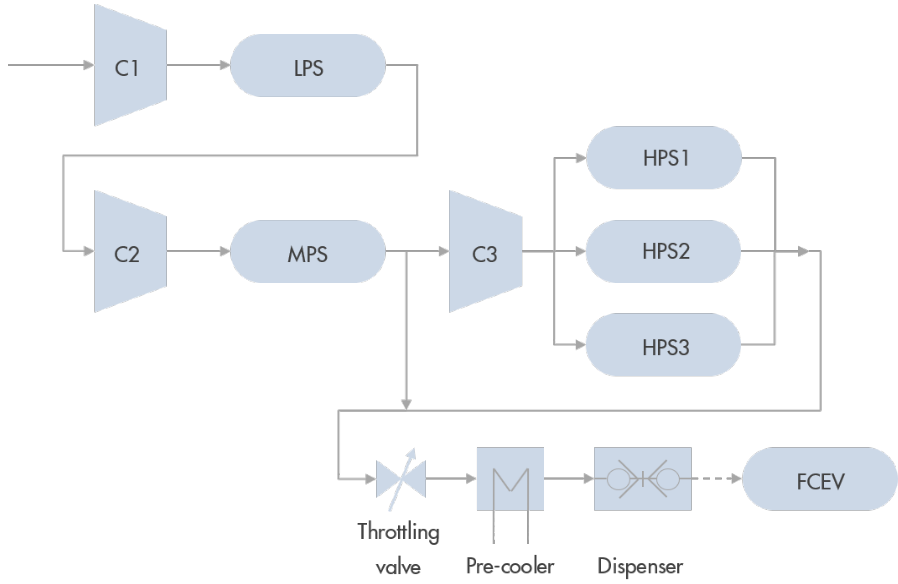

Figure 4.40: Diagram of cascade storage system, compressors, pre-cooler, reduction valve and dispenser

Table 4.10: Fuelling parameters from SAE J2601 [15]

Parameter	Value	Unit
Initial hydrogen mass in tank ($T_{amb} = 20°C$)	2	kg
Initial pressure in tank (T_{amb})	152	bar
Pressure ramp rate (T_{amb})	285	bar/min
Mass flow limit	60	g/s
Final vehicle mass	7	kg
Final vehicle pressure (T_{amb})	700	bar
Final vehicle pressure ($T_{H_2} = 85°C$)	875	bar

4.3.4 Dispenser

In this section more info on the refuelling procedure and dispenser is given. The setup is shown in Figure 4.40. Table 4.10 gives the fuelling parameters taken from the SAE standard.

The cascade procedure in dispensing (i.e. filling from multiple vessels) lowers the station's energy consumption. As mentioned before, Rothuizen and Rokni [23] showed that the total energy demand for cooling and compression can be reduced by respectively, 12% and 17%, and that the high pressure hydrogen storage is reduced by 20%. Farzaneh-Gord et al. [39] analyzed the filling process with buffer and cascade storage systems and concluded that the former holds the disadvantage of generating 55% more entropy compared to cascade filling, reflecting higher compressor work input. Interest lies in finding the optimal configuration of the cascade storage system. Cascade storage imposes fuelling delays when switching storage [40]. This effect is not taken into account in the model.

Different configurations of storage tanks and pressures are tested. Filling occurs only from medium (300 or 500 bar) and high pressure (950 bar) storages. Up to 3 high pressure banks may be selected, where each bank consists of smaller cylinders of 50 L. The vessel volumes were selected to be just able to match the demand for one hydrogen vehicle refuelling of 5 kg. The total power is the sum of the compression power, 5 % of the intercooling duty and the precooling duty divided by its coefficient of performance (Coefficient Of Performance, COP, is 1.1 at T_{amb} is 20°C, Figure 4.44a). Figure 4.41 shows the savings per category when changing between vessel configurations. Then for the most optimum configuration Figure 4.42 holds the pressure levels of the different storage vessels during refuelling. It clearly shows the cascading effect when the pressure difference between car and stationary storage becomes too small and vessels are switched.

Talpacci et al. [30] stated that cooling energy consumption can exceed 10 kWh/kg hydrogen for low station utilization, but that the amount of electrical energy for precooling is about 10 % of the total energy consumption for high utilization rates. This complies with the findings in this report, more info about the cooling in Section 4.3.5.

Table 4.11: Cascade configurations in increasing energy efficiency order and power for compression, intercooling and precooling

Configuration	Storage type and size (m^3)					Power
	300 bar	MPS 500 bar	HPS 1	HPS 2	HPS 3	(kWh/kg)
Base case	-	-	5	-	-	3.16
1	-	-	0.25	1	-	3.10
2	1	-	4.5	-	-	3.06
3	-	-	0.25	0.25	0.5	2.96
4	1	-	0.25	1	-	2.93
5	-	0.75	2	-	-	2.88
6	1	-	0.25	0.25	0.25	2.86
7	-	0.75	0.25	0.75	-	2.84
8	-	0.75	0.25	0.25	0.25	2.79

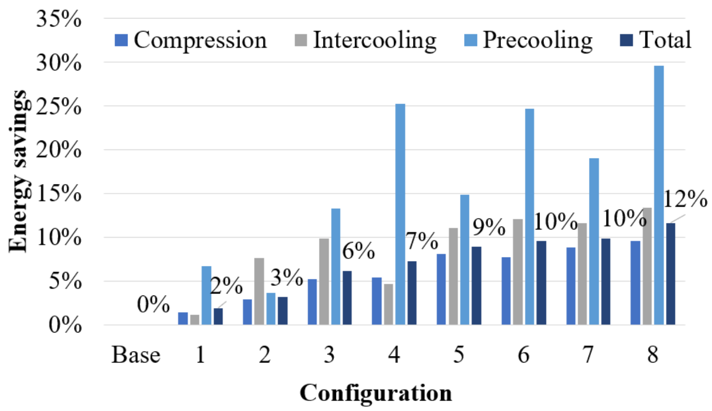

Figure 4.41: Comparison of cascade storage configurations

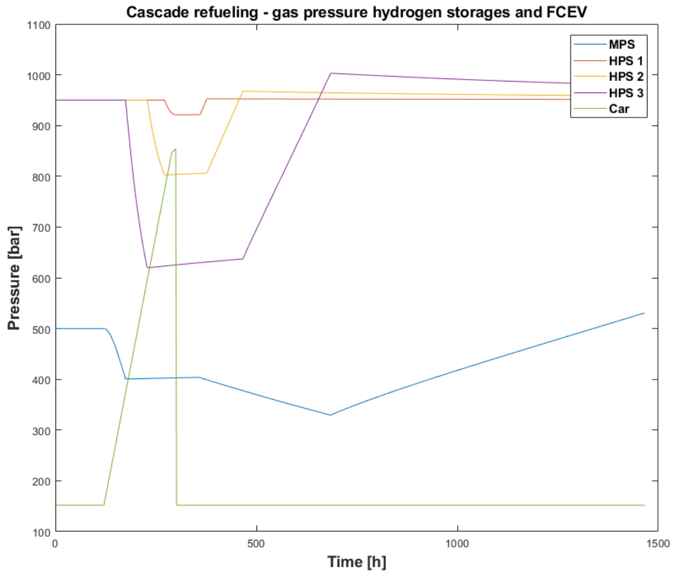

Figure 4.42: Pressure levels for cascade filling with configuration 8 from Table 4.11

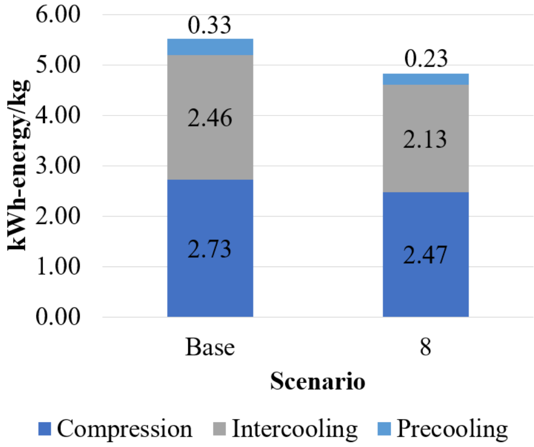

(a) Energy requirement

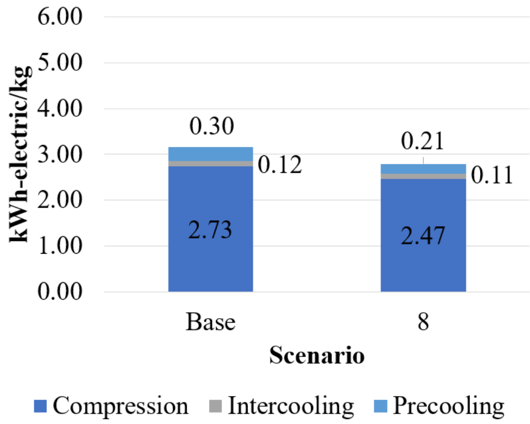

(b) Electric input

Figure 4.43: Comparision of (electric) energy requirements for compression and cooling in base case and cascade filling scenario eight 4.11

4.3.5 Heat exchanger

In this section more info is given on the cooling equipment. There are two cooling methods needed: compressor interstage cooling and pre-cooling. Between each compression stage the hydrogen is cooled by an interstage cooler in order to keep the compressor temperature within its design limits. And before the hydrogen is dispensed it must be cooled by the pre-cooler to protect the vehicle tank from overheating. The heat flow in the pipe from pre-cooler to dispenser is not taken into account.

Intercooling stages are needed to limit the compressor operating temperature due to heat production during hydrogen compression. The maximum allowed operating temperature for these compressors is around 220°C. Depending on the cooling method the intercooler power is estimated at 1-5 % of the compression work. The intercooler outlet temperature is set at 45°C.

Before the hydrogen gas is dispensed to the car's storage vessel, it needs to be cooled down in order to limit the temperature increase of the tank wall during fast filling. The gas heats up during refuelling due to two effects. The first one is that hydrogen is a non-ideal gas, which in this case means it heats up during the expansion from 950 bar to the pressure in the vehicle (which depends on the SoC and gas temperature). The gas heating is explained by the Joule-Thomson effect. Secondly, flow work effects exist when the gas is again compressed in the car storage, where pressure is rising. To accommodate for both effects the hydrogen is precooled to -40°C, according to the SAE J2601 standard. Xiao et al. [41] studied the effects of initial temperature, initial pressure and filling rate on the pre-cooling requirements and tank temperature limit of 85°C. Much heat needs to be removed from the hydrogen to reach the pre-cooling temperature and a large amount of work is required for the refrigeration cycle.

Comparing both cooling procedures, it is clear that precooling requires far more work input than intercooling, as the requested temperatures (-40°C) are well below ambient temperature.

The size of the precooler depends on the refuelling demand. The energy consumption of the cooler contributes to the operating cost of the station. The requirements are easily obtained from a simple energy balance that reduces to:

$$\dot{Q}_c = \dot{m}(h_{in} - h_{out}) \tag{4.55}$$

where the mass flow follows from the SAE J2601 standard and the in- and outflowing specific enthalpies are obtained from the pressure and temperature values at both pre-cooler in- and outlet. The outlet temperature is set at a specific chosen level in order to reduce the temperature build up in the vehicle tank and is put at -40°C. The outlet pressure depends on the cooler pressure drop and is less than 1 bar [42].

The amount of electrical energy consumed upon cooling is calculated from the Coefficient Of Performance (COP). This performance is defined as the ratio of heat (Q_c) removed by the system and the work (W) required to do so:

$$COP_{cooling} = \frac{Q_c}{W} \tag{4.56}$$

The COP is temperature dependent and decreases for higher ambient temperature [43]: The SAE J2601 standard sets the cooling requirement to be met within 30 seconds of refuelling [15]. Therefore the heat exchanger must be kept cold at -40 °C during the entire day in case a refuelling has to take place. The Argonne National Laboratory collected data from several hydrogen stations in California providing an estimate of the daily precooling electricity consumption when no refuellings were recorded. At 25 °C ambient temperature the average energy consumption (Q_c) was 54 kWh [43]. For low station utilization this consumption greatly affects the operating cost (or electricity consumption) per unit of hydrogen, whereas more dispensing leads to small contributions. Following the method of Xiao et al. [41] we can construct a relation between the cooling

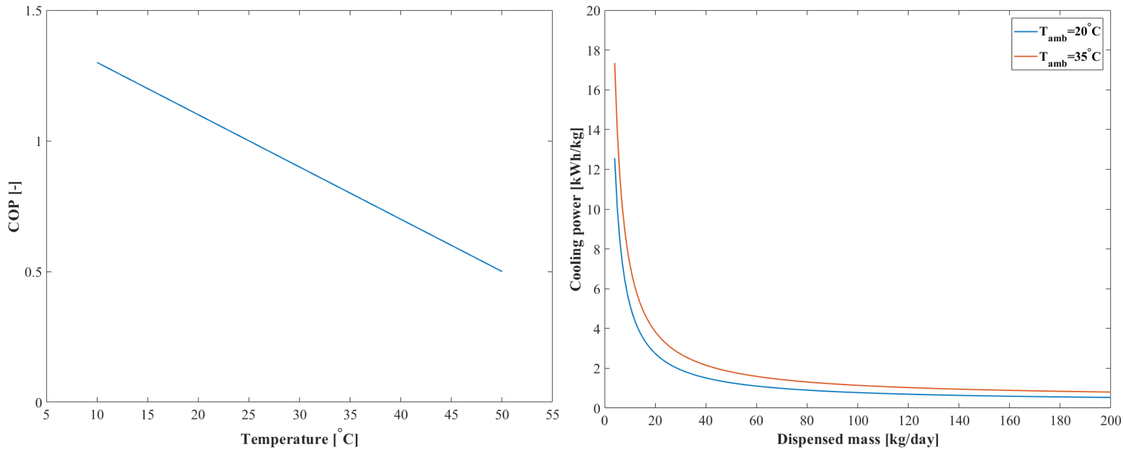

(a) Ambient temperature effect on Coefficient Of Performance [43]

(b) Precooling electricity consumption for different station utilizations

Figure 4.44: Precooling Coefficient-of-Performance and power consumption for different ambient temperatures

electricity consumption and the daily amount of hydrogen dispensed for different station utilization rates:

$$P_{cooling} = \frac{Q_v + \frac{Q_c}{m_{H2,day}}}{COP} \tag{4.57}$$

Where Q_v is 0.32 kWh/kg at ambient temperature T_{amb}=20°C and 0.37 kWh/kg at T_{amb}=35°C, see figure 4.44b. These values are slightly higher than the value (0.30 kWh/kg) found by the report, but can easily be explained by looking at the incoming hydrogen temperature. In the report the inflow temperature is 35°C, contrary to our case where the flow sometimes arrives with higher temperatures from the throttling device. The throttling discharge temperature varies between 10 and 65°C dependent on the storage and vehicle pressure ratio ($\frac{P_s}{P_{car}}$). During refuelling the station switches between storages to meet the rising car pressure. Figure 4.45 shows for an arbitrary throttling activity the effect of cascading. The starting pressure in the first station storage is still high, but slowly reduces when hydrogen is flowing out. Therefore, the throttling temperature also decreases. After a while, the pressure difference with the car becomes to small and the mass flow to slow. Then the cascade switches to a higher pressure storage and continues refuelling. The throttling temperature is then much higher due to the increase in pressure difference. This procedure is characteristic for cascading.

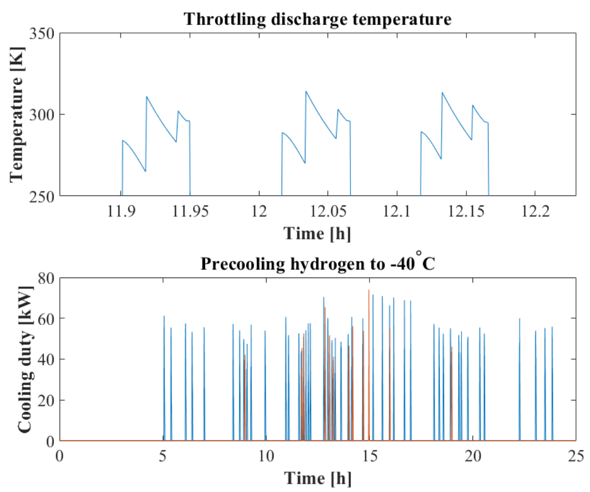

Figure 4.45: Discharge temperature throttling device and precooling duty (Q_{kg})

4.4 Electric system

An overview of the electric system is given in this section. Our interest goes out to the different power sources and loads on the Hydrogen Refuelling Station. The supply of power includes the CH2P production system (net), battery (discharge mode) and grid connection (power consumption). The total load of the station contains the retail station (lights, refrigeration, heating etc.), hydrogen equipment (compression, cooling), EV-charging, battery (charge mode) and grid connection (power export). Both the battery and grid connection are optional, dependent on the station location and economics. The recent growing mismatch between supply and demand in certain power markets (e.g. California) ask for mitigating strategies, including energy storage and energy demand management. Accompanying opportunities and risks should be investigated.

The gross power produced by the CH2P unit is maximum 500 kW (see Table 4.4) and in direct-current (DC) form. Which is ideal for the fast-charging demand of Electric Vehicles and the stationary battery storage (both DC operated). Sometimes additional electronic equipment or expansions are needed for the grid station interconnection. These are left out of the analysis for this report.

The power grid transmits electricity via high-voltage transmission to its substations, where it is reduced to medium voltage (primary) and low voltage (secondary, under 2400 V). Low voltage lines carry power from the distribution transformer to the hydrogen station. If a new station is to be built, or an existing station's power supply is insufficient these grid lines could be upgraded. As mentioned earlier, additional electrical equipment could also be necessary, such as an inverter to invert local DC current to Alternating-Current (AC) or a transformer to increase the AC to the grid. The standard grid connection is assumed to be 75 kW.

At certain daytimes the overall load of the grid is higher, called peak load, which often occurs twice per day and results in increased power prices, because of a larger demand and production mismatch. Another timing imbalance exists, however, where prices decrease rapidly. This phenomenon, called the Duck curve, is strongly linked

to the substantial increase of solar power production and the lack of cheap large scale energy storage in, for example, California [44]. Imbalances between power generation and consumption continuously exist, because of the intermittency of all the devices being used. Electricity grids sense shifts in frequencies, negatively affecting the stability of the grid. Grid operators continuously aim to match supply and demand to ensure stable power grids. Many transactions take place at the intra-day and day-ahead power markets to do so. Fluctuations in supply and demand shortly before use need to be handled by so called ancillary services:
- Reactive Power
- Frequency Regulation
- Spinning and Non-Spinning Reserves
- Black Start

Electric storage could be a good solution for higher power reliability and intermittent renewables by smoothing power differences and posing a chance to reduce grid congestion. Even though a battery is part of the HRS design, the opportunities of these services are complex and depend often on local regulations and are therefore disregarded in this report. For the station, storage mainly serves for locally matching production with demand. It takes the CH2P unit 40 minutes (FICTIVE) to change between modes. Whenever a BEV arrives electric storage is needed to provide power when the CH2P is starting up.

As a widely used technology for large scale storage applications different types of batteries exist (lithium, redox-flux). The battery characteristics are important to the simulation, including the C-Rate, defined as Power to Capacity ratio (kW/kWh), performance, and price. Until recently, lithium-ion technologies provided more than 95 percent of new energy storage applications [45] and they are applicable in both high power and high capacity use. Redox flow batteries (RFB) pose potential for large scale applications, but are currently unfavorable price-wise and because of their low energy density [46]. The C-Rate of the battery is set at two, or more to the spectrum of power-designed systems, mainly to provide high power to BEVs when the CH2P is increasing production [47].

The cueing procedure is set out in Section 4.1. Charging infrastructure operators aim for high occupancy rates and the number of chargers determines the average waiting time. There are two forms of charging, AC and DC charging. Following the German Federal Ministry for Economic Affairs and Energy, fast charging is defined as having chargers with power rates above 22 kW [48]. New charging infrastructure is very dependent on future power rates and battery sizes. In this model only DC fast charging of 150 kW is applied, because for the public charging infrastructure fast charging is most likely to become the standard [49]. Charge speed is influenced by voltage, battery pack capacity, State-of-Charge, battery temperature and the power level of the charger (e.g. insufficient grid connection) [50]. Charging at 50 kW is typically done at 400 V and 125 A, whereas charging of 150 kW has three times higher currents. It is clear that the infrastructure of electric vehicles could generate very high requests on energy.

Table 4.12: Charger characteristics [51]

Charging level	Voltage [V]	Typical power [kW]	Info
Level 1	120 V AC	1.2-1.8 kW	Residential US
Level 2	200-240 V AC	3.6-22 kW	Home, public
DC fast	400 V DC	>50 kW	Public

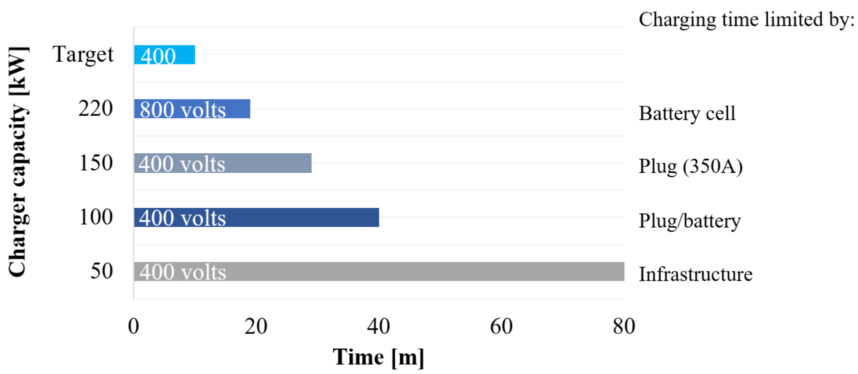

Figure 4.46: Charging time comparison for different charger capacities 80 % SoC and 400 km [51]

The procedure for calculating the battery and grid power levels is shown in Figure C.4. Important to notice is that the battery is used prior to the grid connection. When the battery is below a certain State-of-Charge then power is also provided by the grid. At some moments during the day there is a power surplus or shortage due to sudden load changes. For example, when several BEVs disconnect simultaneously and the CH2P unit is in high production mode, the battery and grid might be inadequately absorbing the surplus power. To solve this problem a flywheel or supercapacitor could be installed for rapid (dis-)charging. In the model the variable $P_{balance}$ captures this effect.

4.5 Other

4.5.1 Pressure drop

The pressure drop in the aforementioned system components has already been explained. At some locations a long distance pipe is needed to connect the storage and dispensing facilities with each other. Kuroki et al. [52] found that the filling pipes may be assumed a simple and straight pipe. Based on different diameters of the pipe the pressure drop can be calculated for varying mass flow. The pipe characteristics are:

Table 4.13: Pressure drop pipe properties

Quantity	Value	Unit
Pressure, P	950	bar
Inner diameter, d_i	0.010-0.012	m
Length, L	50	m
Roughness, r	0.025	mm
Mass flow, m	1-50	g/s
Dynamic viscosity μ	1.1e-5	Pa*s
Density ρ_{H2}	47.7	kg/m^3

Volume flow [m^3] is:

$$V = \frac{\dot{m}_{H2}}{\rho} \tag{4.58}$$

And the Reynolds number can be calculated by using the flow speed $v = \frac{V}{\frac{\pi}{4}d_i^2}$ and

$$Re = \frac{\rho v d_i}{\mu} \tag{4.59}$$

The implicit Colebrook-White equation for the friction factor is then approximated by the Haaland equation

$$\frac{1}{\sqrt{f}} = -1.8log(\frac{6.9}{Re} + \frac{r/D_h}{3.7}^{1.11}) \tag{4.60}$$

Which gives the pressure drop in the Darcy-Weisbach equation

$$dp = f\frac{L}{D_h}\frac{\rho v^2}{2} \tag{4.61}$$

in which D$_h$ is the hydraulic diameter, or for a circular pipe the internal diameter. Only the major losses are considered here, as minor losses such as valves, pipe bends, are to specific for this case.

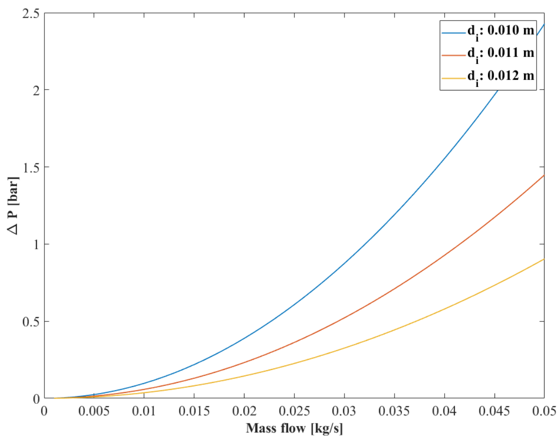

Figure 4.47: Pressure drop in 50 m steel pipe from storage to dispenser

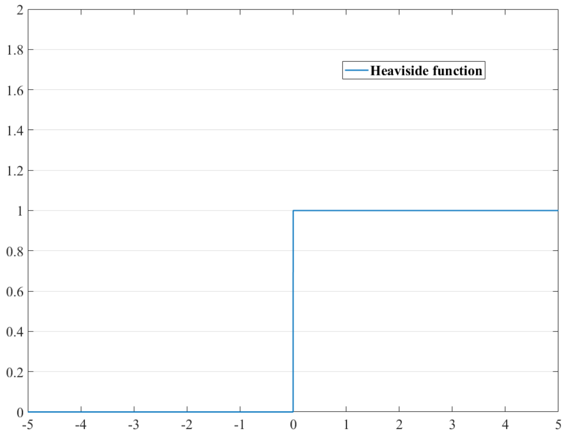

(a) **Heaviside or step function**

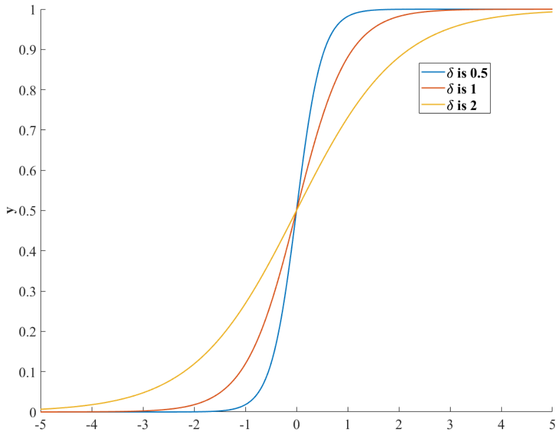

(b) **Smooth Heaviside**

Figure 4.48: Hyperbolic tangens used to smoothen Heaviside function (Eq.4.62)

4.5.2 Software

The model is written in MatLab. Each component uses at least two state properties (such as entropy, temperature, density, pressure) and evaluates based on the equations the quantities of interest. The backbone of the model are the mass and energy balances, in the form of differential equations. All the real gas effects have been calculated by using tables from the US National Institute of Standards and Technology [37]. The database provides fluid thermodynamic and transport properties (REFPROP) from two independent state properties.

A specific Ordinary Differential Equation (ODE) solver is chosen in MatLab to solve the integration procedure, namely the ODE113 solver, which is an explicit multistep predictor-corrector method based on the Adam-Bashforth and Adams-Moulton algorithms. The ODE solver is able to calculate an integration step, evaluate the tolerances and try smaller steps if the calculation was rejected. The variable step-size greatly improves the overall simulation time when compared to fixed-step methods.

Besides non-linear behavior the solver has to work with discontinuous (differential) equations. This effect is caused by time discretization and different configurations set by several conditional statements. Unfortunately the solver experiences heavy slowdown upon evaluating these discontinuities. A solution to this is achieved as follows.

The discontinuous behavior often equals the shape of a Heaviside (or step) function, which we now try to smoothen. The hyperbolic tangens is used, where δ is a parameter that controls the thickness of the transition region (Figure 4.48b).

$$\theta_\delta(t) = \frac{1}{2}(1 + tanh(\frac{t}{\delta})) \tag{4.62}$$

The former equation is adjusted to use it as well in a 'step down' situation:

$$y^i = min(y^{i-1}, y^{i+1}) + |y^{i+1} - y^{i-1}| * \frac{1}{2}(1 + sign(y^{i+1} - y^{i-1})tanh(\frac{t}{\delta})) \tag{4.63}$$

Optimization pitfalls may arise when dealing with the MatLab Optimization Toolbox, as the algorithms tend to exploit model weaknesses. Therefore, it is critical to define the correct problem formulation, pick the right optimization method and set up good control variables. Optimization can be classified by the type of problem, in this case constrained, single objective, nonlinear and discontinuous variables. The problem includes contradicting elements, meaning you cannot improve an objective without making another one worse (Pareto Optimal Point). Within the optimization function there is a penalty function that accounts for the Customer Satisfaction Index and should be higher than a minimum value (for example 95 %). The CSI reflects only the availability of hydrogen and power and not the availability of fuelling spots (latter is a design decision made before the optimization).

Within the MatLab Optimization toolbox the Genetic Algorithm is preferred for this problem, in order to make sure that the global minimum is found and not a local one. The Genetic Algorithm creates a random initial population and then creates more populations based on the score of each member. The best members are called 'elites' and transferred to the next population. The algorithm makes new members by 'mutation' (adjustments) or by 'crossover' (combinations), see Figure 4.49. When one of the stopping criteria is met the algorithm stops.

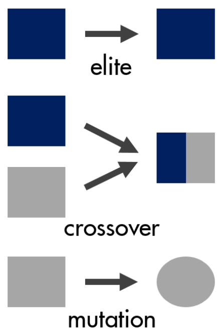

Figure 4.49: Genetic Algorithm selection method

5 Financial framework

This chapter presents all the capital and operational expenditures (CAPEX, OPEX), revenues and reviews commonly used multiples, e.g. Net Present Value (NPV), Value Investment Ratio (VIR), Internal Rate of Return (IRR), Payback Period (PBP) to indicate the station's financial performance.

5.1 CAPEX

Based on the optimization results the initial capital investment is calculated. The types of equipment considered are the CH2P unit, hydrogen storage, compressor, precooler, dispenser, battery and chargers. All equipment prices are summed to give the initial station investment cost. Costs are determined by fitting price curves to equipment quotes. Afterwards several additional cost factors are applied to arrange for indirect expenses as well. These may include costs for design & engineering, construction and contingency.

In Table 5.1 we find the equipment cost, where the capital cost is found by multiplying the unit cost by the desired quantity or size. It must be noted that for the storage type the price depends on the maximum design pressure of the unit. High pressure storage is more expensive than low pressure storage, because of the different wall materials used.

Spare parts, for example a spare compressor, are not included in the prices. Also not included are some electrical units, such as transfomers, inverters etc. Only the fast-charger is accounted for.

Also not included is the fuel quality metering. Although costs of fuel quality certification are currently excessive [27], these are expected to drop.

Table 5.1: Equipment cost

Equipment	Quantity	Capital cost ($)
CH2P system	1	XXX
Compressor	51 kW	XXX
Storage tank H_2	L/M/H	XXX
Precooling	2	XXX
Dispenser	2	XXX
Battery	134 kWh	XXX
Charger	5	XXX
Total CAPEX		XXX

Table 5.2: Indirect cost percentage for station equipment as percentage of initial investment

Item	Percentage
Site preparation	0%
Design & Engineering	10%
Construction	25%
Contingency	25%
Total factor	60%

5.2 OPEX

Operational costs for the station consist of raw materials, utilities and maintenance costs.

The natural gas price is currently 0.46 \$/kg. These costs need to be divided among the hydrogen and power products. This is done proportionally compared to the energy content of the products. For example, if in mode 1 the efficiency is 80 % and the Lower Heating Value (LHV) of the produced hydrogen is 75 % of the LHV_{80}% of natural gas, then 75 % of 0.46 \$ is accounted to the hydrogen cost and 25% to power. Maintenance prices are assumed to be yearly fixed to 3 % of the station CAPEX minus the stack costs. Power prices consist of a fixed and variable part fluctuating per season and day time. Figure 5.1 shows the variable electricity price including generation and distribution costs for commercial customers up to 500 kW connections. The average fixed cost is \$19.85 per kW per year. It is assumed that when the station provides electricity back to the grid, only the generation part of the variable costs is earned back. Distribution costs remain, no matter the direction of the power flow. This means that for each unit of electrical energy delivered to the grid 67 % of the price is earned back.

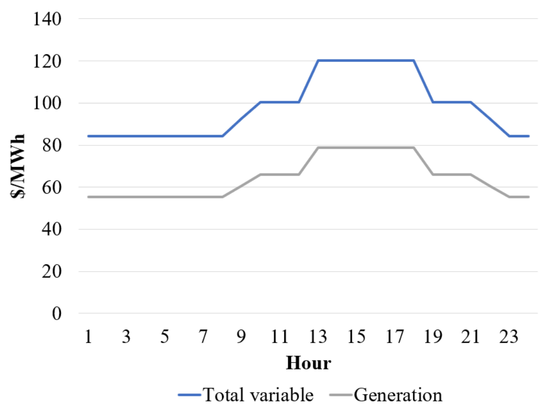

Figure 5.1: Average variable power price and generation part [53]

Table 5.3: Other OPEX

Item	\$/unit	Unit
Natural Gas	0.46	kg
Maintenance	3	%-CAPEX/yr
Rent	2000	month

5.3 Revenues and metrics

Soltani-Sobh et al. [54] demonstrated the factors on which American people base their type of vehicle decision, concluding that among incentives, urban roads and electricity prices, the last is most influential. Therefore, a sensitivity is used on the electric charging price. All the product prices are listed in Table 5.4.

Table 5.4: Product prices

Product	Price	Unit
Hydrogen	10	\$/kWh
Fast-charging	0.60	\$/kWh
Retail power	0.098	\$/kWh
Grid	Variable	\$/kWh

Table 5.5: Financial parameters

Item	Level
WACC	8%
Tax (U.S.)	21%
Inflation	2%
Lifetime HRS	10 years
Operational days	365

Each year's cash flow is simply the expected revenues minus the OPEX. In some years there are additional CAPEX when the CH2P stacks need to be replaced. The cash flow from each year (FCF) is adjusted by subtracting the depreciation of the equipment and correcting for inflation:

$$FCF_{real} = \frac{CF_{nom}}{(1 + infl)^t} \tag{5.1}$$

The Net Present Value (NPV) is the difference between the present value (PV) of all cash in- and outflows during the station lifetime. It measures the profitability of the project. In Equation 5.2 'i', is the Weighted Average Cost of Capital (WACC) by which the cash flow (CF) is discounted from year 't' from now:

$$NPV = \sum_{t=0}^{T} \frac{CF}{(1+i)^t} \tag{5.2}$$

The Value Investment Ratio (VIR) is defined as the ratio of NPV to initial capital investment:

$$VIR = \frac{NPV}{CAPEX} \tag{5.3}$$

The Internal Rate of Return is a discount rate at which the NPV becomes zero, and is found by setting the NPV to zero and solving for the discount rate 'r':

$$IRR = NPV = \sum_{t=1}^{T} \frac{CF}{(1+r)^t} - C_0 = 0 \tag{5.4}$$

Finally, the payback period is calculated as the number of years it takes to earn back the initial investment without discounting the cash flows.

6 Results and discussion

In this chapter the results are discussed. In Section 6.1 the optimization results are shown and various sensitivities are applied to some station parameters. Section 6.2 zooms into the optimal base configuration and explains how the system is behaving.

6.1 Optimization

The selected optimization metric is the Net Present Value. Furthermore, the CSI was put on 90 %. Below this threshold a penalty was applied to the NPV to make sure that most customers leave the station satisfied.

The Genetic Algorithm optimizes the station components, listed in Table 6.1, and gives the results described in this chapter. A simulation day starts at midnight and runs for 24 hours. The storages start at 100 % of their capacity, therefore production during the night will be low (incentive for production is empty storages). Then at the end of the simulation all the storages are brought back to their initial levels in order to compare the different simulations on a fair basis. Otherwise the station would start the simulation of a specific storage configuration at 100 % and finalize at a lower value, e.g. 25 %. Another configuration could give a higher value at the end of the day, e.g. 75%. Then taking these two configurations would be comparing apples and oranges as the second scenario has already much fuller storages and has most likely seen higher energy consumption to reach this state. The most important parameters for this optimization are listed in Table 6.2:

Table 6.1: Optimization variables

Item	Unit
Low pressure storage	m^3
Medium pressure storage	m^3
High pressure storage 1-3	m^3
Compressor mass flow 2	kg/s
Compressor mass flow 3	kg/s
Battery capacity	kWh
Chargers	#

Table 6.2: Simulation parameters

Item	Quantity	Unit
Station size	400	kg
CH2P transient	40	min
BEV	150	cars
FCEV	60	cars
Dispensers	2	#
Power retail	30	kW
Grid capacity	75	kW

Figure 6.1a shows the optimization results for the Net Present Value. To increase the readability of the plot, the values are changed from chronological to increasing order (Figure 6.1b). Next, the penalty for unsatisfied customers is taken out in Figure 6.2, where the values in the upper left corner then correspond to unsatisfied customers. The same approach is used for other optimization plots. The Net Present Value for the Hydrogen Refuelling Station is XXX m$ for the base case scenario. The resulting CAPEX and OPEX are shown in Figures 6.3a and 6.3b, where it can be seen that mainly the CAPEX is optimized.

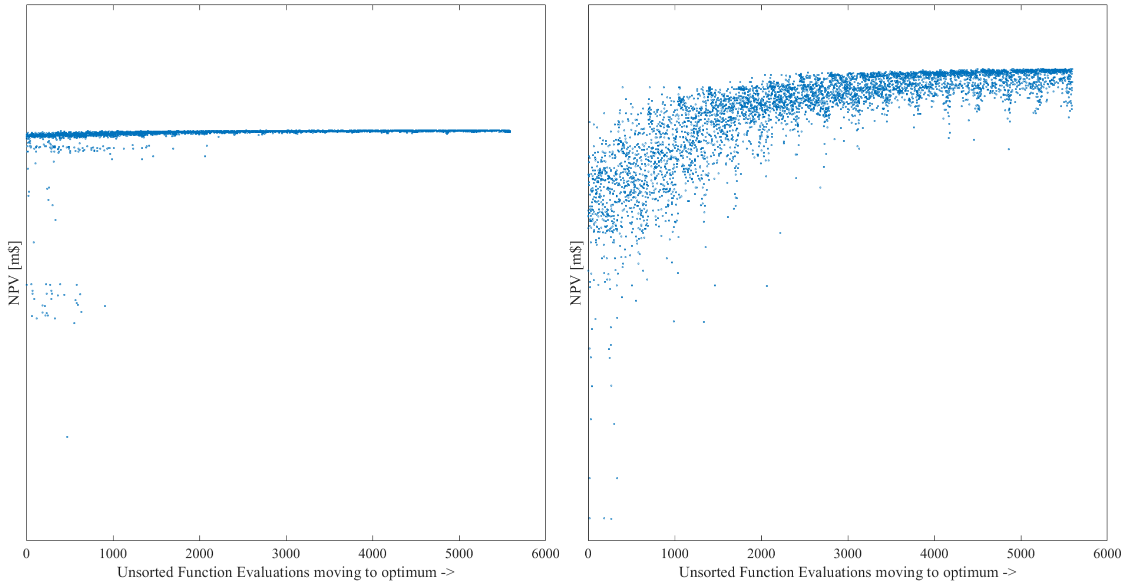

(a) With CSI penalty **(b) Without CSI penalty**

Figure 6.1: Optimization of Net Present Value (unsorted)

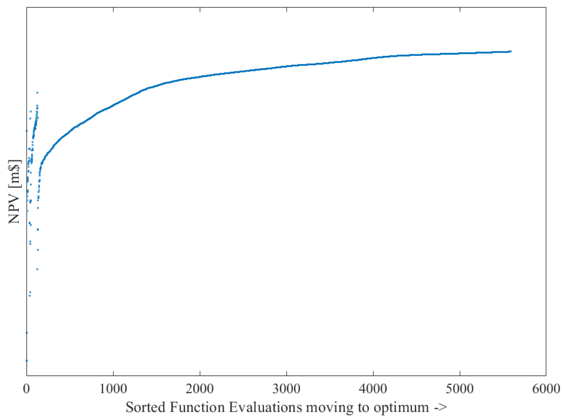

Figure 6.2: Optimization of Net Present Value (sorted, no penalty)

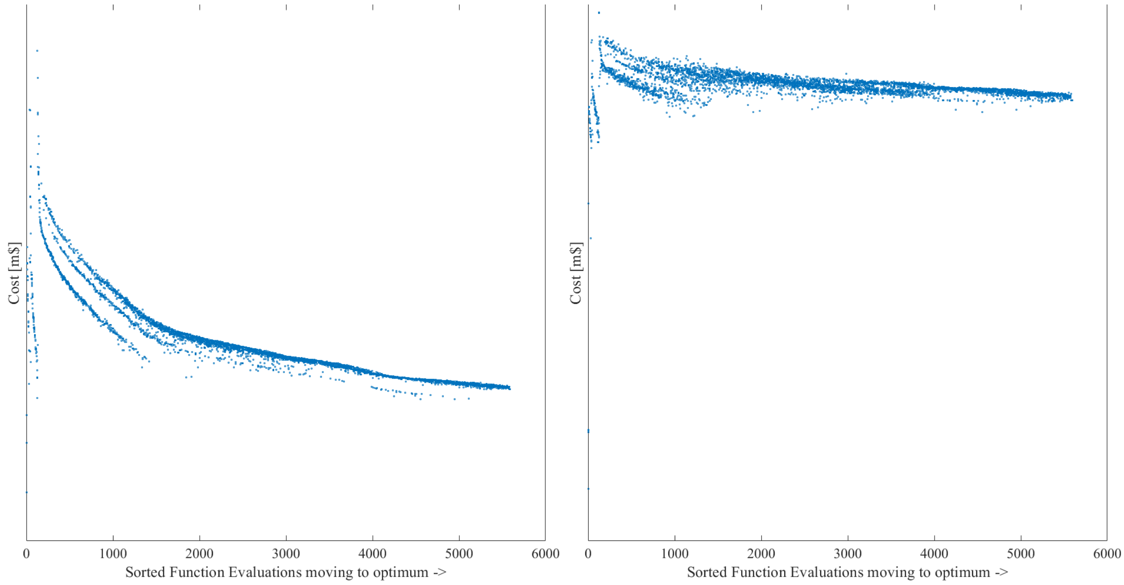

(a) CAPEX **(b) OPEX**

Figure 6.3: Optimization results

The results show that for these specific station parameters (Table 6.2) no low and medium pressure storage (Figures 6.4a, 6.4b) and therefore no second and third compressor are selected by the optimizer (Figures 6.7a, 6.7b). The compressors were optimized by setting their average mass flow rate and the corresponding figures and table show the resulting maximum power. Figure 6.6b indicates that for lower production mass flow a smaller compressor is needed, but that in the preferred setup a 51 kW is needed to match the CH2P production. Then the results also show, that for this system it is more beneficial to refuel straight from the HPS instead of adding a Medium Pressure Storage (MPS) to the station, which would be more energy efficient as concluded in Section 4.3.4. The other variables converge to the values listed in Table 6.3 as shown in Figures 6.5a, 6.5b, 6.6a, 6.8a, 6.8b. The ideal number of chargers is five, but four and six chargers score high NPVs as well.

Table 6.3: Simulation results

Item	Level	Unit
Initial State-of-Charge	100	%
Low pressure storage	0	m^3
Medium pressure storage	0	m^3
High pressure storage	0.48 / 0.90 / 1.36	m^3
Compressor power 1	51	kW
Compressor power 2	0	kW
Compressor power 3	0	kW
Battery capacity	134	kW
Chargers	5	#

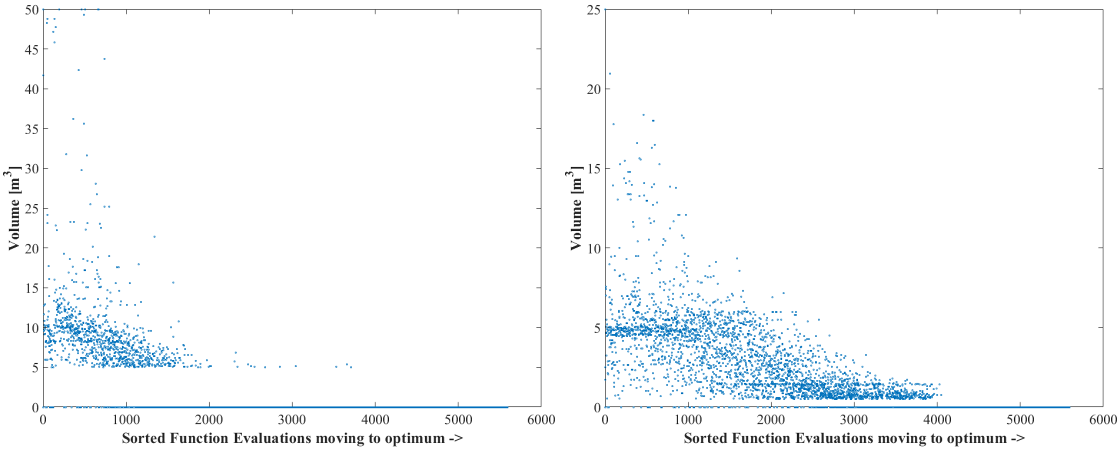

(a) Low Pressure Storage (b) Medium Pressure Storage

Figure 6.4: Optimization results

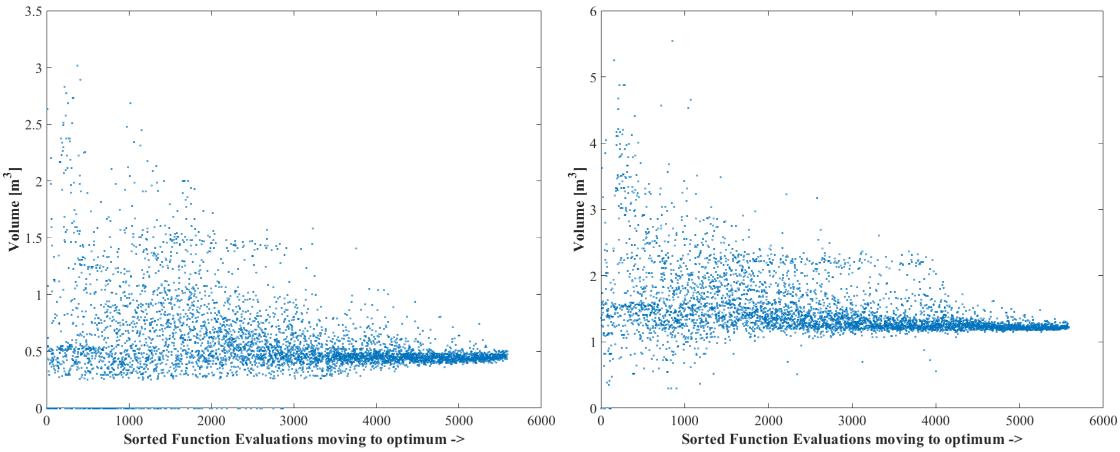

(a) High Pressure Storage 1 (b) High Pressure Storage 2

Figure 6.5: Optimization results

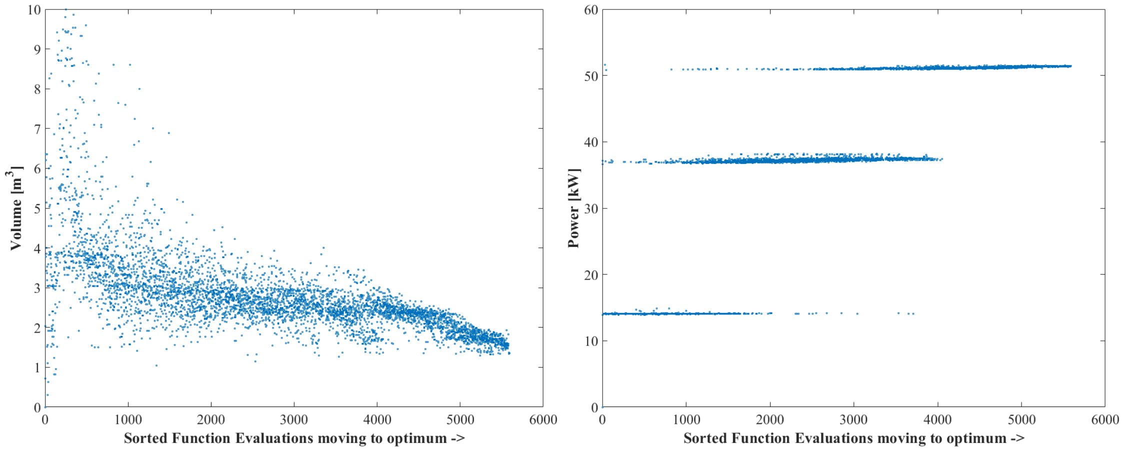

(a) High Pressure Storage 3 **(b) Compressor size 1**

Figure 6.6: Optimization results

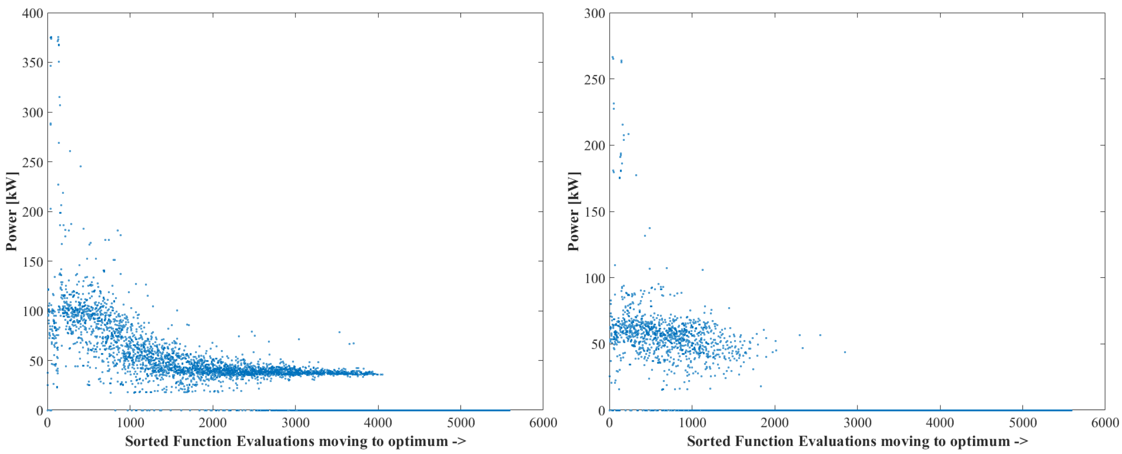

(a) Compressor size 2 **(b) Compressor size 3**

Figure 6.7: Optimization results

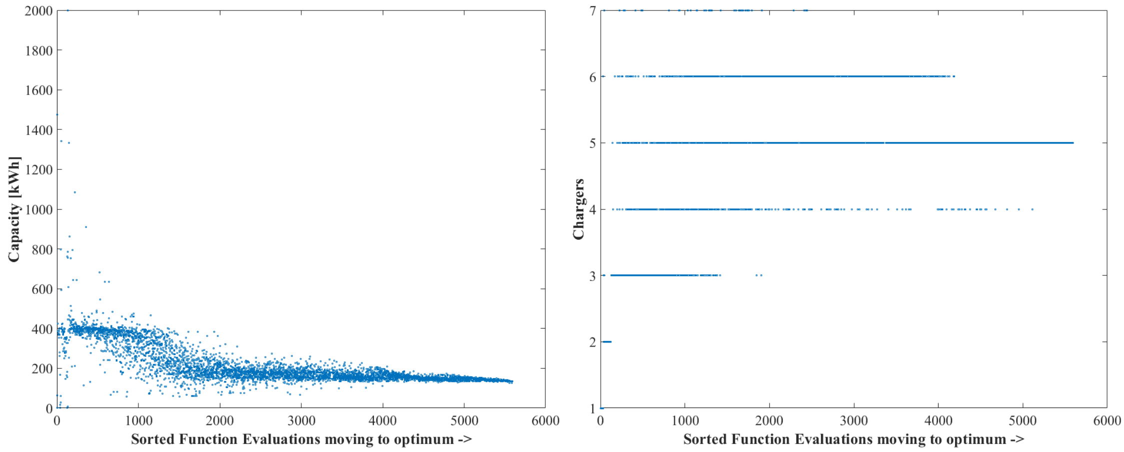

(a) Battery storage **(b) Electric chargers**

Figure 6.8: Optimization results

Some figures have been left out due to confidentiality
Now the results for different station parameters will be discussed. First, the optimal station differs for various utilization rates. Figure **??** and **??** display the effect on the NPV and component sizes. For higher number of vehicles the station becomes more profitable and the required storage facilities grow in size as well. The number of FCEVs is however more influential than the number of BEVs. Moreover, the number of chargers and the battery size grow as well, according to Figure **??**. However, the battery size is rather constant for larger utilization rates, indicating that not the capacity, but the delivered power is of greater importance. Second, a sensitivity on the retail power demand (Figure **??**) shows an interesting effect. For larger retail demand the battery capacity increases, but the NPV decreases. This is caused due to a negative margin on retail power. Third, longer CH2P transient behavior increases the CAPEX of the station as more storage facilities are needed. A MPS is added to the system to cope with the longer switching time between operating modes. Finally, testing with 500 bar MPS has not improved the NPV, the optimal station remains without MPS.

The cost per unit differs per utilization scenario. As expected the price drops for higher utilization rates, at 50 % hydrogen utilization the cost is XXX $/kg and at 100 % it is XXX $/kg. For power the differences are smaller, but not following the same logic as before. The OPEX remain fairly constant, but the CAPEX is higher for the second scenario in Figure **??** due to a larger battery. The battery size is of the same order as in scenario one and four, meaning the battery has more a power - instead of a capacity - function. Combined with a lower total power production this gives a higher cost per unit. A battery with a higher power-to-energy ratio (or C-rate) could lower the cost in this case.

6.2 Optimal CH2P station

The full day simulation of the optimized HRS configuration gives the following results. The most important parameters for this simulation are found in Table 6.2. The results show that the HRS is capable of providing 60 hydrogen and 150 electric cars with fuel and power at an average SoC of more than 97.7 % by using two dispensers and five electric chargers. Simultaneously the power demand for the retail station (max. 30 kW) is covered and some excess power has been sold to the grid. Table 6.4 shows the availability of dispensers and chargers and the resulting average State-of-Charge for the vehicles. It is clear that setting a minimum Customer Satisfaction Index has no effect on the optimization, as the results are well above the minimum threshold.

Table 6.4: Optimal station: availability and average State-of-Charge

Item	Availability %	Average final SoC %
Hydrogen	98.3	97.7
Electric	93.3	100

Table 6.5: Optimal station: input and output quantities

Item	Quantity	Unit
Natural gas	XXX	kg/d
Hydrogen	287	kg/d
CH2P gross	6280	kWh/d
CH2P net	4739	kWh/d
Compression, cooling	924	kWh/d
BEVs	2607	kWh/d
Retail	612	kWh/d
Grid	76	kWh/d
Balance	121	kWh/d

The CH2P system remains turned off until 5 a.m., no hydrogen vehicles arrive and so the storages stay full. The CH2P unit switches 35 times between modes during the day (Figure 6.9) and the most frequently operated modes are mode two and three. Mode two corresponds to the highest hydrogen production mode and mode three to almost identical levels of hydrogen production, but with roughly double electricity production. The production levels are shown in Figures 6.10a and 6.10b. During the day the hydrogen production is relatively stable around 17.5 kg/h. The production of power switches, however, often between 236 kW and 498 kW gross power. This happens when the battery SoC passes a certain threshold after which the mode is changed. If switching is not recommended the procedure could be redesigned to let the mode run up to higher battery energy levels.

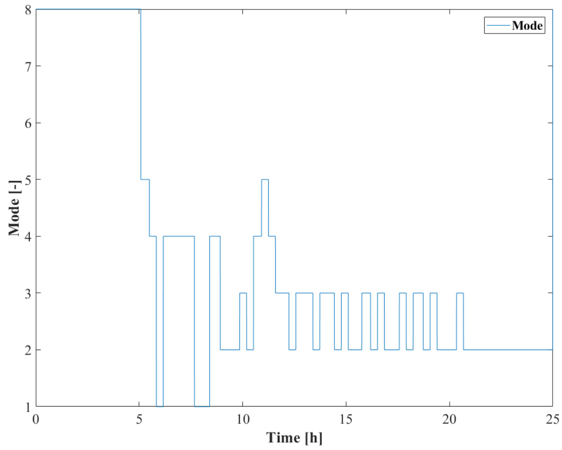

Figure 6.9: CH2P modes during full day operation

With corresponding mass and power production:

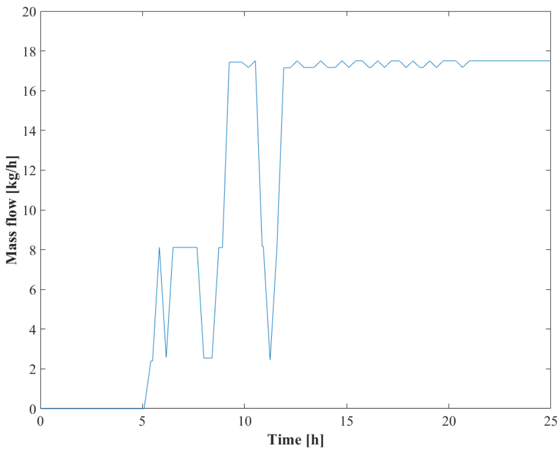

(a) Mass production

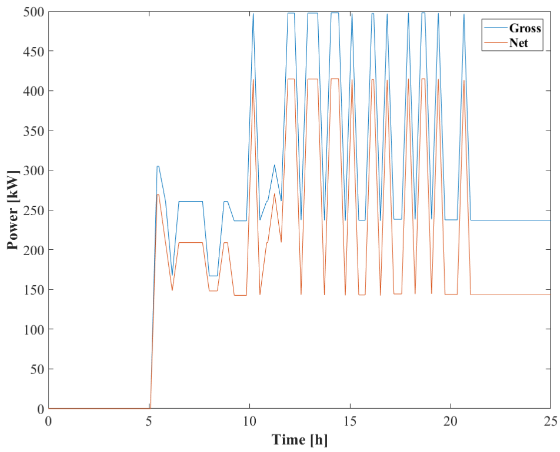

(b) Power production

Figure 6.10: CH2P production

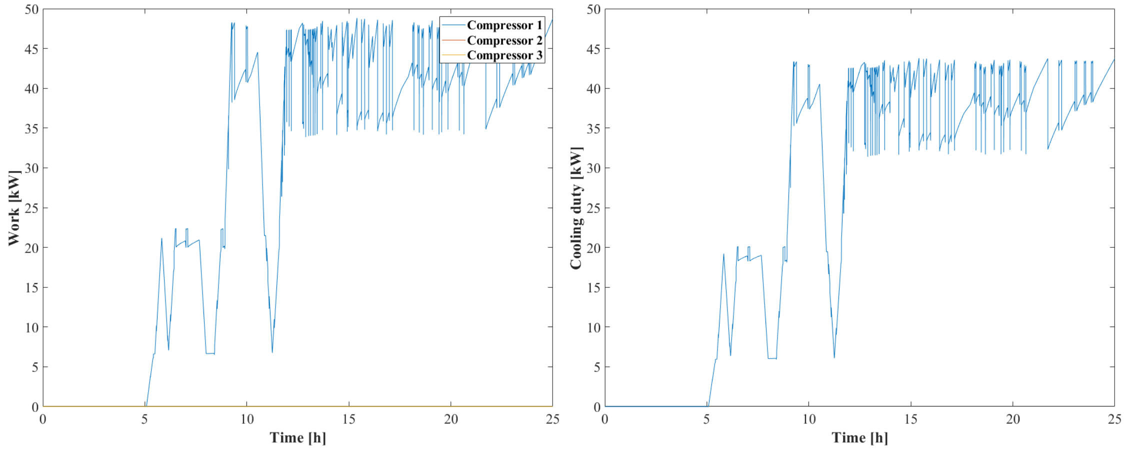

(a) **Power of compressor 1** (b) **Intercooling duty of compressor 1: heat removal**

Figure 6.11: Total compression work and intercooling

The compressor completely follows the CH2P production (Figure 6.11a), and starts at 5 a.m. and remains running the entire day. The compression power per unit hydrogen is calculated from Table 6.5 and equals 3.22 kWh/kg including inter- and precooling.

Figure 6.12 shows the hydrogen mass flow to the vehicles. The few peaks just beneath 0.1 kg/s arise when two dispensers are occupied at the same time.

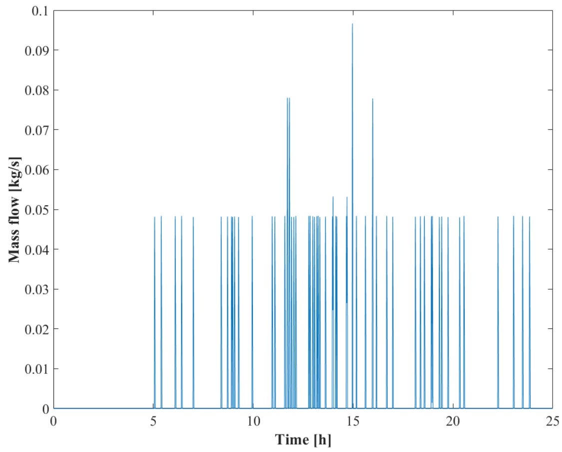

Figure 6.12: The amount of hydrogen dispensed to Fuel Cell Electric Vehicles

The hydrogen storages contain 148 kg of mass, which brings the ratio of the storage capacity to daily demand to 52 %, or 22 % higher than suggested by the Department of Energy [12]. Looking at the amount of usable mass in the storages (by recognizing a certain minimum pressure in the tank) the ratio becomes significantly lower, about 29 %. For both 300 and 500 bar MPS the optimized size is 0 m^3. Even though the energy efficiency in cascade configuration eight (three high pressure storages of 950 bar and one medium pressure storage of 500 bar) is the highest and saves up to 12 % compared to having one high pressure storage vessel of 950 bar. This indicates that the trade-off between energy efficiency and CAPEX was in favor of the latter. It is clearly noticeable that HPS 1 is used the least, the total dispensed mass from this storage is 61 kg. Furthermore, about 129 kg is dispensed from HPS 2 and from HPS 3 about 97 kg. HPS 3 dispenses less mass than HPS 2, because the compressor does not get the chance to fill HPS 2 to its maximum capacity and therefore HPS 3 remains empty after a certain point. See the mass flow, pressure, temperature and SoC profiles in Figures 6.13a, 6.13b, 6.14, 6.15, 6.16a, 6.17a, 6.17b, 6.18. The temperature in the storages remains nicely within their operating limits and storages two and three are both fully used during the day. The precooling power requirement is shown in Figure 6.19b, where the power to keep the cooler at -40°C is 4.5 kW. Figure 6.19b has one peak at 15 hour, when two dispensers are occupied simultaneously and started refuelling (and cooling) at the same time.

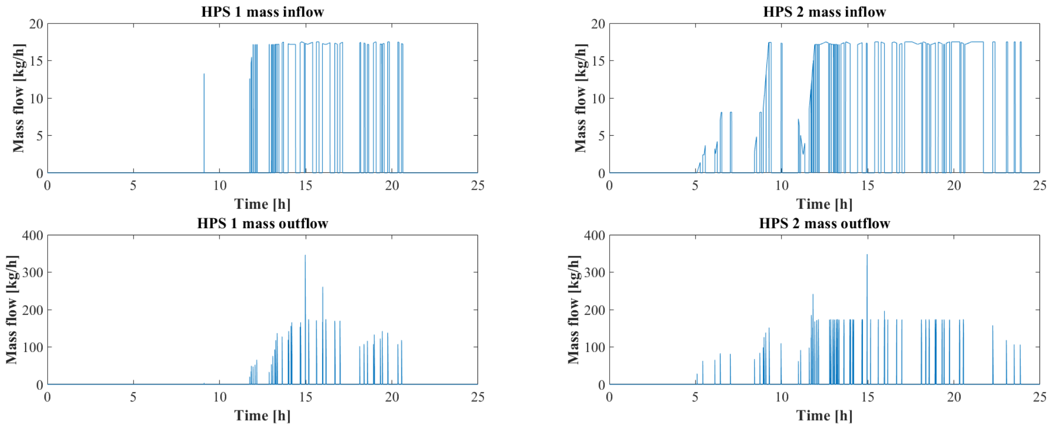

(a) High Pressure Storage 1 **(b) High Pressure Storage 2**

Figure 6.13: Mass in- and outflow of storages

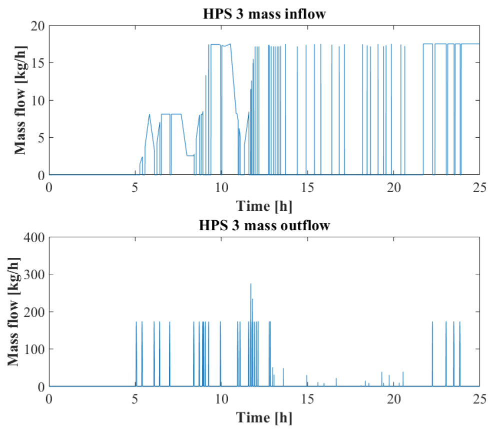

Figure 6.14: Mass in- and outflow of High Pressure Storage 3

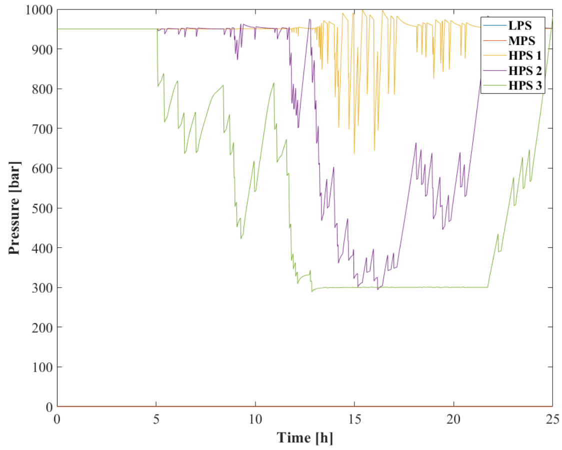

Figure 6.15: Pressure levels storages

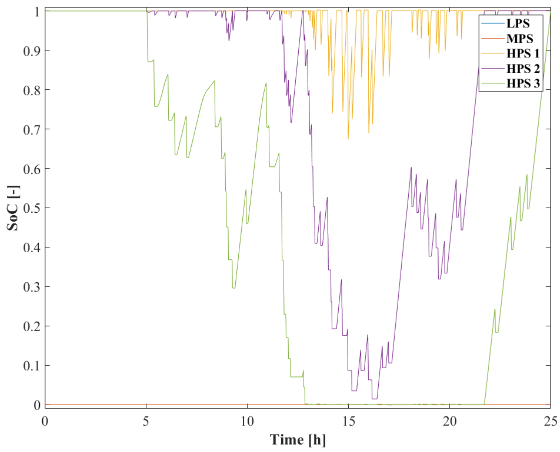

(a) State-of-Charge storages

Figure 6.16: Pressure and State-of-Charge of storages

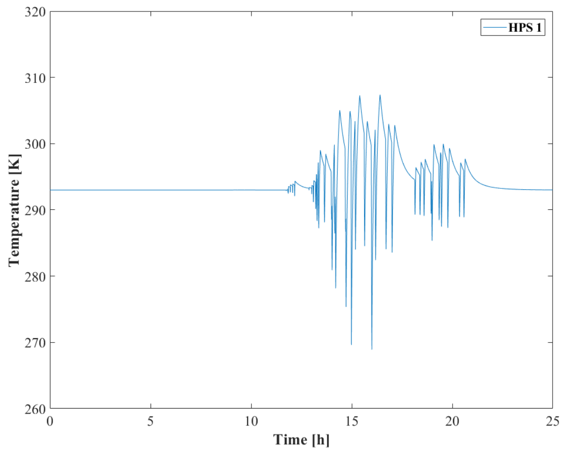

(a) High Pressure Storage 1

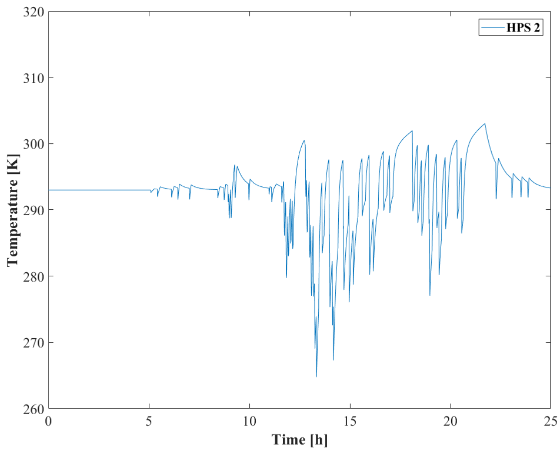

(b) High Pressure Storage 2

Figure 6.17: Temperature profile storages

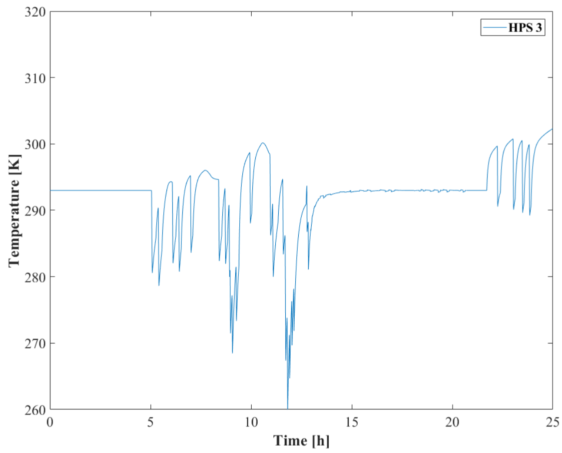

Figure 6.18: Temperature profile High Pressure Storage 3

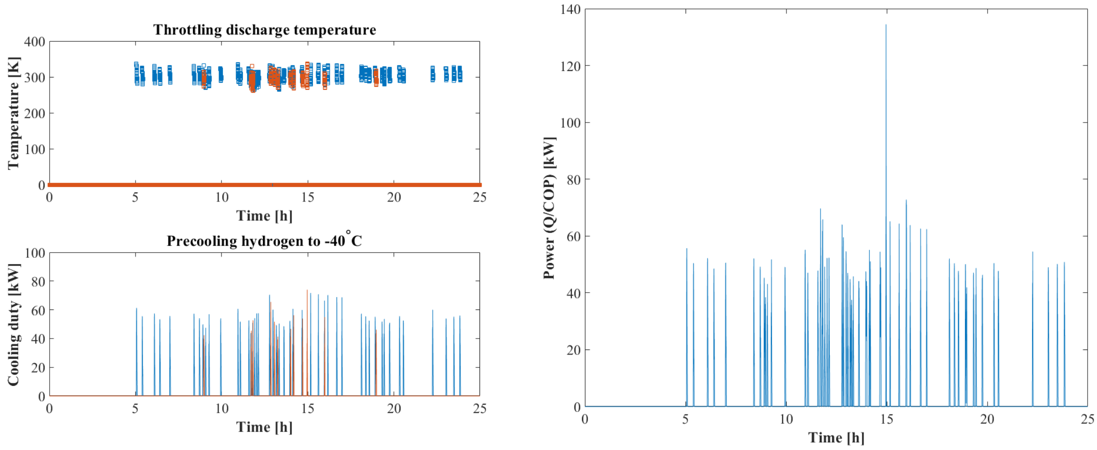

(a) **Heat removal** (b) **Power consumption cooler**

Figure 6.19: Hydrogen precooling before dispensing

Figure 6.20a shows the power drawn by the electric chargers. The maximum value is 375 kW, which equals five fast-chargers of an effective charging rate of 75 kW. The peak is witnessed around noon and afternoon rush hour, which corresponds to the probability density function in Section 4.1. Then Figure 6.20b shows the battery (dis-)charging. The grid connection jumps in when the station needs more power, as is the case during the night when the CH2P production is off because the hydrogen storage is full. Between 5 and 10 a.m. an excess of power exists and during the middle of the day power is mostly being imported due to many BEVs.

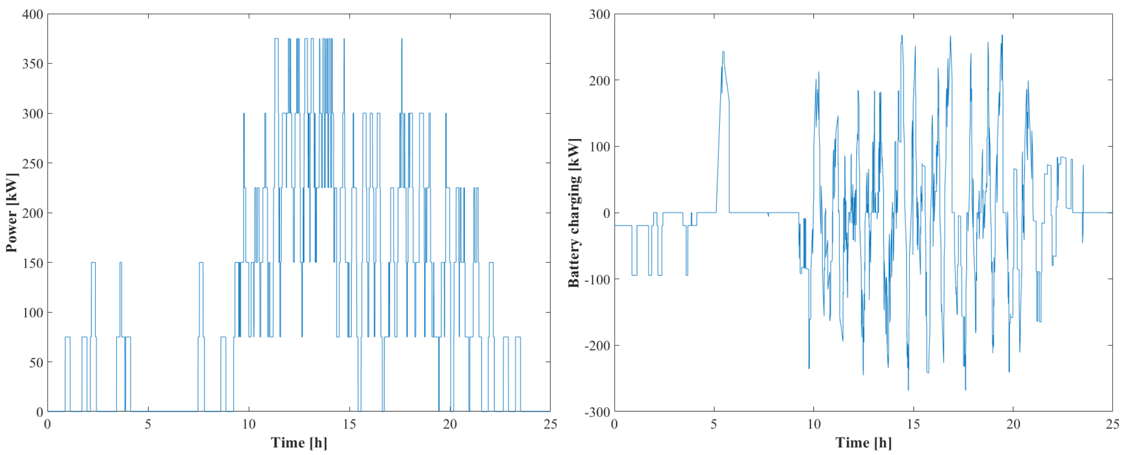

(a) **Electric Charging** (b) **Battery storage**

Figure 6.20: Power charged by Battery Electric Vehicles and (dis-)charging of battery storage

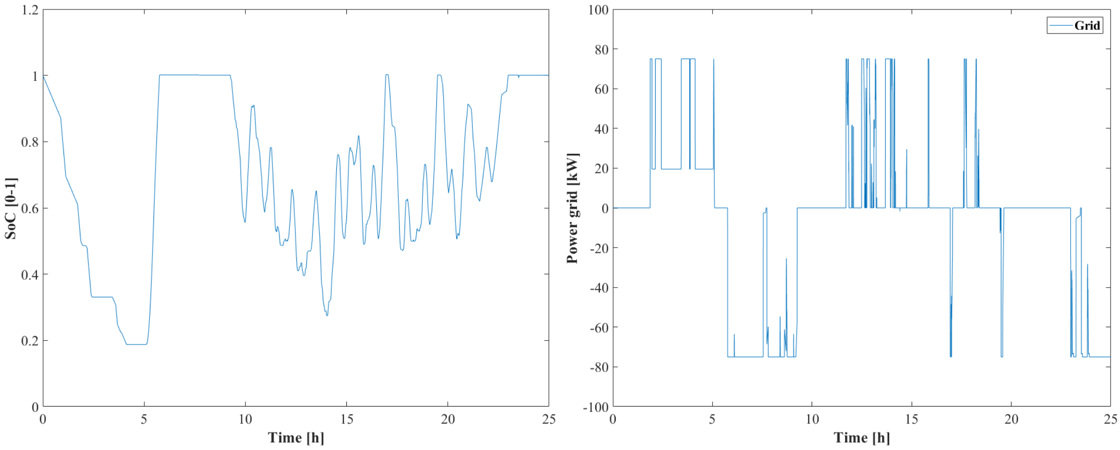

(a) Battery storage (b) Grid connection

Figure 6.21: State-of-Charge battery storage and grid power consumption

An overview of the costs and all sensitivities is excluded from this non-confidential version of the report.

7 Conclusions and recommendations

7.1 Conclusions

The final model of a Hydrogen Refuelling Station gives some interesting insights about the fuel station. Most importantly it does show that the Cogeneration of Hydrogen, Heat and Power as a decentralized production method is profitable. The station becomes 55 % more profitable for higher utilization rates. The hydrogen and power unit cost are XXX $/kg and XXX $/kWh, respectively. Moreover, the CAPEX for compression, storing and dispensing is XXX $/kg. The hydrogen price has the largest effect on the NPV, whereas the natural gas price has the largest effect on the hydrogen and power cost. Other important costs are the CH2P unit and fast-chargers.

The HRS has proven to meet the first three use cases as stated in Section 3, where further analysis is needed for the excess heat integration. Electricity demands for the retail station could successfully be delivered up to high power levels. The CH2P system has shown to be able to provide fast-charging to BEVs by adding a battery and without the need to increase the standard grid capacity of 75 kW. The optimized HRS configuration for 60 FCEVs and 150 BEVs consists of three high pressure storages in cascade, a four-stage compressor plus intercooling, two dispensers and precoolers, five 150 kW fast-chargers and a 134 kWh battery. The corresponding availability of refuelling or charging spots is 98.3 % and 93.3 %, where the average final SoC of the vehicles is for dispensing 97.7 % and charging 100 %. For larger CH2P transients the station equipment becomes larger.

About the optimization can be said that a minimum required Customer Satisfaction Index has little effect on the optimization results. It is most beneficial to refuel vehicles to their maximum capacity in order to gain the highest revenues. The accuracy of the Genetic Algorithm is highly dependent on the number of model evaluations, at least 30 generations with population size 300 are recommended. The simulation time for testing one particular station configuration is rather quick (less than one minute), but unfortunately the model is slow in optimization when 30*300 iterations are required. Running the Genetic Algorithm in parallel mode on 8 cores speeds up the process, but still 5-10 hours are required to gain results.

All hydrogen equipment remained within reasonable operating conditions. The most energy efficient configuration consists of one 500 bar MPS and three HPSs in cascade, saving up to 12 % on compression, cooling and dispensing compared to having one storage vessel. The total storage is also greatly reduced. These positive effects of cascade filling on the energy consumption were more subtle than found in literature.

The electric system is currently not sufficient for coping with sudden power fluctuations. For larger CH2P production transients the mode selection thresholds must be re-evaluated. Power production by CH2P is more expensive than grid power and opportunities for grid ancillary services are still unclear.

7.2 Recommendations

The main bottleneck in optimizing the station has been the speed of the algorithm. Therefore, the usability could be greatly improved by enhancing the speed of the Genetic

Algorithm or by using a different optimization method. Besides this practical remark, the results could be boosted from different perspectives.

First, the input and parameters of the system can be improved. In the current simulation weekly and yearly demand fluctuations are not considered and might impact the preferred operation of the station. The CH2P operating modes are also an input to the system. These modes do not cover the full spectrum of the operating envelope. More flexibility would be introduced if the system could cover a wider range of operating modes, for example 100 % hydrogen and 0 % power and vice versa. Also, the system often switches between two modes, there might be a combination possible of both.

Second, revising assumptions, adding more detail to the design and simulating different settings gives better and more realistic insights of the system. Further integration of rest heat improves, for example, the station's efficiency as you can always heat water for the car-wash or retail station. Then, modelling also the car vessel and battery system would give a more realistic interface between the station and vehicles. Next, the electric system consists of a very basic design and electric losses are currently not considered in the model and should be further scrutinized, for example, by adding the battery round trip efficiency, transformer and inverter losses. Currently the system is not capable of handling sudden power spikes, additional equipment such as a supercapacitor should be researched. Besides electric losses, finding the pressure losses of the compressor, intercooler and dispenser improves the model as well. Then, the heat transfer coefficients of storage vessels are experimentally determined only for small storage sizes. The well-stirred assumption might be invalid for larger vessels. Another heat transfer related recommendation would be to understand how the precooler behaves during multiple back-to-back fillings, is the handling time between actual back-to-back mass flow enough to cool the HEX block back to -40°C? More details are also required in the economics section. The financial framework consists only of the main capital and operational costs, and revenues, and must be further investigated. Several angles are possible here: using more recent cost curves, understanding the effect of carbon pricing, add pipes and valves, electrical components, and examine additional cost factors when building stations such as civil works.

Third, the results have to resonate in a wider perspective. The CH2P station must be compared to conventional hydrogen or electricity production facilities (or grid expansion options), and the benefits of modular and expandable stations with a high degree of standardization should be reviewed. Compatibility issues of placing a CH2P system and CDS components to an existing station have not yet been explored.

References

[1] Vision on the charging infrastructure for electric transport. Dutch Ministry of Economic Affairs, 2017.

[2] S. Kodukula, F. Rudolph, U. Jansen, and E. Amon. Living. Moving. Breathing. Surface Vehicle Standard, Wuppertal: Wuppertal Institute, 2018.

[3] Hydrogen's role in the future of transport. Shell, [Online]. Available: https://www.shell.com/energy-and-innovation/the-energy-future/future-transport/hydrogen.html, [Accessed: June 2018].

[4] K. Reddi, A. Elgowainy, N. Rustagi, and E. Gupta. Impact of hydrogen refueling configurations and market parameters on the refueling cost of hydrogen. *International Journal of Hydrogen Energy*, 42:21855–21865, 2017.

[5] Summary of H2ME projects achievements and emerging conclusions. Hydrogen Mobility Europe, [Online]. Available: https://h2me.eu/about/hydrogen-refuelling-infrastructure/, [Accessed: May 2018].

[6] P.J. Bouwman, J. Konink, D. Semerel, L. Raymakers, M. Koeman, W. Dalhuijsen, E. Milacic, and M. Mulder. Electrochemical hydrogen compression. *Electrochemical Society Transactions*, 64:1009–1018, 2014.

[7] B. Heid, M. Linder, A. Orthofer, and M. Wilthaner. Hydrogen: The next wave for electric vehicles? McKinsey - Automotive and Assembly, 2017.

[8] R. Hendricks, C. Ildiko, and A. Baron. Joule-Thomson inversion curves and related coefficients for several simple fluids. NASA, 1972.

[9] A European Strategy for low-emission mobility. European Union, [Online]. Available: https://ec.europa.eu/clima/policies/transport-en, [Accessed: May 2018].

[10] B. Van Bree, G.P.J. Verbong, and G.J. Kramer. A multi-level perspective on the introduction of hydrogen and battery-electric vehicles. *Technological Forecasting and Social Change*, 77(4):529–540, 2010.

[11] B. Elrick. The California Fuel Cell Revolution. California Fuel Cell Partnership, 2018.

[12] Hydrogen Delivery Infrastructure Options Analysis. DOE Award DE-FG36-05GO15032, Department Of Energy - Fuel Cell Technologies Office, 2008.

[13] Personenauto's. Centraal Bureau voor de Statistiek, [Online]. Available: https://www.cbs.nl/nl-nl/maatschappij/verkeer-en-vervoer/transport-en-mobiliteit/infra-vervoermiddelen/vervoermiddelen/categorie-vervoermiddelen/personenauto-s, [Accessed: May 2018].

[14] Hydrogen, scaling up. A sustainable pathway for the global energy transition. Hydrogen Council, 2017.

[15] Fueling Protocols for Light Duty Gaseous Hydrogen Surface Vehicles. Surface Vehicle Standard, SAE International, 2016.

[16] Commercial Buildings Energy Consumption. U.S. Energy Information Administration, 2018.

[17] T. Gnann, S. Funke, N. Jakobsson, P. Plø̈tz, F. Sprei, and A. Bennehag. Fast charging infrastructure for electric vehicles: Today's situation and future needs. *Transportation Research Part D: Transport and Environment*, 62:314–329, 2018.

[18] J. Yang, T. Kim, J. Park, T. Lim, H. Jung, and D. Chun. Development of a stand-alone steam methane reformer for on-site hydrogen production. *International Journal of Hydrogen Energy*, 41:8176–8183, 2016.

[19] A.L. Dicks. Hydrogen generation from natural gas for the fuel cell systems of tomorrow. *Journal of Power Sources*, 61:113–124, 1996.

[20] P. Breeze. *Fuel Cells*. Elsevier, 2017.

[21] Fuel cells - Fuel cell types. U.S. Department of Energy - Energy Efficiency and Renewable Energy, 2006.

[22] E. Rothuizen, W. Mérida, M. Rokni, and M. Wistoft-Ibsen. Optimization of hydrogen vehicle refueling via dynamic simulation. *International Journal of Hydrogen Energy*, 41:4221–4231, 2013.

[23] E. Rothuizen and M. Rokni. Optimization of the overall energy consumption in cascade fueling stations for hydrogen vehicles. *International Journal of Hydrogen Energy*, 39:82–592, 2014.

[24] N. Omdahl. Modelling of a hydrogen refueling station. Norwegian University of Science and Technology, Trondheim, 2014.

[25] K. Reddi, A. Elgowainy, and E. Sutherland. Hydrogen refueling station compression and storage optimization with tube-trailer deliveries. *International Journal of Hydrogen Energy*, 39:19169–19181, 2014.

[26] M. Suermanna, T. Kiupela, T.J. Schmidta, and F.N. Büchia. Electrochemical Hydrogen Compression: Efficient Pressurization Concept Derived from an Energetic Evaluation. *Journal of The Electrochemical Society*, 164:1187–1195, 2017.

[27] G. Parks, R. Boyd, J. Cornish, and R. Remick. Hydrogen Station Compression, Storage, and Dispensing Technical Status and Costs. U.S. Department of Energy Hydrogen and Fuel Cells Program, NREL, 2014.

[28] M. Gardiner. Energy requirements for hydrogen gas compression and liquefaction as related to vehicle storage needs. U.S. Department of Energy Hydrogen and Fuel Cells Program, 2009.

[29] Development of calculation formulas for cylinder wall thickness. European Cylinder Makers Association, 2018.

[30] E. Talpacci, M. Reub, T. Grube, P. Cilibrizzi, R. Gunnella, M. Robinius, and D. Stolten. Effect of cascade storage system topology on the cooling energy consumption in fueling stations for hydrogen vehicles. *International Journal of Hydrogen Energy*, 43:6256–6265, 2018.

[31] E. Ruffio, D. Saury, and D. Petit. Thermodynamic analysis of hydrogen tank filling. effects of heat losses and filling rate optimization. *International Journal of Hydrogen Energy*, 39:12701–12714, 2014.

[32] A.F. Mills. *Basic heat and mass transfer*, volume 2. Pearson, 2014.

[33] Annual Average Wind Speeds in the Netherlands. KNMI, [Online]. Available: https://www.currentresults.com/Weather/Netherlands/wind-speed-annual.php, [Accessed: July 2018].

[34] T. Bourgeois, F. Ammouri, M. Weber, and C. Knapik. Evaluating the temperature inside a tank during a filling with highly-pressurized gas. *International Journal of Hydrogen Energy*, 40:11748–11755, 2015.

[35] M. Monde, P. Woodfield, T. Takano, and M. Kosaka. Estimation of temperature change in practical hydrogen pressure tanks being filled at high pressures of 35 and 70 mpa. *International Journal of Hydrogen Energy*, 37:5723–5734, 2011.

[36] P. Woodfield, M. Monde, T. Takano, and Y. Misutake. Measurement of averaged heat transfer coefficients in high-pressure vessel during charging with hydrogen, nitrogen or argon gas. *Journal of Thermal Science and Technology*, 2:180–191, 2007.

[37] E.W. Lemmon, I.H. Bell, M.L. Huber, and M.O. McLinden. NIST Standard Reference Database 23: Reference Fluid Thermodynamic and Transport Properties-REFPROP, Version 9.0, [Online]. Available: https://www.nist.gov/srd/refprop, [Accessed: April 2018].

[38] M. Deymi-Dashtebayaza, M. Farzaneh-Gordb, and H. Rahbari. Thermodynamic analysis of single reservoir filling process of hydrogen vehicle. *Theoretical Foundations of Chemical Engineering*, 52:465–472, 2018.

[39] M. Farzaneh-Gord, M. Deymi-Dashtebayaz, H. Rahbari, and H. Niazmand. Effects of storage types and conditions on compressed hydrogen fuelling stations performance. *International Journal of Hydrogen Energy*, 37:3500–3509, 2012.

[40] B. Simonsen. Case Study: HyNor Filling Station, Grenland. International Energy Agency, 2009, [Online]. Available: http://ieahydrogen.org/Activities/Selected-Case-Studies/Grenland-refuelling-station-(Norway).aspx, [Accessed: May 2018].

[41] J. Xiao, X. Wang, P. Bénard, and R. Chahine. Determining hydrogen pre-cooling temperature from refueling parameters. *International Journal of Hydrogen Energy*, 41:16316–16321, 2016.

[42] Hydrogen Fueling Station Precooling MCHE. Vacuum Process Engineering, [Online]. Available: http://vpei.com/wp-content/uploads/Hydrogen-Fueling-Station-Pre-Cooling-MCHEprint.pdf, [Accessed: January 2019].

[43] A. Elgowainy. Hydrogen fueling station precooling analysis. U.S. Department of Energy Hydrogen and Fuel Cells Program, Argonne National Laboratory, 2014.

[44] P. Denholm, M. O'Connell, G. Brinkman, and J. Jorgenson. Overgeneration from Solar Energy in California: A Field Guide to the Duck Chart. U.S. Department of Energy - Energy Efficiency and Renewable Energy, NREL, 2015.

[45] The 2015 year-in-review executive summary. Green Tech Media Research, 2016.

[46] C. Zhang, L. Zhang, Y. Ding, and S. Peng. Progress and prospects of next-generation redox flow batteries. *Energy Storage Materials*, 15:324–350, 2018.

[47] I. Tsiropoulos, D. Tarvydas, and N. Lebedeva. Li-ion batteries for mobility and stationary storage applications. Joint Research Centre - European Union, 2018.

[48] Verordnung über technische Mindestanforderungen an den sicheren und interoperablen Aufbau und Betrieb von öffentlich zugänglichen Ladepunkten für Elektromobile (Ladesäulenverordnung LSV). Bundesministerium für Wirtschaft und Energie, 2014.

[49] M. Nicholas and D. Hall. Lessons learned on early electric vehicle fast-charging deployments. International Council on Clean Transportation, 2018.

[50] How fast-charging works. Fastned, [Online]. Available: https://fastned.nl/en/blog/post/how-fast-charging-works, [Accessed: May 2018].

[51] D. Hall and N. Lutsey. Emerging best practices for electric vehicle charging infrastructure. International Council on Clean Transportation, 2017.

[52] T. Kuroki, N. Sakoda, K. Shinzato, M. Monde, and Y. Takata. Prediction of transient temperature of hydrogen flowing from pre-cooler of refueling station to inlet of vehicle tank. *International Journal of Hydrogen Energy*, 43:1846–1854, 2018.

[53] Time-of-Use rate plans. Pacific Gas and Electric, [Online]. Available: https://www.pge.com/en-US/small-medium-business/your-account/rates-and-rate-options/time-of-use-rates.page, [Accessed: October 2018].

[54] A. Soltani-Sobh, K. Heaslip, A. Stevanovic, R. Bosworth, and D. Radivojevic. Analysis of the electric vehicles adoption over the united states. *Transportation Research Procedia*, 22:203–212, 2017.

[55] R. Holyst and A. Poniewierski. *Thermodynamics for Chemists, Physicists and Engineers*, volume 1. Springer, Dordrecht, 2012.

[56] H Chen, J. Zheng, P. Xu, L. Li, Y. Liu, and H. Bie. Study on real-gas equations of high pressure hydrogen. *International Journal of Hydrogen Energy*, 35(7):3100–3104, 2010.

[57] M.J. Moran, H.N. Shapiro, D.D. Boettner, and M.B. Bailey. *Fundamentals of Engineering Thermodynamics*, volume 8. Wiley, 2014.

Appendix

A Equation Of State

Properties of fluids, mixtures or solids are described by equations of state (EOS) that relate state variables like pressure, volume and temperature (PVT). The ideal gas law is the limiting case of a real gas when the pressure goes to zero [55].

Hydrogen under high pressure deviates much from ideal behavior and calculations based on the ideal gas state equation cause large errors. Differences between both equations are caused by neglecting molecular volumes and intermolecular forces of the real gas [56]. Therefore, the thermodynamic fluid properties of hydrogen need to be derived from real gas equations of state.

The Universal Gas Constant, $\bar{R}$, is the limiting value for all gases in the limit of the ratio $p\bar{v}/T$ as p tends to zero at fixed temperature. The compressibility factor, denoted by Z, is the ratio

$$Z = \frac{p\bar{v}}{\bar{R}T} \; or \; Z = \frac{p\nu}{RT} \tag{A.1}$$

and tends to unity when pressure goes to zero, as can be seen in A.1:

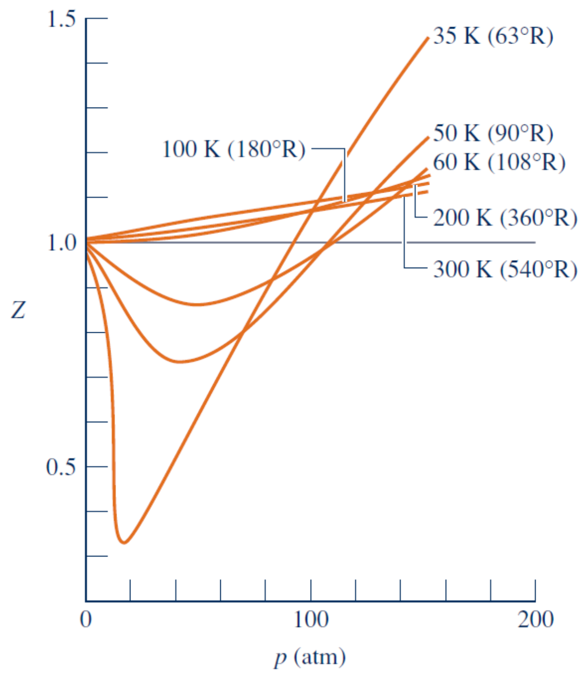

Figure A.1: Variation of the compressibility factor of hydrogen with pressure at constant temperature [57]

B SAE J2601

This protocol contains technical information and defines the hydrogen fueling standards and corresponding process limits, without compromising on safety. According to SAE, process limits include the fuel temperature, fuel flow rate, pressure ramp rate and final pressure, these are affected by for example the ambient pressure and initial storage tank pressure. The protocol gives guidelines for 35 and 70 MPa vehicles. The ratings of the different protocols are indicated by letters A, B, C and D, for a certain temperature level. Table B.1 shows the various ratings, for the A70 case a precooling temperature of -40°C is needed to avoid too high thermal stresses in the vessel material. Figure B.2 presents the operating region. The maximum allowable pressure is 125 % times the NWP, or 87.5 MPa for a A70 vehicle. Smaller tanks have a higher risk of being overheated as they are filled faster.

Table B.1: SAE J2601 precooling requirement based on vehicle's pressure and mass capacity

Type	Mass [kg]	Pressure [MPa]	Precooling [°C]
A70	1-7	70	-40
A70	7-10	70	-40
A35	1-7.5	35	-40
B70	1-7	70	-20
B70	7-10	70	-20
B35	1-7.5	35	-20
C35	1-7.5	35	0
D35	1-7.5	35	n/a

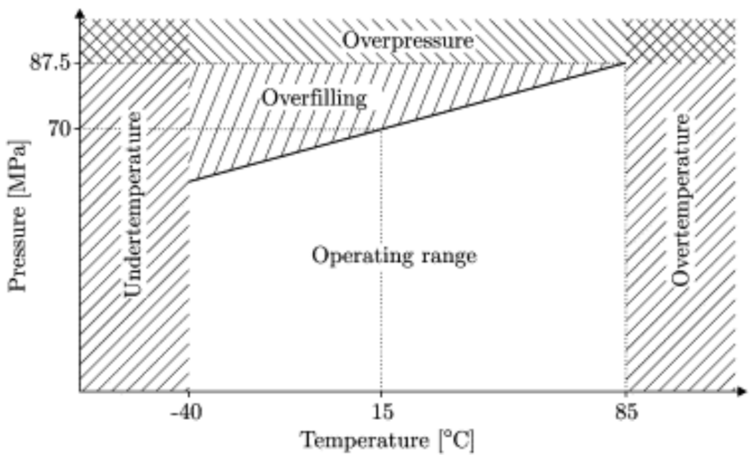

Figure B.2: Operating region as defined by SAE J2601 [24]

Using a T40 dispenser, the fueling performance target is set at 3 minutes fueling time to reach a State-of-Charge of 95-100 %. The T40 dispenser precools the hydrogen to -40°C. This is necessary because the hydrogen temperature increases due to the Joule-Thomson effect and the added compression heat.

The dispenser consists of several components to transfer fuel from the station storage to the vehicle (connector/coupling, nozzle, receptacle, dispenser hose, hose break-away). Fueling may happen with a valid data connection from the vehicle to the dispenser, but can also work without communication interface. The protocol for fueling depends on the vehicle's nominal working pressure (NWP: vessel gauge pressure at uniform gas temperature of 15°C and 100 % SoC) and the fuel temperature delivered by the station.

H70-T40 stands for a 70 MPa and -40°C configuration, which is used in this report due to its fastest fueling time. Ratio of vehicle hydrogen storage density to NWP density is called State-of-Charge, and density at 100% SoC and H70 corresponds to 40.2 kg/m3̂:

$$SoC(\%) = \frac{\rho(P,T)}{\rho(NWP, 15°C)} * 100\% \tag{B.2}$$

C Models

C.1 Demand

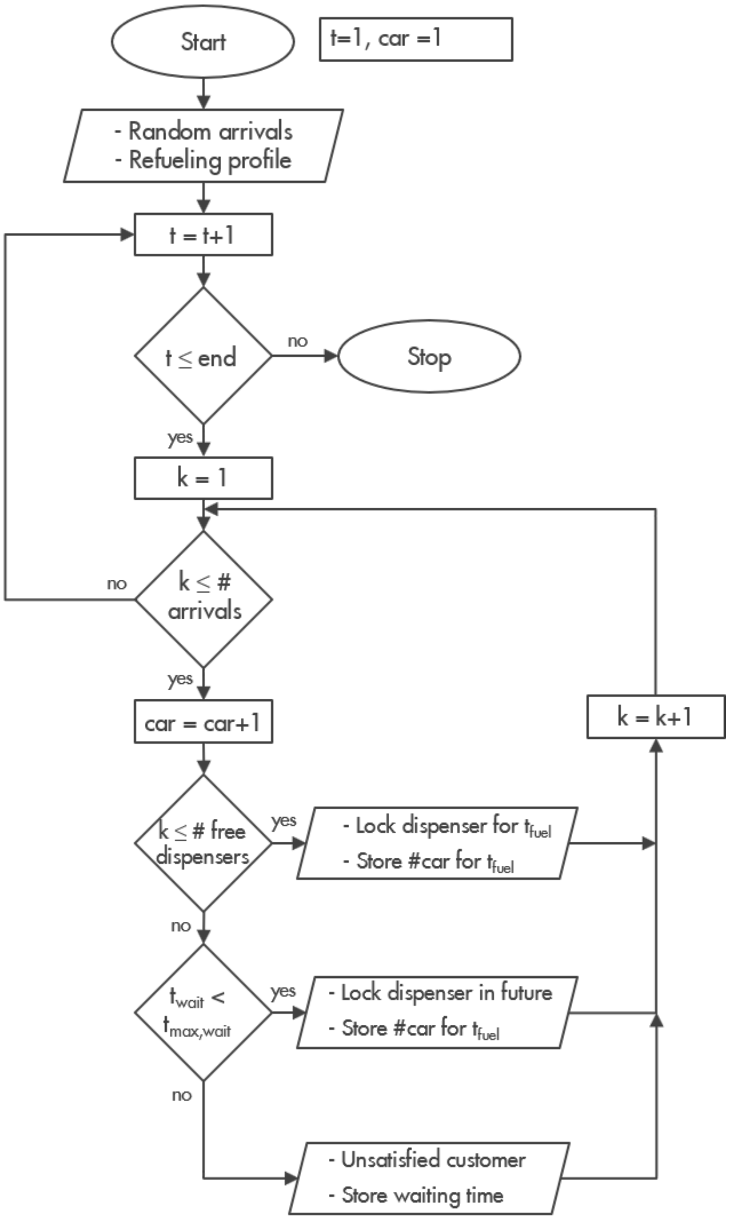

Figure C.3: Flowchart car arrival and cueing

C.2 Electric system

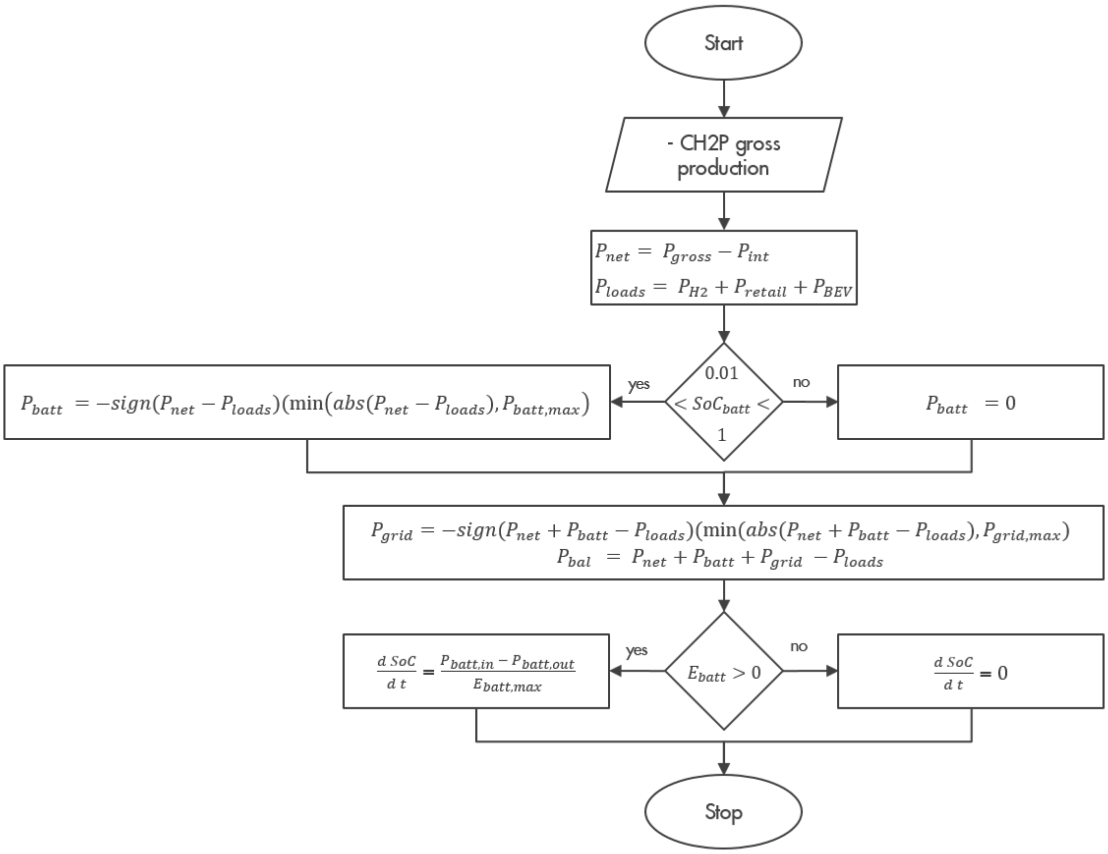

Figure C.4: Flow chart for power calculation

D Results

D.1 Optimization

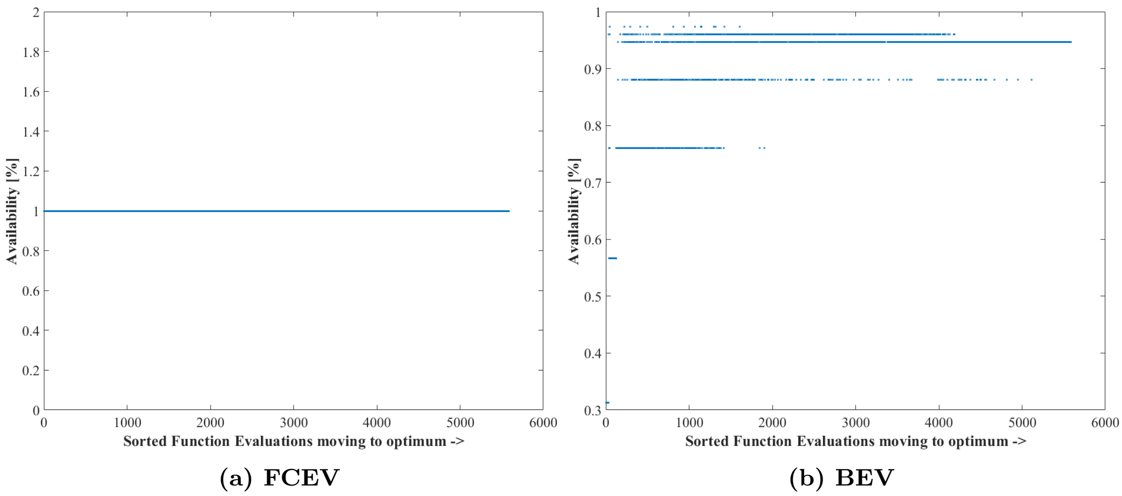

Figure D.5: Optimization results: availability refuelling spots

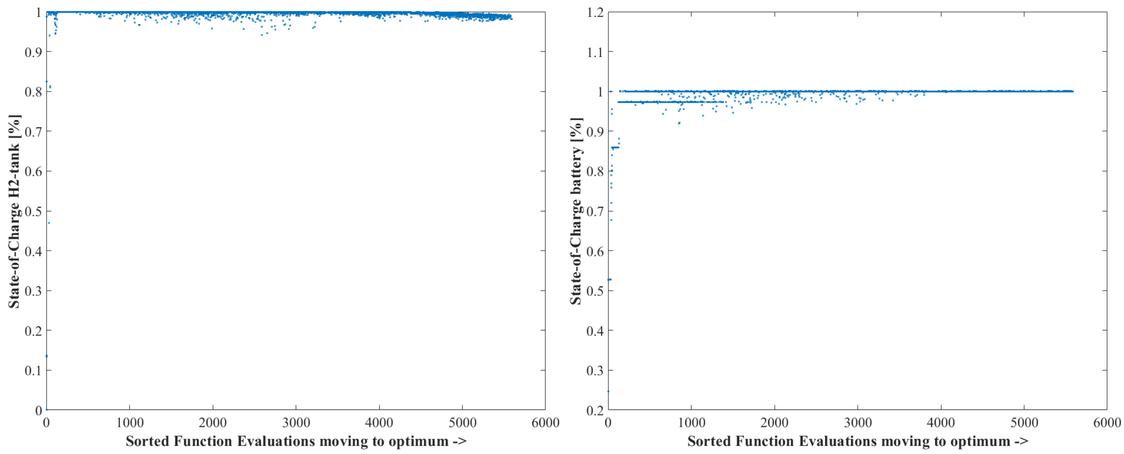

(a) FCEV **(b) BEV**

Figure D.6: Optimization results: average State-of-Charge of all vehicles at end of day

Some graphs have been omitted from this version of the report.

Bibliographic Information

Classification	Unrestricted
Report number	SR.19.001
Title	Modelling and Optimization of a Hydrogen Refuelling Station based on CH2P Technology
Sub title	Delivering decentralized hydrogen and electricity for mobility
Author(s)	Daniel Heere
Keywords	Hydrogen, Solid Oxide Fuel Cell, EV, CH2P, HRS, infrastructure
Date of Issue	April 31st, 2019